

Investigations of low-dimensional emitter system by dynamic strain platform

**Von der Fakultät für Mathematik und Physik
der Gottfried Wilhelm Leibniz Universität Hannover**

zur Erlangung des akademischen Grades

Doktor der Naturwissenschaften

Dr. rer. nat.

genehmigte Dissertation von

M. Sc. Zhao An

2023

Referent: Prof. Dr. Fei Ding
Korreferent: Prof. Dr. Jonathan J. Finley

Tag der Promotion 02.05.2023

Abstract

Two-dimensional transitional metal dichalcogenides (2D TMDs) and zero-dimensional quantum dots (QDs) are among the most representative low-dimensional emitter systems, with one or three dimensions on nano-scale. Both of them exhibit potential for (quantum) optical applications. Analog to the electric field and magnetic field, strain is a powerful probe to detect the physics of the emitter systems. The reduced dimension renders strain tuning more applicable to deepen the understanding and tune their properties. Previous researches demonstrate that strain can change the distance of particles or/and the symmetry. Based on this, we conduct some investigations: *first*, we detect the responses of monolayer WSe₂ to biaxial in-plane strain. Generally, all the helicities of excitons and trions are related to the scattering process. In our observation, the decreases of exciton circular helicities in WSe₂ and MoSe₂ are associated with their e-h exchange interactions. The helicity of trion in MoSe₂ is almost intact, and a phenomenological rate equation model is developed to describe the decrease of trions in WSe₂, which agrees with our observation well. Our findings provide a new strategy to tune the read-in/read-out in TMDs-based memory devices. *Second*, we focus on the responses of WSe₂ to uniaxial strain. We identify fine structures of neutral exciton in polarization-dependent photoluminescence spectroscopy. The nonlinear evolutions, in terms of amplitude and phase, with an active uniaxial strain are interpreted by the interaction of wavefunction with strain. Though these two bulk strain-tuning platforms hold the potential for sophisticated emitter systems, a more versatile strain-tuning platform is needed. *In the last section of this work*, a 2-leg MEMS strain-tuning platform is fabricated and then integrated with a QDs-embedded membrane. We resolve the position-dependent anisotropic strain on the strain-tuning platform and compare the opposite responses of positive and negative trions to the same strain. Our observation agrees well with the previous pseudo-potential/configuration interaction calculations. Notably, the 2-leg strain platform applies to 2D TMDs.

These findings act as some helpful attempts to deepen the understanding of low-dimensional emitter systems. In some ongoing work, we get a prototype as a more versatile strain-tuning platform. We envision this platform can add a degree of freedom for the integrated photonic circuits.

Keywords:

Cryogenic strain-tuning, 2D TMDs, quantum dots, optical properties, degree of polarization, symmetry evolution, opposite responses of trions

List of abbreviations

| | |
|----------------|--|
| 2D | two dimensional |
| AFM | atomic force microscope |
| MBE | molecular beam epitaxy |
| FSS | fine structure splitting |
| LCVR | liquid crystal variable retarder |
| PL | photoluminescence |
| QDs | quantum dots |
| TMDs | transitional metal dichalcogenides |
| X | neutral exciton |
| T _t | triplet negatively charged trion |
| T _s | singlet negatively charged trion |
| XX | neutral bi-exciton |
| D ⁰ | spin dark exciton |
| ZPL | zero phonon line |
| SOC | spin-orbit coupling |
| HOM | Hong-Ou-Mandel |
| VBM | valance band maximum |
| CBM | conduction band minimum |
| Dop | degree of polarization |
| SHG | second harmonic generation |
| PMN-PT | [Pb(Mg _{1/3} Nb _{2/3})O ₃] _{0.72} -[PbTiO ₃] _{0.28} |

Contents

| | |
|---|----|
| Abstract..... | 1 |
| Keywords: | 2 |
| List of abbreviations | 3 |
| 1. Introduction | 9 |
| 1.1 Structure and Properties of 2D Transition Metal Dichalcogenides..... | 9 |
| 1.1.1 Composition and Chemical Bonds..... | 9 |
| 1.1.2 Structural Symmetry | 11 |
| 1.1.3 Band Structure | 13 |
| 1.1.4 Valley contrasting physics and optical selection rules | 15 |
| 1.2 Description and Effect of Strain in 2D Transition Metal Dichalcogenides | 16 |
| 1.2.1 Description of Strain in 2D Materials..... | 17 |
| 1.2.2 Types of strain..... | 18 |
| 1.2.3 Effect of Strain on TMDs | 19 |
| 1.3 Strain tuning techniques | 22 |
| 1.3.1 Atomic force microscopy tips..... | 23 |
| 1.3.2 Substrate deformation | 24 |
| 1.3.3 Substrate patterning | 26 |
| 1.3.4 Diamond Anvil Cell..... | 27 |
| 1.3.5 Piezoelectric Actuators | 28 |
| 1.4 Introduction of quantum dots | 31 |
| 1.5 QDs Physics | 32 |
| 1.6 Optical Parameters of QDs..... | 35 |
| 1.6.1 Lifetime and Coherence Time | 35 |
| 1.6.2 Fine Structure Splitting | 35 |
| 1.6.3 Second-order Time Correlation Function | 35 |
| 1.7 Influence of Strain on QDs..... | 37 |
| 1.8 Summary of details..... | 39 |
| 1.8.1 Research topic | 39 |
| 1.8.2 Motivation..... | 39 |
| 1.8.3 Structure of this thesis..... | 40 |
| 2. Technology | 45 |
| 2.1 Light Path..... | 45 |
| 2.1.1 Power Modulation..... | 45 |

| | | |
|-------|--|-----|
| 2.1.2 | Polarization and Etaloning Effect | 46 |
| 2.2 | Fabrication of Emitters..... | 47 |
| 2.2.1 | Fabrication of 2D TMD | 47 |
| 2.2.2 | Fabrication of QDs Embedded Nanomembrane | 47 |
| 2.3 | Fabrication of Piezoelectric Actuator..... | 48 |
| 2.3.1 | Bulk Biaxial Piezoelectric Single Crystal..... | 48 |
| 2.3.2 | Bulk Uniaxial Piezoelectric Single Crystal..... | 49 |
| 2.3.3 | Laser Cut Piezoelectric Single Crystal | 49 |
| 2.4 | Electric Tuning Strategy..... | 49 |
| 2.4.1 | Lateral Electrodes for QDs Nanomembranes | 50 |
| 2.4.2 | Lateral Electrode for 2D TMDs..... | 50 |
| 3. | Strain control of exciton and trion valley depolarization in monolayer transition metal dichalcogenides..... | 53 |
| 3.1 | Introduction | 53 |
| 3.2 | Sample fabrication..... | 54 |
| 3.3 | Results and discussions | 55 |
| 3.4 | Conclusion..... | 62 |
| 4. | Manipulation of WSe ₂ exciton fine structure by anisotropic strain..... | 65 |
| 4.1 | Introduction | 65 |
| 4.2 | Sample and Experimental Setup | 66 |
| 4.3 | Results and discussions | 67 |
| 4.4 | Conclusions and prospectives | 75 |
| 5. | Strain-induced modulation of quantum dot emissions at Si-vacancy transitions..... | 77 |
| 5.1 | Introduction | 77 |
| 5.2 | Sample fabrication..... | 79 |
| 5.3 | Results and discussions | 79 |
| 5.4 | Conclusion and prospective | 85 |
| 6. | Appendix | 89 |
| 7. | Conclusion and outlook..... | 93 |
| | Conclusion..... | 93 |
| | Outlook..... | 93 |
| | Bibliography | 95 |
| | Acknowledgments..... | 113 |
| | Publications and Presentations..... | 117 |
| | Publications and manuscripts:..... | 117 |

| | |
|------------------------------------|-----|
| Scientific Talks and Posters | 117 |
| Selbständigkeitserklärung | 119 |
| Curriculum Vitae | 121 |

1. Introduction

In this section, the general knowledge of 2D Transition Metal Dichalcogenides and quantum dots are reviewed, respectively. In each section, their interactions with strain are particularly discussed.

Based on the state-of-the-art, a summary of details is followed, stating the choice of research topic, motivation of the research, the findings, and the status of the work. The contributions are stated.

1.1 Structure and Properties of 2D Transition Metal Dichalcogenides

1.1.1 Composition and Chemical Bonds

TMDs are layered structures of the type MX_2 , where M is the transition metal atom (e.g. Mo, W, Ti, Zr, Re, Pt, Nb, and Ta) and X the chalcogen atom (e.g. S, Se, and Te). Different chemical compositions result in unique properties of 2D TMDs: for instance, NbSe_2 exhibits superconductivity, while MoS_2 is a semiconductor, and TiS_2 shows metallic properties.

TMDs monolayers comprise a X–M–X trilayer where the M atom layer is sandwiched by two X atom layers. Each M atom is six-coordinated, and the atomic interaction is governed by the chemical bonds between M and X, as shown in Figure 1. 1 Interlayer interaction between different TMDs monolayers is determined by Van der Waals forces, far weaker than the chemical bonds within each layer. The characteristics of each material are influenced by the thickness, geometry, and electronic configuration [1]. The interplay of different binding mechanisms allows for a certain freedom in designing new materials systems by vertically stacking different types of TMDs monolayers. In the following, we focus more on the most frequently studied TMDs: MoS_2 , MoSe_2 , WS_2 , and WSe_2 .

In silicon or graphene, the electronic properties are determined by the hybridization of s and p orbitals. In contrast, the d orbital filling of the transition metals has a major effect on the properties of 2D TMDs. The transition metal atoms contain partly filled d orbitals in the configuration $5s^14d^5$ (Mo) and $6s^24f^{14}5d^4$ (W). In the chalcogen atoms, the orbitals are filled regularly, with $3s^23p^4$ (S) and $4s^24p^4$ (Se). The difference in electronegativities between M (above 1.36) and X atoms (2.58 for S, 2.55 for Se, and 2.12 for Te) is not large enough (typically <1.7) for developing fully ionic bonds. In the resulting mixture of covalent and ionic bonds, the electron density shifts from the d orbital of the M atoms closer to the X atoms. The degree of d orbital filling influences the atomic structure of TMDs layers, resulting in two types of phases: trigonal prismatic (H – hexagonal symmetry) or octahedral

(T – tetragonal symmetry). In the trigonal prismatic phase the X atoms are vertically aligned with each other, while in the octahedral phase, the top X atom layer is rotated $\pi/3$ around the vertical axis passing through the M atom (see Figure 1. 1). In the 1H phase (a single TMDs layer) the d orbitals tend to split into three degenerate sub-states, d_{zx}, d_{yz} and $d_{x^2-y^2}, d_{xy}$ and d_{z^2} with ≈ 1 eV splitting between the latter two states. In the 1T phase, the d orbitals split into two orbitals $d_{x^2-y^2}, d_{z^2}$ and d_{zx}, d_{yz}, d_{xy} . [2]

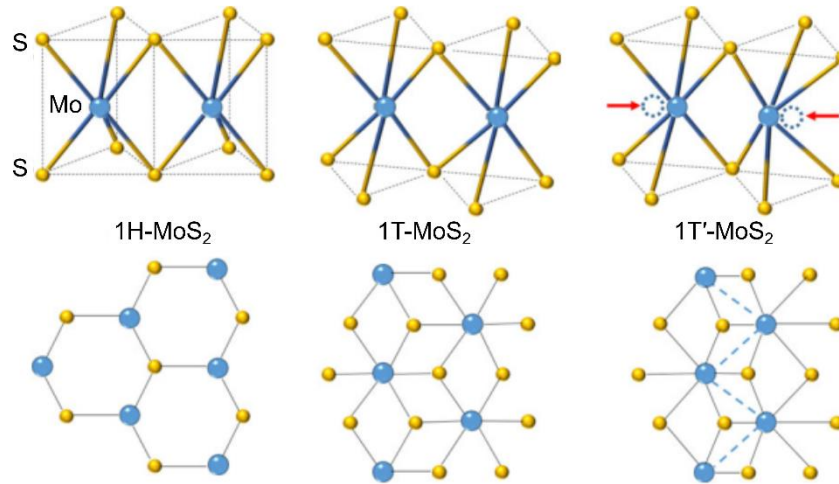


Figure 1. 1. Different phase structures of monolayer MoS₂. The top shows the side-view, and the bottom row is the front view. Adapted from Ref. [6]. <https://www.nature.com/articles/s41467-017-00640-2>. Licensed under CC BY 4.0.

T-type monolayers of the group 6 TMDs considered here are metastable and can relax into other phases [2] such as the zigzag phase (T' - blue, dashed line in Figure 1. 1T (or T') type monolayers are metallic, while the H phase shows semiconducting properties. The electronic properties are a result of the d orbitals filling since the p-orbitals of the X atoms are energetically much lower than the Fermi energy. For example, in 1H-WSe₂, there are no electrons left in the d orbital resulting in semiconducting behavior. In comparison, in e.g. 1T-VSe₂ (a group 5 TMDs) metallic behavior is observed due to partial filling of the d orbitals. Different phases of TMDs can interconvert e.g. via strain engineering; the principle is shown in Ref. [3]. The interatomic in-plane distances in the T' phase are larger than that in the H phase, which can be one reason for a semiconductor-to-metal transition in response to tensile strain. The lattice mismatch between the H and T' phases determines the strain required to induce the phase transition[4]. Compared to other 2D TMDs, the phase transition

for MoTe₂ occurs particularly fast, as the lattice mismatch is merely 3% (see AFM [atomic force microscope] tuning technique).

Multilayer stacks of the trigonal phase result in hexagonal and rhombohedral symmetry denoted with 2H and 3R, respectively. The monolayer trigonal phase is also called 1H, as in the left sketch of Figure 1. 1. The symmetry and interlayer hopping for 2H and 3R are different. Natural crystals are mostly H-type and are most frequently studied. Below, all the TMDs mentioned are H-type, unless specified.

1.1.2 Structural Symmetry

The symmetry of the crystal lattice is one of the fundamental features determining the properties of solids. Here, the symmetry of 2D TMDs and their effect are discussed. We start by looking at the X and M atom layers. In each layer, X and M are placed in a honeycomb-type structure, similar to the arrangement of carbon atoms in graphene. However, only half of the sites in the TMDs honeycomb structure are occupied, resulting in a C_3 or $2\pi/3$ rotational symmetry. This symmetry is inherited by the X–M–X trilayer. Another symmetry in the (H-type) trilayer is the mirror symmetry, that is, the top and bottom X layers are mirrored with respect to the central M atom layer. Mirror symmetry has great importance: On the one hand, it requires the lifting of the band degeneracy induced by the SOC to be in the out-of-plane (z) direction [5]; on the other hand, the mirror symmetry forces the Bloch functions in the top and bottom layer to be invariant. Lastly, the time-reversal symmetry of K and K' valleys (Figure 1. 3 and Figure 1. 4) in reciprocal space is broadly discussed in the literature and is reviewed in 1.1.4.

If only a kind of monolayer TMDs (i.e. one X–M–X trilayer) is used to construct, stacking them in a similar fashion as lego bricks. 2H type (D_{4h}^6), 3R type (C_{3v}^5), and further multiple (homo)layer TMDs can be obtained. Any symmetries in these assembled systems are determined by the basic symmetry in the monolayer TMDs. One feature shared is that their mirror symmetry is broken.

3R TMDs comprise three X–M–X layers on top of each other. The position of the three layers can be defined by the in-plane translation of each monolayer, where each layer X atom is laterally placed on top of the M atoms in the lower layer (see Figure 1. 2). The interlayer hopping of charge carriers, including the contribution of the valence band and conduction band, vanishes at the K and K' points in reciprocal space, which is determined

by the rotational symmetry of the band edge Bloch function. 3R TMDs share a lot of the properties with monolayer TMDs.

2H TMDs are composed of two X–M–X layers, with the upper monolayer comprising a rotation of π compared to the bottom monolayer. In contrast to 3R, 2H TMDs are inversion symmetric. Different from monolayer and 3R, the interlayer hopping of charge carriers does not vanish at the K and K' points in 2H TMDs are also influenced by the interlayer hopping or hopping vectors because the contribution from the valence band still exists. [5]

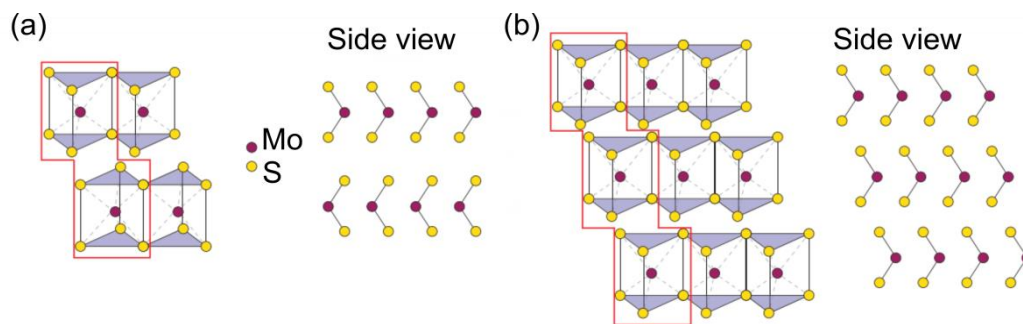


Figure 1. 2. Crystal structure of 2H (a) and 3R (b) MoS₂. Adapted from Ref. [11].

<https://www.nature.com/articles/lisa2016131>. Licensed under CC BY-NC-SA 4.0.

An even number of layers in a TMDs result in inversion symmetry, in contrast to the case of an odd number. This symmetry gives rise to many different phenomena: 2D materials with an odd number of layers are piezoelectric while with an even number of layers, they are not. Piezoelectricity requires the crystal to not be inversion symmetric, so the positive and negative centers of charge will not coincide when subjected to external strain. Additionally, the breaking of the inversion symmetry allows for studying valleytronics [6].

Materials containing different types of monolayers are called heterostructures or heterojunction samples. We limit our discussion to the simplest case of two different monolayers (called heterobilayers). Due to the comparatively weak out-of-plane Van der Waals interaction, lattice mismatch and a twist angle between the monolayers can exist. While basic monolayer symmetries can be inherited, these additional degrees of freedom enable the formation of new higher-order periodical structures, so-called Moiré patterns. The structure of this superlattice or supercell will introduce an additional symmetry.

In heterobilayers, the superlattice constant is $b \approx a/\sqrt{\delta^2 + \theta^2}$, where a is the lattice constant of the monolayer TMD, θ is the twist angle, and δ is the lattice mismatch. The larger the twist angle and lattice mismatch, the smaller the superlattice cell will be. The

experimentally observed lattice constants of Moiré patterns are usually in the order of several tens of nm, but can also be as low as 0.5 nm [7].

Heterobilayers have two types of stacking formations as determined by a twist angle of 0 or π , corresponding to H- and R-type stacking (names come from the 2H and 3R stacking in TMDs monolayer). Additionally, different twist angles and lattice mismatches result in distinguished local atomic arrangements or registries. There are 6 high symmetric points in Moiré patterns (3 in H-type stacking, 3 in R-type stacking). In these high symmetric points, C_3 symmetry is still intact. However, the optical selection rules are different [8] because of the broken mirror symmetry in the heterobilayer. Besides, the interlayer hopping of charge carriers brings an extra deviation into the local potential distribution.

After discussing the structural properties in real space, we now move on to the reciprocal space.

1.1.3 Band Structure

In the following, we focus our discussion on the four most commonly studied (VIB group) TMDs: MoS₂, MoSe₂, WS₂, and WSe₂. Monolayer TMDs can be exfoliated from their bulk counterparts. In bulk TMDs, the conduction and valence band edges are in the Q(Λ) point and Γ point, respectively, therefore forming an indirect band-gap. For decreasing thickness of the TMDs, the valence band energy increases and the conduction band energy decreases, resulting in a widened band-gap. Furthermore, due to band-edge shifting, the indirect band gap turns into a direct one. The band character at different points in the reciprocal lattice can be assigned to the different contributions of the involved atomic orbitals: At the K and K' points the d orbitals from the M atoms contribute most, and their localized nature results in stable bands at the K and K' points when the TMDs thickness decreases. As a consequence, the band edges transfer to the K and K' points. The photon emission and light-matter interaction [9] in the monolayer are much stronger than that in the bilayer counterpart.

Multilayer systems exhibit slightly different properties compared to monolayer TMDs due to the additional interlayer interaction. The different orbitals of M and X atoms exhibit distinct contributions to the band edges, causing the band edges to be site-dependent. In multilayer structures, this results in different magnitudes of interlayer hopping at the K and Q(Λ) points (Figure 1. 3). The work function and bandgap in the four TMDs considered here have values such that any combination of these TMDs in a heterobilayer will exhibit staggered band [10–15] alignment (type-II band edges) as sketched in Figure 1. 3 (c). As a

result, the photoexcited electrons and holes will relax to the conduction band edge of MoX_2 and the valence band edge WX_2 . When irradiated by laser light, the generated carriers in one layer can transfer to the other layer before recombination. Driven by the large band offset of the conduction (several tens of meV) and valence bands (several hundred of meV) of the different layers, the charge transfer is ultra-fast (<1 ps) [16]. In comparison, the decay time of intra-layer electrons is typically in the range of 1–100 ps. The electron and hole, distributed in the two respective layers, will still form an exciton because of the strong Coulomb interaction. The spatial separation of the carriers and indirect exciton momentum will lead to long radiative lifetimes that can reach 100 ns [17]. Compared to the in-plane monolayer exciton, the interlayer excitons show new interesting features and potential for valley-functional optoelectronic devices [18].

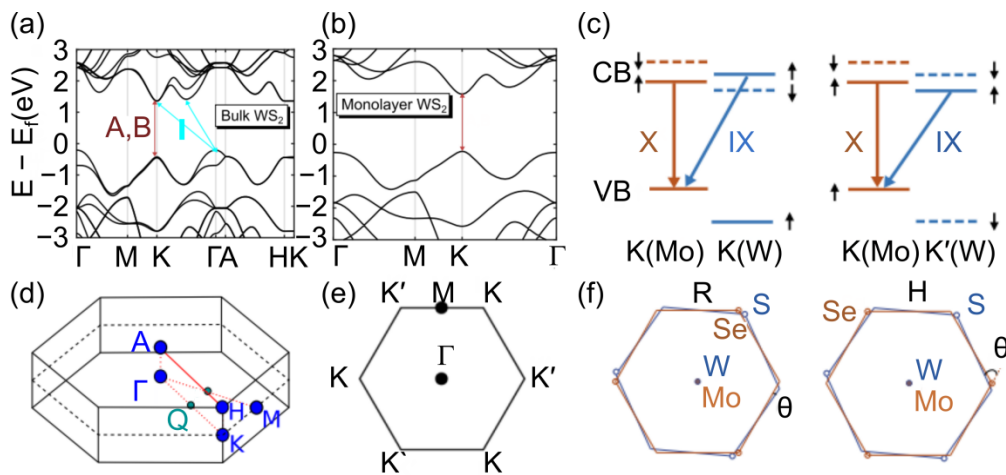


Figure 1. 3. Band structures and Brillouin zones for TMDs. (a,b) Calculated band structure of bulk and monolayer WS_2 , showing indirect and direct band gaps, respectively. (d,e) The corresponding 3-dimensional and 2-dimensional Brillouin zones, highlight different symmetry points. (c) Schematic band structure of a $\text{WS}_2/\text{MoSe}_2$ heterobilayer, showing type II (staggered) band alignment. Black arrows denote the spin orientation of the charges in the conduction (CB) and valence band (VB). The radiative transitions of intra-layer excitons (X) and interlayer excitons (IX) are shown. (f) 2-dimensional Brillouin zones so does of a $\text{WS}_2/\text{MoSe}_2$ heterobilayer with the twist angle (θ). (a), (b), (d) adapted from Ref. [19]. <https://www.nature.com/articles/s41699-020-00162-4>. Licensed under CC BY 4.0. Figure (e) adapted from Ref. [20]. <https://www.nature.com/articles/s41467-019-11697-6>. Licensed under CC BY 4.0. Figures (c) and (f) adapted from Ref. [21].

<https://www.nature.com/articles/s41467-020-19466-6>. Licensed under CC BY 4.0.

A further property that changes when comparing bulk to monolayer TMDs are the band curvatures and therefore effective masses of the carriers, as shown in Figure 1. 3(a,b). The

reason for the change of effective mass at the band edge is twofold: On the one hand, the density of state at the same points (Γ in the valence band [VB] and Λ in the conduction band [CB]) is altered. On the other hand, when changing from bilayer to monolayer TMDs, the band-edge shifts from the Γ point in VB (Λ point in CB) to the K (K') point. A similar band-edge shift can be induced by strain, as illustrated in Section 1.2.3.

1.1.4 Valley contrasting physics and optical selection rules

Monolayer TMDs provide a platform for investigating spintronics and valleytronics, which show strong potential for information storage and processing. Valleys are the extrema of the conduction and valence bands in reciprocal/momentum space. In the K and K' points exist energy degenerate but in-equivalent valleys, see Figure 1. 4. Strong SOC not only leads to lifted degeneracy of the bands at K and K' points but also a coupling between spins and valleys. The spin polarization in the different valence bands has to be the opposite in the K and K' points to preserve time-reversal symmetry [22]. The mirror symmetry requires the spin quantum number to be the same in the conduction band and valence band. The selection rules are additionally governed by the C_3 symmetry. As a result, the spin-conserved transition between valence and conduction band at the K valleys will couple with σ^+ , while K' valleys couple with σ^- as e.g. experimentally observed by Xu and coworkers. [23]. Photons polarized perpendicular to the atomic plane are forbidden (dark excitons) at normal incidence as in standard spectroscopy [8]. However, they can be detected, but with significantly weaker intensity (several percent) compared to the in-plane polarized signal [24].

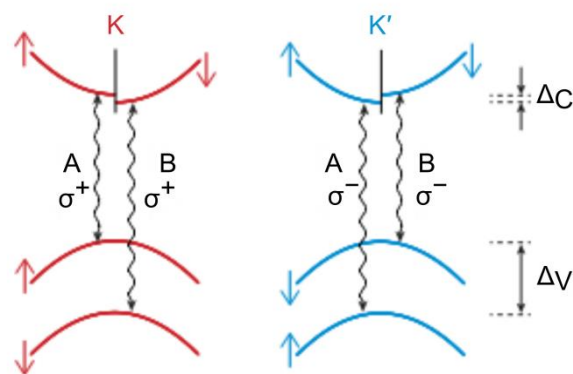


Figure 1. 4. Valleys and optical selection rules in monolayer TMDs. The red and blue arrows denote the spin directions, and Δ_c and Δ_v the splitting in the conduction and valence bands, respectively.

Adapted from Ref. [25]. <https://www.nature.com/articles/ncomms10643>. Licensed under CC BY 4.0.

Besides the optical selection rules in the monolayer, the valley Hall effect (a type of anomalous Hall effect) also attracts much attention. It is based on the coupling between the orbital motion of electrons with the valley degree of freedom and results in electrons from different valleys moving in opposite directions, perpendicular to the drift current [37, 38]. This is often explained using pseudo-vectors such as the Berry curvature and orbital magnetic moment, which show even parity in the K and K' valleys in the presence of inversion symmetry. In this case, these quantities at K and K' valleys take the same value under a uniform electric field. The breaking of the inversion symmetry is therefore necessary to obtain a valley contrast. In the monolayer case, the inversion symmetry is broken, and therefore the berry curvatures at K and K' points give rise to opposite velocities perpendicular to the applied electric field.

The physics in heterobilayers is more complex due to position-dependent atomic registries. The absence of mirror symmetry allows spin-flips in the heterobilayer. Because of the twist angle and lattice mismatch, the overall degree of symmetry is not as high as in the monolayer [8]. The optical properties have been recently observed experimentally by Xu and coworkers [11] and other researchers [39, 40], looking at the distribution of optical polarization in the Moiré pattern.

1.2 Description and Effect of Strain in 2D Transition Metal Dichalcogenides

Deeper insight into the underlying physics of a material can be obtained using external fields or structural variations, often leading to novel applications. Applying electric [30] and magnetic fields [31] or doping [32] is a frequently used tuning technique. In 2D materials, strain engineering is found to be particularly suitable. The enhanced strength and flexibility allow for tuning the strain in a wide parameter space. In 2D materials, the concentration of defects is typically low, the concentration is about 1% [33,34] in 2D MoS₂. According to Griffith's theory [35], the mechanical strength of a material approximates the theoretical value that is determined by the strength of the chemical bonds. As a result, the mechanical strength will be enhanced greatly. On the other hand, in the continuum theory, the reduced dimension gives rise to higher flexibility. Additionally, strain can be actively varied in its configuration (uniaxial, biaxial, and tensile, discussed in Section 1.2.2 and magnitude by

various methods (discussed in Section 1.3), allowing control over structural, electronic, and optical properties.

The research on 2D TMDs materials has been greatly influenced by the research on graphene. Strain engineering techniques are no exception; e.g. Ding and coworkers [36] reported the reversible tuning of graphene by using piezoelectric actuators. Until now, there are various reports on the strain tuning of 2D TMDs, covering experimental aspects as well as *ab initio* calculations. In the following, some representative reports are reviewed, starting from simple isotropic strain to the more general anisotropic case.

1.2.1 Description of Strain in 2D Materials

Elastic bodies can move and deform when subjected to an external load. The relative amount of elastic deformation can be described by the dimensionless quantity strain. In a one-dimensional crystal lattice, the strain can be described as the relative change of the lattice:

$$\epsilon = \frac{a' - a}{a} \quad (1.1)$$

where ϵ is the strain, a' is the lattice constant after, and a before deformation. In a three-dimensional system, the strain tensor is composed of the strain coefficients ϵ_{ij} :

$$\boldsymbol{\epsilon} = \begin{pmatrix} \epsilon_{xx} & \epsilon_{xy} & \epsilon_{xz} \\ \epsilon_{yx} & \epsilon_{yy} & \epsilon_{yz} \\ \epsilon_{zx} & \epsilon_{zy} & \epsilon_{zz} \end{pmatrix} \quad (1.2)$$

Considering the linear-elastic regime and excluding rigid body rotations, $\boldsymbol{\epsilon}$ is symmetric ($\epsilon_{ij} = \epsilon_{ji}$) and can be described by only six components. The tensor has eigenvalues ($\epsilon_1, \epsilon_2, \epsilon_3$) which are called the principal strains.

For two-dimensional material systems, a strong focus lies on the in-plane strain [37,38]. The in-plane strain tensor can be written as

$$\boldsymbol{\epsilon} = \begin{pmatrix} \epsilon_{xx} & \epsilon_{xy} \\ \epsilon_{xy} & \epsilon_{yy} \end{pmatrix} \quad (1.3)$$

Now considering a symmetric tensor again, a rotation of the coordinate system leads to [38]:

$$\boldsymbol{\epsilon} = \begin{pmatrix} \epsilon'_{xx} & 0 \\ 0 & \epsilon'_{yy} \end{pmatrix} \quad (1.4)$$

With the principal strain components ε'_{xx} , ε'_{yy} . If the off-diagonal (shear strain) components are not equal, there will be rotation. The strain tensor can then be determined by

$$\epsilon \cong \begin{pmatrix} \varepsilon''_{xx} & \varepsilon''_{xy} - \theta \\ \varepsilon''_{xy} + \theta & \varepsilon''_{yy} \end{pmatrix} = \mathcal{S}(\epsilon) + \mathcal{T}(\theta) \quad (1.5)$$

where $\mathcal{S}(\epsilon)$ denotes the strain contribution and $\mathcal{T}(\theta)$ the contribution by rotation [37].

1.2.2 Types of strain

Strain can be categorized into various types. Due to the reduced dimension of TMDs, it is natural to first classify between *in-plane and out-of-plane strain*. If the strain is solely directed along the plane of the 2D TMDs, it is called in-plane strain; otherwise, it comprises additional out-of-plane components. Experiments of 2D TMDs mostly report on the in-plane strain, which has been achieved by different techniques such as substrate-bending, substrate thermal expansion, or piezoelectric actuators. Additional out-of-plane strain components can be introduced by applying hydrostatic pressure on the 2D TMDs, such as in a Diamond Avil Cell.

By applying in-plane strain, TMDs can be stretched or compressed, corresponding to *tensile and compressive strain*, respectively. There are only a few techniques that allow for applying compressive strain. If a compressive strain is applied by techniques based on a deformation of the substrate, the TMDs layers are likely to detach or form wrinkles. Tensile strain is more frequently reported.

Another possible classification is deduced from the uniformity of the strain throughout the TMDs layers; *homogeneous and inhomogeneous (local) strain*. A uniform strain distribution leads to a homogeneous change of material properties. Localized strain gives rise to inhomogeneous strain fields, leading to modified bandgaps in different positions of the 2D TMD, as shown in Figure 1. 5 The resulting local potential minima are energetically favorable for the excitons compared to the surrounding area. Excitons, therefore, drift to the strain center, where they can decay under the emission of a photon. This is also referred to as the funnel effect due to the structure of the electronic potential and is attractive for PL and electroluminescence applications.

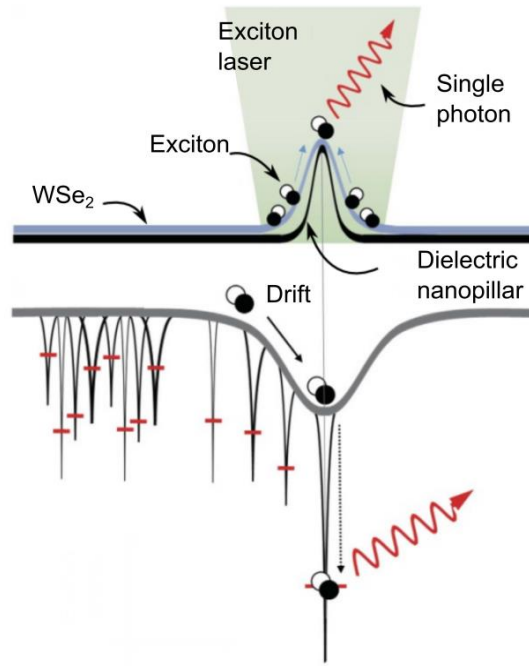


Figure 1. 5. Atomically thin WSe₂ is deformed by localized strain which inhomogeneously modulates the bandgap. Adapted from Ref. [39]. <https://www.nature.com/articles/ncomms15053>. Licensed under CC BY 4.0.

1.2.3 Effect of Strain on TMDs

Strain can exert its influence in two fundamental aspects, the distance of atoms and symmetry. Changing the spatial extent and angles of the inter-atomic bonds leads to changes in the band structure (effective masses, direct to indirect band gap transitions, etc.) and vibrational modes. Furthermore, the symmetry can be changed, e.g. by breaking the C_3 symmetry when applying uniaxial strain [47, 82]. Considering Moiré patterns in twisted bilayers, the application of strain has an additional effect, since the material properties are now atom registry-dependent. Strain can change atom coordination/registry and lattice mismatch.

Changes in the properties of 2D TMDs by applying strain were reported by experiments and *ab initio* calculations. These changes can be observed using various strain-tuning techniques that allow for the application of different types of strain. While the details about these techniques are discussed in Section 1.3, below the dependence of the 2D TMDs properties on the different types of strain is discussed.

What all the *ab initio* calculations suggest [32, 82] is that (small) tensile strain leads to a shrinkage of the bandgap while compressive strain gives rise to increased separation of the

conduction band and valence band, which has been confirmed in various experiments, see 1.3. However, it has been reported that beyond a critical limit, compressive strain results in a shrinking bandgap, see Figure 1. 6(f). The change of the bandgap is slightly different in each type of 2D TMDs monolayer, a qualitative explanation is given in Ref. [44].

Strain can modify the band structure. Once the compressive strain is beyond a critical point, band edges of monolayer TMDs change to K and Λ points [45], by which the direct band gap transforms into an indirect one as shown in Figure 1. 6(d–f) Sufficient in-plane tensile strain can “pull” the VBM from the K point to the Γ point. Tensile strain can also induce phase transitions. Calculations [88, 90] revealed that the band structure of MoS₂ will undergo a semiconductor-metal transition when the in-plane isotropic tensile strain is 11%. Experimentally, the semiconductor-metal transition was achieved by AFM tips and diamond anvil cell (DAC).

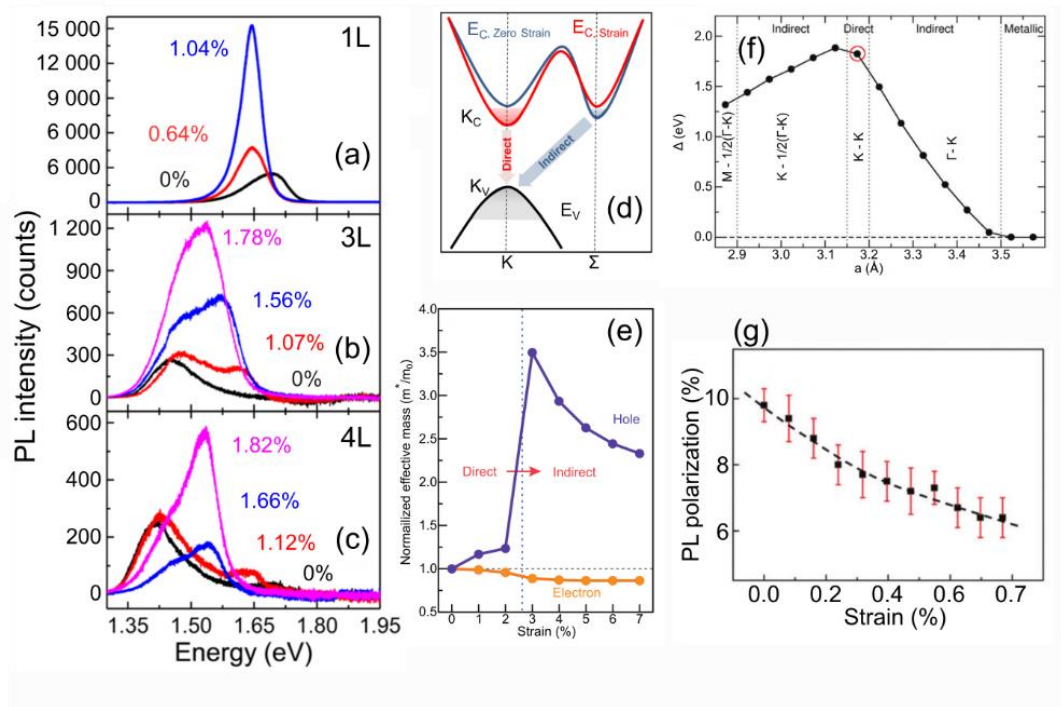


Figure 1. 6 Bandgap and PL in response to external strain. (a-c) PL intensity change of WSe₂ (1 layer, 3 layers, and 4 layers) with tensile strain. (d) Changes in the band structure with in-plane strain. (a-d) adapted from Ref. [47]. Copyright (2014) American Chemical Society. (e) Effective mass change with tensile strain. Adapted from Ref. [48]. Copyright (2013) American Physical Society. (f) *Ab initio* calculation result of band structure under compressive and tensile strain, where the red circle denotes the unstrained state. Band edges (VBM-CBM in the figure) and phase transitions are also shown. Adapted from Ref. [45]. Copyright (2013) American Physical Society.

(g) Change in degree of circular polarization by in-plane tensile strain in a monolayer of MoS₂. Adapted from Ref.[49]. Copyright (2013) American Physical Society.

Change of electron or hole effective mass in a monolayer is complex, influenced by positions (electron effective mass in K or Λ point), directions, and strain configurations [50]. Electron effective masses decrease slightly with in-plane tensile strain [48,50–53]. It is worth noting that the hole effective mass shows a discontinuous shift [89, 93] when the band edges in the transition between a direct and indirect bandgap, see Figure 1. 6.

Strain can change the intensity of the PL emission. The responses to strain at different sites in the reciprocal lattice (e.g. K or Γ points) are different, which is why a competition of the band exists, as shown in Figure 1. 6(d). Under tensile strain, the conduction band around the K point is lowered, enhancing the direct band gap contribution. The stronger decay of excitons in a radiative way leads to a higher PL intensity. MoX₂ and WX₂ show opposite changes, as the main contribution is attributed to the valence band and conduction band, respectively. Experimentally, a growing PL intensity of WSe₂ [47] and WS₂ [54] peaks was observed by applying strain, and a decreasing intensity for MoS₂ [54].

The optical polarization of the emission is determined by the valley-dependent optical selection rules, as discussed in Section 1.1.4. The degree of Polarization (Dop) [49] is defined by $Dop = (I_{co} - I_{cr}) / (I_{co} + I_{cr})$, where I_{co} is the intensity of the co-polarized signal and I_{cr} is the intensity of the cross-polarized signal. The Dop is influenced by the quality of the sample, the type of excitons (neutral or charged), and the type and magnitude of strain. Figure 1. 6(g) shows a decrease of the neutral exciton Dop in MoS₂ with tensile strain at room temperature. Recently, in the research area of heterobilayers and Moiré patterns, a circular to linear polarization transition was reported [55] due to the strain that occurs in the fabrication process. Changes in the polarization were also reported in 2D TMDs using magnetic field tuning by the Zeeman effect. [56] Fabian and coworkers [57] pointed out in their calculations that the SOC can be influenced by strain.

The second harmonic generation (SHG) is also influenced by strain. Monolayer TMDs typically show a SHG intensity change dependent on the laser polarization. As shown in Figure 1. 7(b), a pattern of hexagonal symmetry is observed, due to the broken inversion symmetry and non-zero second-order nonlinear susceptibility [38,58,59]. The SHG signal has a good response to external strain with regard to its shape and signal intensity. Studying

the SHG is very helpful in the assembly of heterobilayers since it is twisted angle-dependent.

The change in vibrational properties can be observed using Raman spectroscopy. In-plane tensile strain will induce phonon softening. Furthermore, the in-plane mode E_{2g}^1 will split into two discrete peaks E_{2g}^{1-} (E'^- in Figure 1. 7(c)) and E_{2g}^{1+} (E'^+ in Figure 1. 7(c)). Redshifts of the E_{2g}^1 peak have also been reported. The distance between the in-plane and out-of-plane modes increases with tensile strain. Changes in the out-of-plane mode have been observed in 2D TMDs subjected to strain by piezoelectric actuators or diamond anvil cells.

Besides, tensile strain can increase mobility, because of the reduction of scattering in the valley.

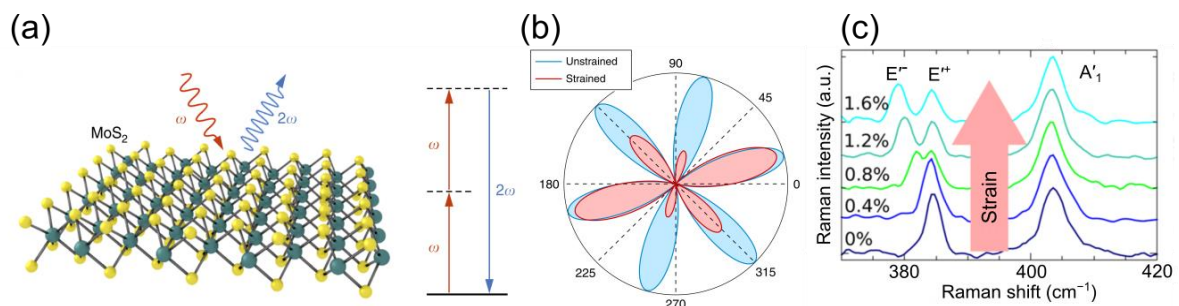


Figure 1. 7. (a) Schematic of SHG in MoS₂. (b) Polarization resolved SHG signal intensity. In the unstrained state, the pattern has a hexagonal symmetry. When strained, the shape and intensity change. Adapted from Ref. [39]. <https://www.nature.com/articles/s41467-018-02830-y>. Licensed under CC BY 4.0. (c) Raman spectra of MoS₂ for different magnitudes of strain. Adapted from Ref. [60]. Copyright (2013) American Chemical Society.

1.3 Strain tuning techniques

Strain can be applied to TMDs with various experimental techniques, which we summarize here. TMDs are usually already subject to strain due to the nature of the fabrication processes like mechanical exfoliation or material growth using molecular beam epitaxy or chemical vapor deposition. In the following, we will discuss the (mostly active) strain tuning techniques, which allow for deterministic control of the TMDs properties. Typically applied techniques will be discussed and classified, starting from atomic force microscope tips and concluding with piezoelectric actuators.

1.3.1 Atomic force microscopy tips

Atomic force microscopes (AFMs) are commonly used in labs across the world and therefore convenient for strain tuning of 2D TMDs, see Figure 1. 8. Dynamic and localized strain fields can be achieved by pressing the tips on the material surface. It is possible to combine this technique with dynamic *in-situ* characterization. Researchers utilized AFM tips to measure the mechanical properties of MoS₂ and obtain a very high Young's modulus [61]. The generated strain fields can be large enough to induce phase transitions: Lee and coworkers [62] investigated the influence of strain on the phase transition by pressing AFM tips with constant load onto MoTe₂. The energetic difference between the 2H and 1T' phase is smaller in this material compared to WSe₂, MoSe₂, WS₂, and MoS₂. The required strain for interconverting the phases is also lower [63]: Sufficient uniaxial tensile strain for the transition is as low as 3%, referring to the lattice constant difference in the two phases (2H 0.61 nm, 1 T' 0.63 nm).

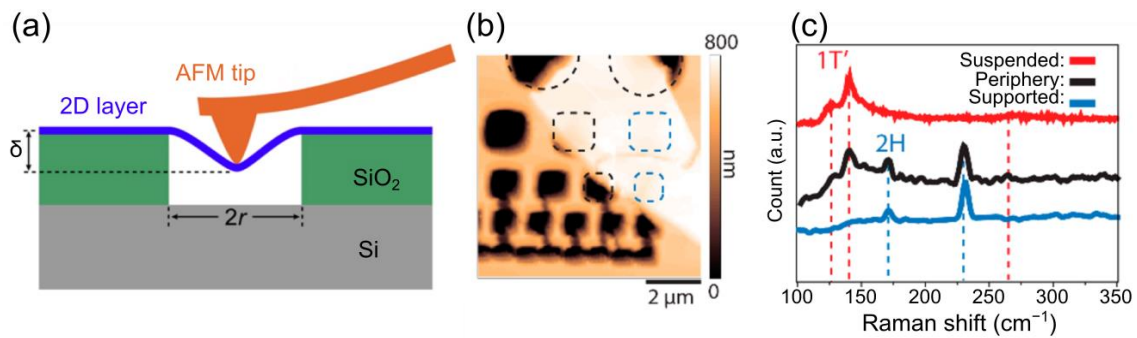


Figure 1. 8. (a) Schematic of strain induced by an AFM tip. Adapted with the permission from Ref.[64]. Copyright (2014) American Chemical Society. (b) AFM topography image of a suspended 2H MoTe₂ flake. The suspended area (partially) covered by the TMDs flake corresponds to the zones enclosed by dashed lines. (c) Raman spectra of MoTe₂ when pressed by an AFM tip. At different positions (suspended, periphery, and supported) the Raman signals are different, revealing a phase transition. Figures (b,c) are adapted with the permission from Ref. [62]. Copyright (2016) American Chemical Society.

When using AFM tips to generate strain fields, the response of 2D materials is substrate and position-dependent. Investigations on graphene showed that the strain on suspended parts of the material can be four to five times larger compared to parts connected to the substrate [65].

The level of strain can be extracted as suggested by Lee and coworkers[62] using $\epsilon=2\delta^2/3r^3$, where δ is the indentation depth, r the radius, and ϵ the radial strain. Wu and coworkers used

$F=(\sigma_0^{2D} \pi)\delta+(E^{2D}q^3/r^2)\delta^3$, where F is the applied load, δ is the indentation depth at the center, σ_0^{2D} is the pretension, r is the radius of the hole, $q=1/(1.05-0.15\nu-0.16\nu^2)$ with ν denoting the Poisson's ratio. One drawback of using AFM tips to generate strain is that it is not very practical in low-temperature measurements or for the development of scalable devices.

1.3.2 Substrate deformation

Strain can be induced by the deformation of the substrate. Bending elastic substrates with 2D materials on top has proven to be an effective way to apply uniaxial or biaxial in-plane tensile strain. The 2D TMDs can be transferred onto substrates such as terephthalate (PET) [49], Polydimethylsiloxane(PDMS) [66], Polycarbonate (PC) [60], polyethylene enaphthalate (PEN) or polyethylene terephthalate glycol-modified (PETG) [67] films. After the transfer, the 2D materials will stick to the top surface of the elastic substrates via Van der Waals interaction. When the flexible substrate is bent, the strain is transferred to the 2D TMDs. According to continuum mechanics, the generated strain follows $\varepsilon=d/2R$, where d is the thickness of the substrate and R is the bending radius, as shown in Figure 1. 9. For cantilever-type bending, the strain level is evaluated by $\varepsilon=(3t\delta/2L^2)(1-x/L)$ [68,69]. Here, L is the length of the substrate, t is the thickness of the substrate, x is the distance from the TMDs flake to the fixed root, and δ is the deflection of the free edge.

Applying tensile in-plane strain with this technique is reported to lead to red-shifts in the PL A peaks and splitting and shift of the E_{2g}^1 Raman peaks [69]. When the bending-induced strain is large enough, slippage of the layers will occur, e.g. for more than 1.3% strain [58] in 2D MoS₂. Depositing titanium on the substrate to hold the TMDs in place can effectively prevent slippage [60] and increases the transferrable strain to more than 2.5% for monolayer MoS₂. Besides, epoxy patches [70], PVA [71], and PDMS encapsulation [72] were used for the same purpose.

A second way to deform the substrate is by stretching it. Elongating a PET substrate with WS₂ led to similar phenomena [73] as discussed for the bending of MoS₂. The application of isotropic strain along the armchair and zigzag direction by aligning the substrate bending axis with the TMDs orientation was also studied both experimentally and using *ab initio* calculations [43]. Biaxial strain can be generated by elongating the substrates in two directions at the same time.

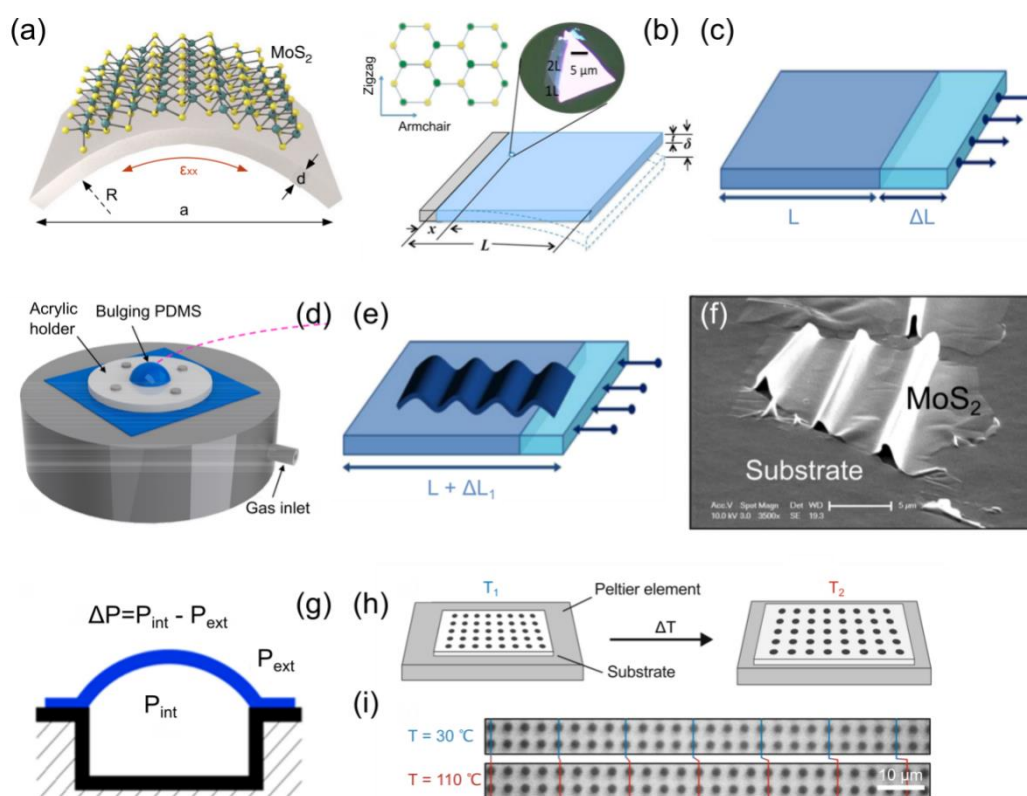


Figure 1. 9. Strain induced by elastic substrate deformation. (a) Schematic of substrate bending for inducing tensile strain. R is the curvature radius, and d is the thickness of the substrate. Adapted from Ref. [38]. <https://www.nature.com/articles/s41467-018-02830-y>. Licensed under CC BY 4.0. (b) Schematic of cantilever bending, where one end (grey) is fixed, and the other is deflected. x denotes the distance of the MoS_2 flake to the fixed end. L is the length of the whole cantilever, and δ the vertical deflection of the free end. Adapted with the permission from Ref. [69]. Copyright (2013) American Chemical Society. (c) Schematic of substrate elongation. L is the length, and ΔL the extension. Adapted with the permission from Ref. [74]. Copyright (2015) American Chemical Society. (d) and (g) show a schematic of a blown bubble. When the inner pressure (p_{int}) is higher than the external pressure (p_{ext}), the elastic substrate will be blown like a bubble. Gas can be led via the inlet (not shown) into the chamber below the PDMS film. Figure (d) is adapted with the permission from Ref. [66]. Copyright (2017) American Chemical Society. Figure (g) is adapted with the permission from Ref. [75]. Copyright (2016) American Chemical Society. (e) Schematic of the prestretch method. L is the length in the idle state, and ΔL_1 is the extension in response to external pressure. Releasing the prestress leads to the formation of wavy wrinkles as seen in the SEM image in (f). Figure (e) adapted from Ref. [74]. Copyright (2015) American Chemical Society. Figure (f) adapted from Ref. [76]. Copyright (2013) American Chemical Society. (h) and (i) show schematics of strain induced by thermal expansion. Adapted from Ref.[77]. <https://www.nature.com/articles/s41699-017-0013-7>. Licensed under CC BY 4.0.

Another possibility is to transfer 2D TMDs on pre-stretched elastic substrates [74,76]. Strain is then induced after releasing the external pre-stress. This technique gives rise to the formation of flat and wrinkled areas and therefore an inhomogeneous strain field distribution. The localized strain can induce the “funnel effect”, i.e. exciton confinement by local strain fields.

2D materials usually have different thermal expansion coefficients compared to the substrate they are placed on [78]. Therefore, strain can be generated simply by heating the materials, e.g. by thermal wires or laser radiation. Homogenous or inhomogeneous strains can be applied by different thermal treatments [78]. Another interesting technique called ‘blown-bubble’ (see Figure 1. 9(g)) was investigated on MoS₂. It was first introduced by Bunch and coworkers [79] in their research on graphene. And extended to MoS₂ by Yang and coworkers [66]. In the original state, the pressure in the cavity (P_{int}) is equal to the pressure outside ($P_{\text{out}}=P_0$, P_0 is the ambient gas pressure). Strain can be induced by a pressure difference, which can be achieved by pumping gas into the cavity under the 2D material.

1.3.3 Substrate patterning

Strain can also be induced in 2D TMDs by patterning the substrate. The artificially increased surface roughness or coarseness leads to local strain fields in the layers transferred on top. The patterning can be performed by Argon bombardment [80], electron beam lithography [39,81], or Al₂O₃ deposition [82]. The roughness of the substrate can be characterized by the AFM and SEM. Then, the 2D TMDs can be transferred to the surface by a stamping process [83]. Local, tensile strain can then be observed at the “spiky” parts of the substrate, as illustrated in Figure 1. 10. The pillars or thorns on the substrate are small in diameter compared to the size of the TMDs flakes. This leads to inhomogeneous strain and therefore the observation of e.g. the funnel effect.

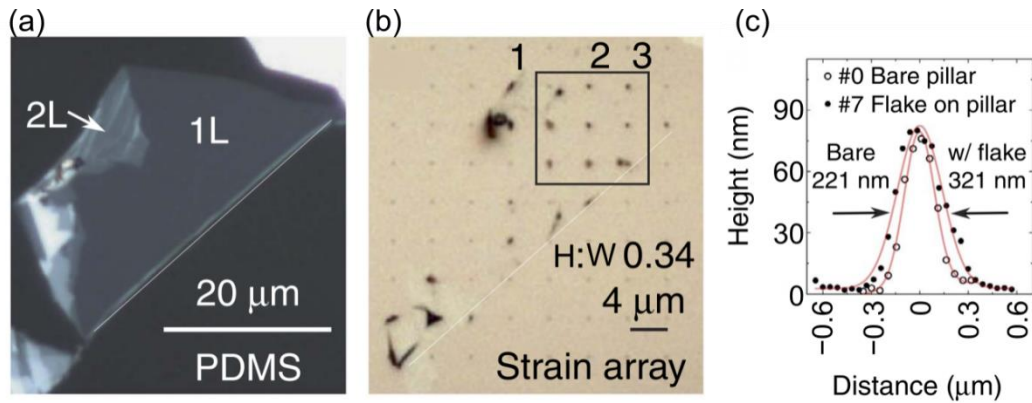


Figure 1. 10. Patterned substrate with monolayer WSe_2 flakes. (a) Optical image after transfer of two layers of WSe_2 onto nanopillars (black dotted array). (b) 2D spatial map of integrated PL intensity. (c) AFM profile of a bare nanopillar and a nanopillar that is covered by a WSe_2 flake. Adapted from Ref. [39]. <https://www.nature.com/articles/ncomms15053>. Licensed under CC BY 4.0.

Sometimes the transferred 2D TMDs flakes will not perfectly follow the surface morphology of the substrate, resulting in tent-like structures as illustrated in Figure 1. 10(c), therefore impeding the correct estimation of the strain. The local strain together with the funnel effect allows for accurate localization of the strain sites using PL mapping. One drawback of the method is that the strain cannot be tuned dynamically.

1.3.4 Diamond Anvil Cell

Diamond Anvil Cells (DACs) are powerful devices by which very high hydrostatic pressures of up to 39.2 GPa [84] can be applied to 2D materials. This technique allows for conducting *in-situ* optical characterization. Nayak and coworkers [84–87] used this technique to investigate MoS_2 , WS_2 , and the hybrid $\text{Mo}_{0.5}\text{W}_{0.5}\text{S}_2$, resulting in the first experimental evidence of the strain-induced semiconductor-to-metal transition.

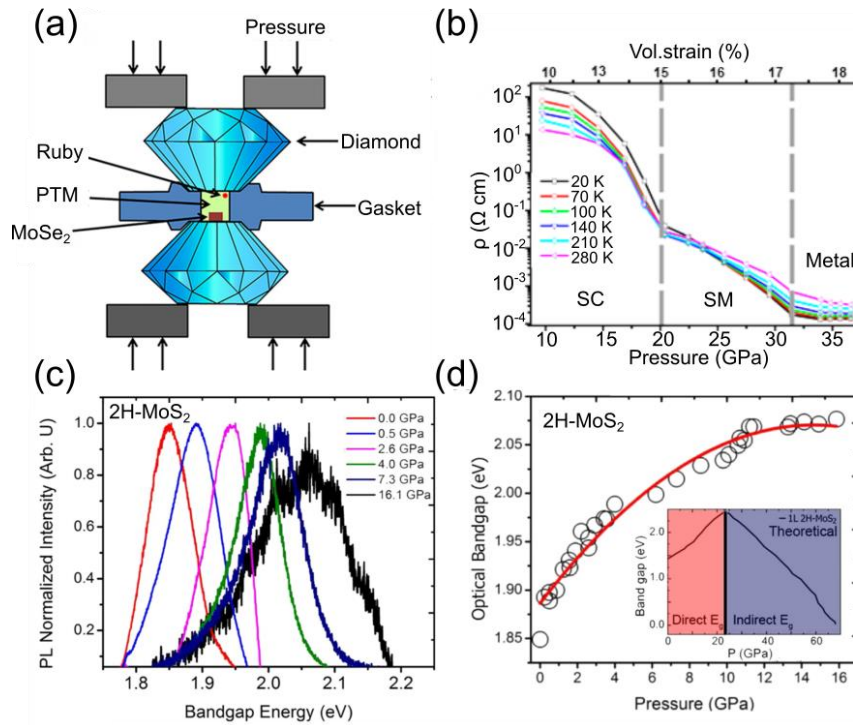


Figure 1. 11. Strain induced by DAC. (a) Schematic of the DAC with a MoS₂ flake inside. Ruby dot is the gauge monitoring the pressure. PTM is the pressure-transmitting medium. Adapted from Ref. [87]. Copyright (2017) American Chemical Society. (b) Phase transition with hydrostatic pressure. The change in resistance (ρ) denotes the phase transition from semiconductor (SC) to semimetal (SM) and metal. Adapted from [85]. Copyright (2015) American Chemical Society. (c) Spectral PL shift for different pressure. (d) Change of the optical band gap for different pressure. Figures (c,d) adapted from Ref. [84]. Copyright (2014) American Chemical Society.

The PL emission peaks of MoS₂ will blueshift with the increase of hydrostatic pressure (compressive strain). The A_{1g} peaks of the Raman spectrum show an obvious blueshift rather than a slight or no visible shift, because of the out-of-plane pressure component. With a DAC, compressive, but no tensile strain can be applied. Conveniently, the level of hydrostatic pressure can be measured by the gauge (red Ruby dot in Figure 1. 11(a)) in the chamber.

Similar band structure change (Figure 1. 11(d)), phase transition (b)), and PL peak shift (Figure 1. 11(c)) were also reported in the heterobilayer.[88]

1.3.5 Piezoelectric Actuators

The generation of strain by piezoelectric platforms is based on the inverse piezoelectric effect. Applying an electric field on piezoelectric material results in its mechanical deformation. Different types of strain (uniaxial, biaxial, or shear strain) can be applied, by

altering the crystal orientation and electrical or mechanical boundary conditions. Usually, the electric field is generated by applying a voltage to metal electrodes at the piezo. The resulting strain can then be transferred to a 2D material placed on top. This technique is a convenient way to induce strain in 2D TMDs in an independent and dynamically controllable way. For obtaining high electrostriction and therefore higher strain, relaxor ferroelectric crystals are typically used [36]. Lead magnesium niobate-lead titanate $(1 - x)[\text{Pb}(\text{Mg}_{1/3}\text{Nb}_{2/3})\text{O}_3] - x[\text{PbTiO}_3]$ (PMN-PT) is reported to have the highest piezoelectric charge coefficients [89], d_{33} , and d_{31} .

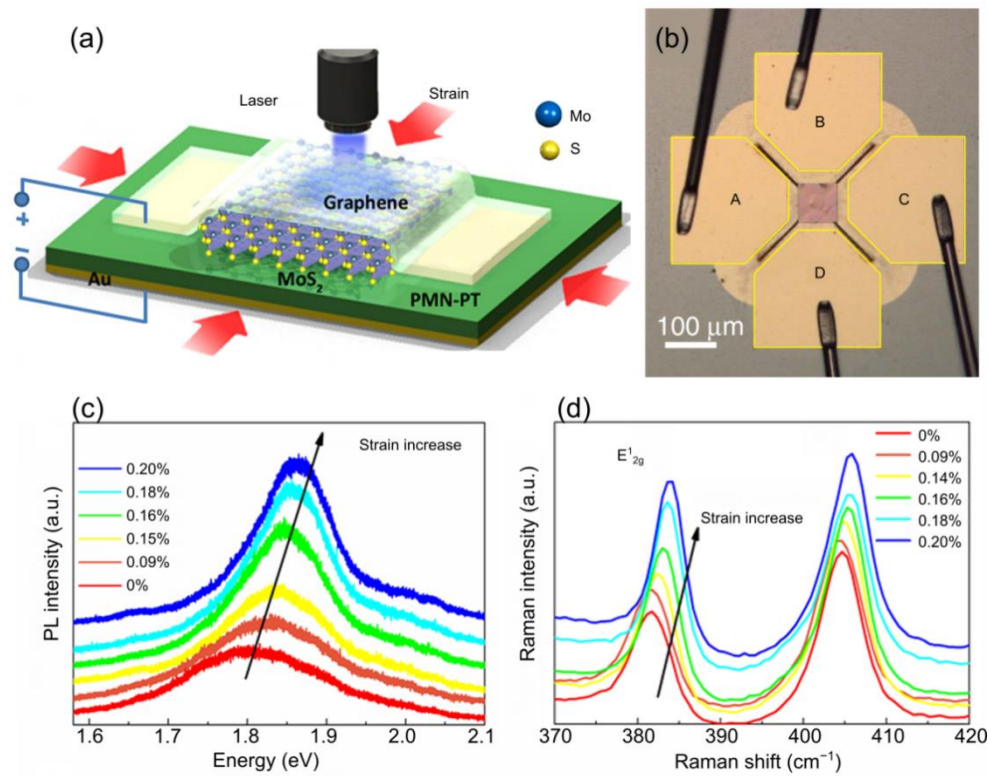


Figure 1. 12. Strain induced by piezoelectric actuators. Schematic of bulk (a) and optical image of a patterned (b) piezoelectric strain tuning platform. (a) adapted from Ref. [90]. Copyright (2013) by American Chemical Society. (b) adapted from Ref. [91].

<https://www.nature.com/articles/ncomms10387>. Licensed CC BY 4.0. (c) PL spectra of trilayer MoS₂ in dependence of compressive strain applied by a piezoelectric actuator. (d) Raman spectra of trilayer MoS₂ in dependence of compressive strain. Figures (c,d) adapted from Ref. [90]. Copyright (2013) by American Chemical Society.

In 2010, Ding and coworkers [36] applied this technique by investigating the properties of graphene in response to in-plane biaxial strain, as shown in Figure 1. 12. Different shifts in the observed Raman modes allowed the extraction of the Grüneisen parameters, in good

agreement with theoretical predictions. Hui and coworkers [90] placed a MoS₂ trilayer, sandwiched by a gold and graphene electrode, on a PMN-PT substrate, allowing for the application of biaxial isotropic compressive strain of up to 0.2%. MoS₂ showed a 200% increase in PL intensity, accompanied by about a 40% reduction in the linewidth of the emission. A blue-shift of the E_{2g}¹ and A_{1g} peaks in the Raman spectrum is observed, in contrast to the in-plane strain-tuning techniques mentioned before for which visible shifts of A_{1g} peaks are not detected. A further example of strain tuning of 2D TMDs with piezoelectric actuators is a report by Vamivakas and coworkers [92], showing the rotation of the polarization direction of defects in monolayer WSe₂ in response to strain.

The magnitude of the strain can be measured in different ways. One possibility is X-ray diffraction measurements [90] due to the changes in the lattice constant of the material. Hou and coworkers [93] obtained the amount of strain by creating micropatterned metallic strain gauges on top of the piezoceramic. By measuring changes in the electric resistance the amount of strain can be obtained by $K\varepsilon = \Delta R/R$, where R is the electric resistance and K is a pattern-specific coefficient.

Using piezoelectric strain-tuning platforms allows for much more than the application of in-plane isotropic biaxial strain. Piezoelectric single crystals can be (micro-) fabricated into more complex shapes, which can even allow control over the complete in-plane strain. Figure 1. 12 shows an illustration of anisotropic strain tuning platforms, consisting of four “legs” of the piezoelectric material that can induce biaxial and uniaxial strain simultaneously and independently. In this example, the strain was transferred to a semiconductor quantum dot containing membrane in the center of the device. Uniaxial strain can be achieved by applying a voltage to one pair of opposite contacts (AC or BD), and biaxial strain can be achieved by applying voltages on all contacts at the same time. One can switch between tensile and compressive strain by switching the voltage bias.

In comparison, piezoelectric crystals show some advantages over other techniques. The strain is easy to manipulate since this platform is controlled by a voltage (or electric field). Thereby strain can be generated “on-demand” in microstructured devices which is interesting for several applications. The small footprint also allows researchers to load it in cryo-chambers for low-temperature measurements. Furthermore, this versatile platform can induce uniaxial/biaxial, compressive/tensile, isotropic and even anisotropic strain. *In-situ*

characterization measurements (such as PL or Raman spectroscopy) are combinable with this technique.

1.4 Introduction of quantum dots

In this section, the physics of quantum dots (QDs) is discussed.

Richard Feynman said there is plenty of room at the bottom in 1959, pointing out a direction for the research in nano-physics. The nano-scale particles show great differences from their bulk counterparts.

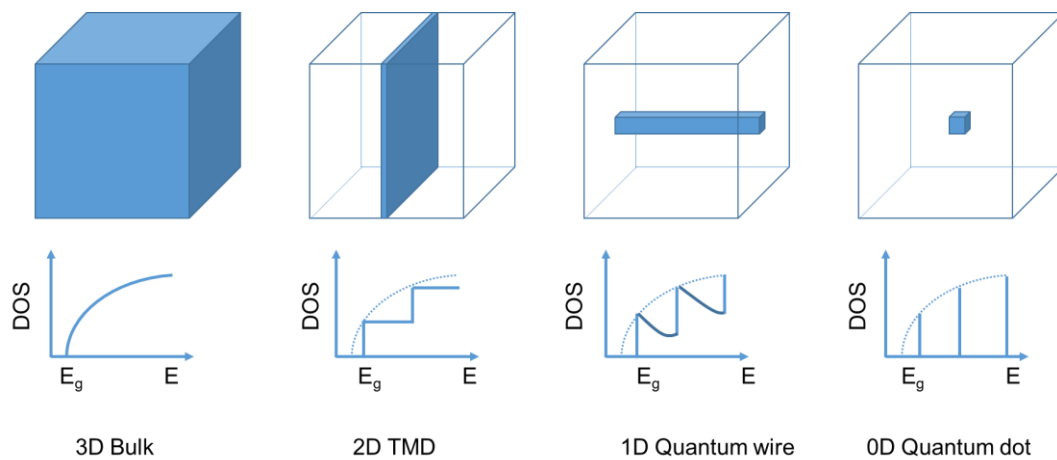


Figure 1. 13. Dimension-dependent density of states.

In the bulk scale, the DOS (density of states) increases in a continuous way, in 2D they are step stairs, finally, they go to discrete lines in 0D QDs.

QDs are confined in all directions. Their band gaps are controlled by their size or their confinement conditions. Generally, this equation below helps to understand the relationship between the size of and bandgap[94]

$$E(R) = E_{1g} + \frac{\hbar^2 \pi^2}{2\mu R^2} - \frac{1.8 e^2}{\epsilon R} \quad (1.6)$$

where, E_{1g} bandgap of the bulk materials, R is the radius of QDs, and ϵ is the permittivity.

Below, we discuss the growth, physical description, optical parameters, and the influence of strain on QDs. In the end, the effects of an electric field on QDs are added.

QDs can be acquired by more than one strategy. Here, we discuss the chemical solution quantum dot and self-assembled quantum dots growth by MBE or MOCVD/ MOVPE, including the S-K mode growth, local droplet etching and nanohole infilling method.

Here, the samples used in these works are grown via this mode.[95] The growth mechanism goes below.



Figure 1. 14. Sketch of local droplet etching and nanohole infilling. Adapted from Ref.[96] <https://www.nature.com/articles/ncomms15501>. Licensed under CC BY 4.0.

After wafer deoxidization, a sacrificial layer (AlAs) is first grown, for sake of the subsequent fabrication. Then, the barrier layer $\text{Al}_x\text{Ga}_{(1-x)}\text{As}$ is deposited. Different from the S-K mode growth, there is no strain left in the barrier layer because of no lattice mismatch between AlAs and GaAs. Then, we close the As shutter, only Al is deposited on the surface. Due to the concentration or chemical potential difference between the barrier layer and the Al droplet, the As (V group) inside the barrier and Al in the droplet begins to diffuse into each other, when the temperature is left to accelerate the diffusion. These operations result in some nanoholes in the matrix, and the next step is to fill the hole: GaAs are spluttered onto the surface. Subsequently, the top barrier layer is deposited to confine the quantum dots in vertical (growth) direction. The confinements of QDs in this growth mode can be controlled from several aspects: the size of the hole can be controlled via the temperature, diffusion time, and the Al droplet.

1.5 QDs Physics

In this section, the band structure and radiations of QDs are reviewed.

The lattice of GaAs belongs to the zinc blend family. GaAs has a direct band, which enables itself to emit photons. What interests us is the band structure around the Γ - point (original point of reciprocal space, k space). The major contributions come from one conduction and three valence bands, because all of them have the electron spin freedom $s=\pm 1/2$, which presents the 8-band structure[97] as below.

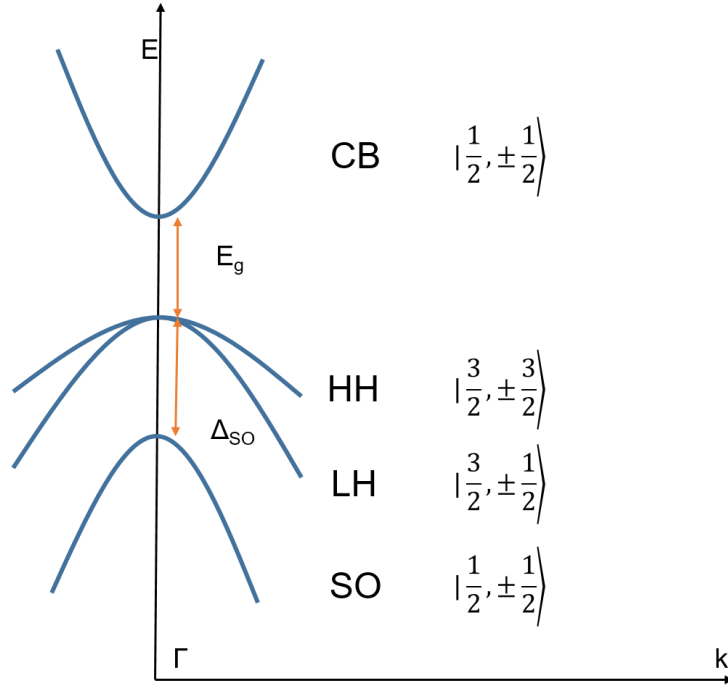


Figure 1. 15. Band structure of GaAs QDs.

The conduction band is separated from the valance bands by the bandgap, the corresponding energy is E_g . Conduction band holds the s orbit feature, and the orbital angular momentum is 0. Considering the contribution of electron spin, the electron states in the conduction band can be $|\frac{1}{2}, \pm\frac{1}{2}\rangle$. By contrast, valence bands share the p orbital feature, and their orbital angular momenta are 1. The spin-orbital coupling lowers down one of the energy states, annotated as SO in Figure 1. 15. Since this orbital has minor contributions to the optical properties, we will focus on the heavy holes (HH) and light holes (LH). The heavy holes get their names for their heavier effective mass than the light holes. Readers can also get this information from the band curvatures.

In the single-particle picture, once an electrode is excited into the conduction band, the corresponding excitons have these possibilities.

$$|\frac{3}{2}, -\frac{3}{2}\rangle_h |\frac{3}{2}, -\frac{1}{2}\rangle_e, |\frac{3}{2}, \frac{1}{2}\rangle_h |\frac{3}{2}, -\frac{1}{2}\rangle_e, |\frac{3}{2}, \frac{1}{2}\rangle_h |\frac{3}{2}, \frac{1}{2}\rangle_e, |\frac{3}{2}, \frac{3}{2}\rangle_h |\frac{3}{2}, -\frac{1}{2}\rangle_e.$$

The subscript (e or h) denotes the bound electron (hole) state. Of the four possibilities, the former two are dark states, because of the violence of angular momentum conservation. By contrast, the latter two can describe the excitons emitting photons, called bright states. Notably, the energies of the two bright states are not necessarily the same, because of the electron-hole exchange interaction. Their energy difference is called fine structure splitting (FSS), see below.

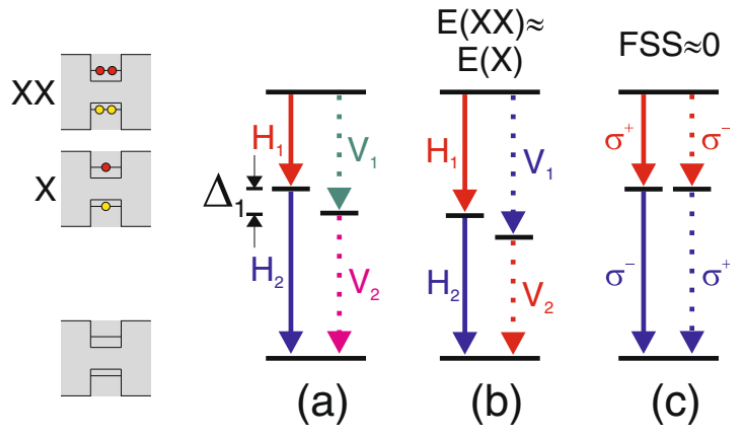


Figure 1. 16. Sketch of FSS and corresponding polarizations. On the left, the ground state, exciton, and biexciton are listed from the bottom to the top, corresponding to the different energy levels in the right columns. Δ_1 denotes FSS. Adapted with the permission from Ref. [98].

<https://nanoscalereslett.springeropen.com/articles/10.1186/1556-276X-7-336>. Licensed under CC BY 2.0.

| Quasiparticle/ state name | Charge config. | Quantum state | Spin state | Linear transitions | Circ. trans. flip | Spin Non- rad. |
|------------------------------|-------------------|------------------|---|-----------------------|--------------------------|----------------------|
| Biexciton | | $ XX\rangle$ | $ \downarrow\uparrow\downarrow\uparrow\rangle$ | | | |
| Negative trion | | $ X^- \rangle$ | $ u_h\rangle \alpha_h\rangle \otimes \frac{1}{\sqrt{2}}(\uparrow\downarrow\rangle - \downarrow\uparrow\rangle)$ | | | |
| Positive trion | | $ X^+ \rangle$ | $\frac{1}{\sqrt{2}}(\uparrow\downarrow\rangle - \downarrow\uparrow\rangle) \otimes u_c\rangle \alpha_c\rangle$ | HV | | |
| Exciton | | $ Y_b\rangle$ | $\frac{1}{\sqrt{2}}(\uparrow\downarrow\rangle + \downarrow\uparrow\rangle)$ | | | |
| | | $ X_b\rangle$ | $\frac{1}{\sqrt{2}}(\uparrow\downarrow\rangle - \downarrow\uparrow\rangle)$ | | | |
| | | $ Y_d\rangle$ | $\frac{1}{\sqrt{2}}(\uparrow\uparrow\rangle + \downarrow\downarrow\rangle)$ | | | |
| | | $ X_d\rangle$ | $\frac{1}{\sqrt{2}}(\uparrow\uparrow\rangle - \downarrow\downarrow\rangle)$ | HV | σ^+ σ^- | |
| Electron | | $ g^- \rangle$ | $ u_c\rangle \alpha_c\rangle$ | | | |
| Hole | | $ g^+ \rangle$ | $ u_h\rangle \alpha_h\rangle$ | | | |
| Ground state | | $ g\rangle$ | | | | |

Figure 1. 17 Sketch of radiative species and their spin and polarization states. Adapted with the permission from Ref.[99]. Copyright (2015) American Physical Society.

FSS breaks the polarization entanglement state and gives rise to the time dependence of the degree of entanglement[100]. In the polarization-encoded mode, all the states are summarized in the figure below, which indicates the potential of polarization-encoded qubits.[91]

1.6 Optical Parameters of QDs

In this section, we discuss some parameters to evaluate the optical properties of QDs. Considering the length limitation, only some of them will be briefly mentioned.

1.6.1 Lifetime and Coherence Time

Once excited, the electrons can go through multiple processes including radiative and non-radiative ones. What matters to us includes lifetime and coherence time. Lifetime describes the time period from excitation to radiative recombination, T_1 . During the lifetime of the excited electrons, they are likely to be elastically scattered by some impurities, and lattice vibrations then lose some characteristic information, while keeping the population intact. This pure dephasing process is T_2^* . Then, we get the total coherence time T_2 :

$$\frac{1}{T_2} = \frac{1}{2T_1} + \frac{1}{T_2^*} \quad (1.7)$$

Ideally, when there is no pure dephasing process, we can get this

$$T_2 = 2T_1 \quad (1.8)$$

The coherence time can be acquired from the Michelson interference experimental results, and the lifetime can be detected from the counting of high-time resolution APD.

1.6.2 Fine Structure Splitting

As the mechanism of FSS is discussed before, here, we just mention how the FSS can be acquired experimentally. As shown in Figure 1. 16, the recombination from bright states emits a linear polarized signal in the presence of FSS. We collect the X photon and access their peak position by Gaussian fitting. In this thesis, the FSS of our QDs are generally about a few to tens of μeV .

1.6.3 Second-order Time Correlation Function

One of the selling points for QDs emitters is their role as single-photon sources. Compared to the coherent laser, the photons from QDs show anti-bunching behaviors.

Probability can be described mathematically. Considering in a period T , the average photon number is \bar{n} . We divide the period T into N sections, thus in each section, the probability to find a photon goes as:

$$p = \frac{\bar{n}}{N} \quad (1.9)$$

Now the probability to find n photons in T is:

$$P(n) = \frac{N!}{n!(N-n)!} p^n (1-p)^{N-n} \quad (1.10)$$

$$P(n) = \frac{\bar{n}^n}{n!} e^{-\bar{n}}, n = 0, 1, 2 \dots \quad (1.11)$$

On the other hand, as the intensity is not a constant, the fluctuation of intensity is quantified by the standard deviation Δn :

$$\Delta n = \sqrt{\sum_{n=0}^{\infty} (n - \bar{n})^2 P(n)} \quad (1.12)$$

The photon statistics can be divided into three groups, super-Poisson, Poisson, and sub-Poisson distributed.

$$\Delta n > \sqrt{\bar{n}} \quad \text{Super - Poisson distribution} \quad (1.13)$$

$$\Delta n = \sqrt{\bar{n}} \quad \text{Poisson distribution} \quad (1.14)$$

$$\Delta n < \sqrt{\bar{n}} \quad \text{Sub - Poisson distribution} \quad (1.15)$$

Super-Poisson requires the fluctuation to be large enough. A typical example is thermal light, where the number of photons depends on the temperature. The standard deviation goes as:

$$\Delta n = \sqrt{\bar{n} + \frac{\bar{n}^2}{N}} \quad (1.16)$$

Correspondingly, a bunching effect is present in terms of photon stream.

Poisson distribution requires the fluctuation to be equal to the probability. A typical example is the coherent laser, with the classical intensity fluctuation on a time-scale determined by the coherence time. Corresponding the photon stream goes below.

Sub-Poisson requires the fluctuation should be small enough. A typical example is the light from quantum dots. As the 3-dimensional confined particle, QDs hold a discrete density of state. Pauli exclusion requires only one particle in each state, which determines that each photon is not accompanied by others. The picture of the photon stream goes below.

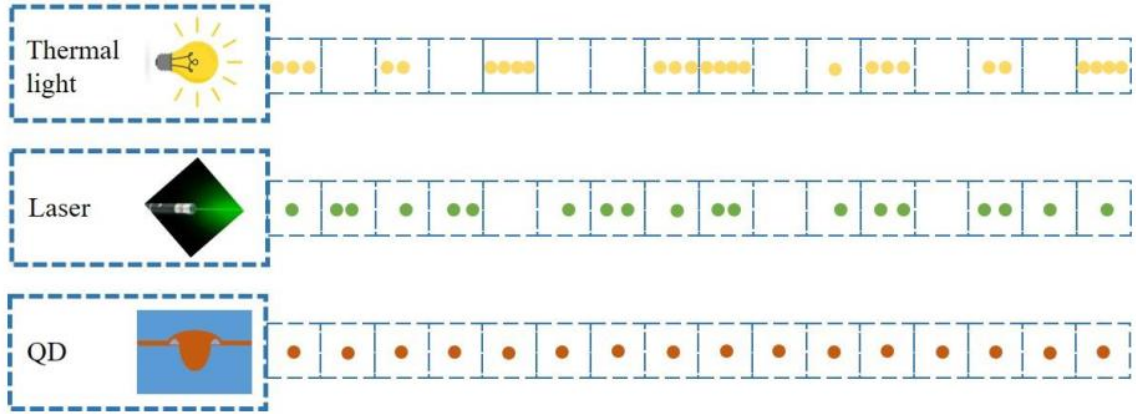


Figure 1. 18 Schematic of photon streams for super-Poisson, Poisson, and sub-Poisson light. Note the stream here is different from the sketch for laser cavity operation. This figure is adapted from Xin Cao's dissertation, with permission from Dr. Xin Cao.

In our experiments, this property can be evaluated by the second-order (auto)correlation function:

$$g^{(2)}(\tau) = \frac{\langle I(t)I(t + \tau) \rangle}{\langle I(t) \rangle \langle I(t + \tau) \rangle} \quad (1.17)$$

where the τ is the interval between two beams of signals, and I is the intensity. Sharp bra means the average of the item inside. Experimentally, it can be obtained by a Hanbury-Brown and Twiss setup. For continuous wave and pulsed laser excitation, their corresponding results are different.

1.7 Influence of Strain on QDs

In 2D TMDs section, we discuss a math description of in-plane strain. For quantum dots devices, the model applies here.

The strain's function is to affect the lattice constant and symmetry. According to the band theory, the distance of atoms determines the communization of outmost shell electrons, then the band properties. This indicates the influence of strain can be quite fundamental and universal.

In this case, the band structure goes as below, in response to strain:

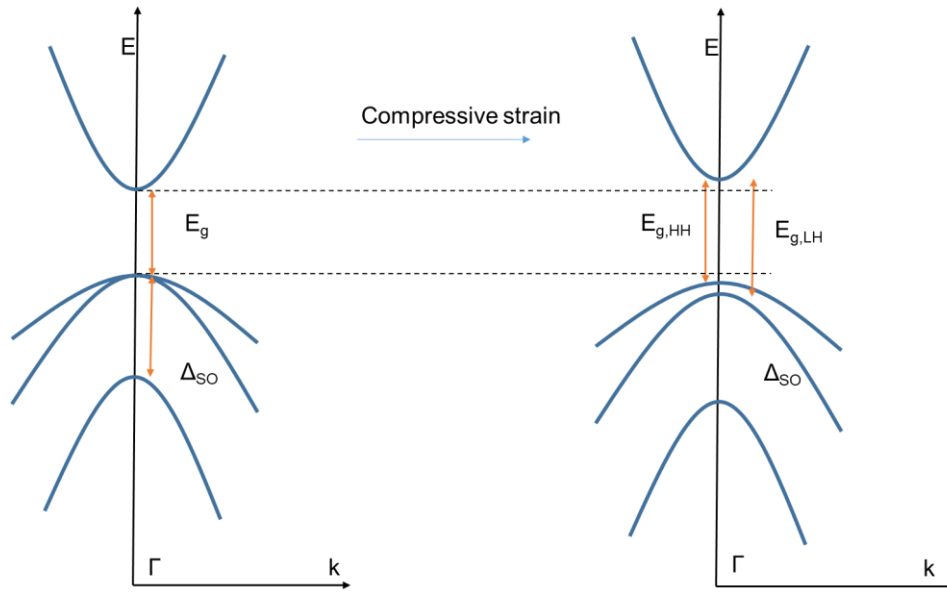


Figure 1. 19. Band structure without and with compressive strain.

The bandgap will expand to a compressive strain, within a certain range.[101] As well, band degeneracy of heavy holes and light holes [102] at Γ point will be lifted. Both aspects have been confirmed by the experiments.[103,104]

Symmetry can be altered by the anisotropic strain. As discussed before, GaAs holds a zinc blend structure: each Ga (As) atom is coordinated by four As (Ga) atoms, and this tetrahedron (central Ga and three As atoms nearby, and vice versa) shows a C_3 in-plane projection. When subjected to an anisotropic strain, such as a uniaxial strain, the C_3 can reduce to C_{2v} even to C_1 . By contrast, an anisotropic strain cannot make it.

Generally, we can understand the vertical projection of nanoholes as an ellipse[105], which corresponds to a similar shape of wavefunction or dipole. As shown below the anisotropic can interaction with the dipole: A compression strain can change an ellipse projection to a regularly circular one. This process is accompanied by the ellipse deformation and rotation, which corresponds to the change of FSS and phase.[91]

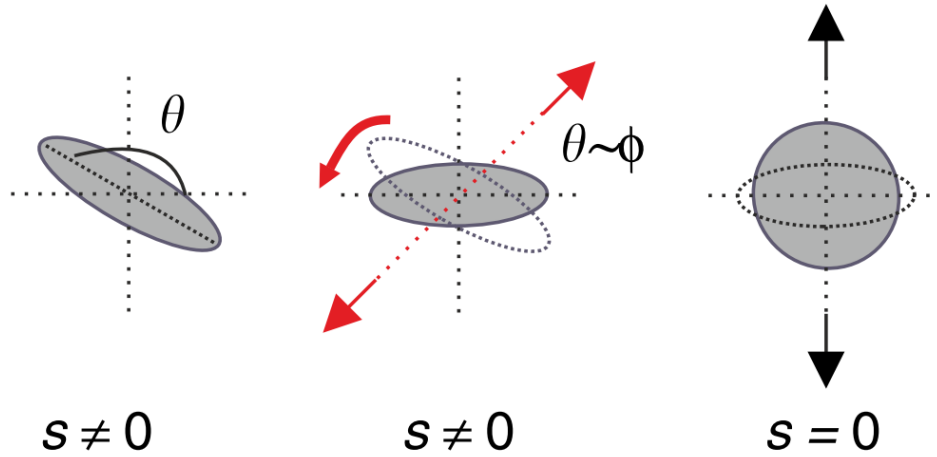


Figure 1. 20. Sketch of strain's effect on QDs. Adapted from Ref.[106].

<https://www.nature.com/articles/ncomms10375>. Licensed under CC BY 4.0.

1.8 Summary of details

In this section, important details, including the findings and status of the work in this thesis, are summarized.

1.8.1 Research topic

In this thesis, the focus is on the interaction of strain with low-dimensional emitter systems. Compared with their bulk counterparts, low-dimensional (2D or 0D) systems show different responses to an external strain.

Single atomic layer WSe₂ and three-dimensionally confined GaAs/AlGaAs quantum dots are chosen. On one hand, they show some differences in the degrees of freedom, distribution of emitters, orientations of their dipoles,[107,108], and band structures.[8,105] On the other hand, these differences can be associated with some similarities, the interaction of band gap with strain,[47,106] and the format of Hamiltonians (Pikus-Bir Hamiltonian).[109,110]

Technically, we integrate strains of different configurations with the low-dimensional emitter systems. Monolithic piezoelectric platforms, including biaxial and uniaxial ones, and MEMS platforms are used, which acts as another line to unify all the research.

1.8.2 Motivation

From the state-of-the-art in sections 1.1-1.7, we know the general knowledge of the 2D TMDs and 0D QDs low-dimensional system. Both of them are regarded as promising candidates for the (quantum) optical application.[111]

2D TMDs, as a hotspot of scientific research these days, couple helicities of light with the valleys, so-called valleytronics.[112] Research on this topic benefits the envisioned information storage and treatment.[112] However, the physical understanding of this system is not deep enough. Strain, as a more suitable probe, will help to understand the physical process in terms of distance change and symmetry change.

Meanwhile, 2D TMDs can also emit some non-classical light,[113] which manifests its potential for quantum optical application.[111] In this aspect, QDs are more promising. Related optical circuits and cavities[114] have been developed to assemble QDs into a functional emitter system. Unfortunately, as-grown QDs samples are accompanied by the notorious fine structure splitting.[106] Strain is a nice choice to tackle this issue, at the same time tuning the emission wavelength in a fine resolution.[115]

The (quantum) optical application of both drives researchers to investigate the physical process, which is the platform where strain can play a role.

1.8.3 Structure of this thesis

Chapter 1 presents the readers the start-of-the-art, by discussing the structure and properties of 2D TMDs, describing the effects of strain and strain tuning techniques. These sections are published in the *Zhao An, Michael Zopf, and Fei Ding. (2022) Strain-Tuning of 2D Transition Metal Dichalcogenides, in Nanomembranes, John Wiley & Sons, Ltd, pp. 413–448.* The discussion on QDs is added to depict the readers a picture of the research status.

Chapter 2 presents some experimental details, which apply to all the results discussion. So in Chapters 3, 4, and 5, the setups will not be explained in detail. Readers can focus on the results and discussion.

Following the research topic and motivation mentioned above, three investigations are described in chapters 3, 4, and 5. **The findings, related significance, status of the work, contributions, and limitations of the work are declared.**

Chapter 3 presents the first result of this thesis. It discusses research on a biaxial strain and the influence of the scattering process in monolayer WSe₂ and MoSe₂. Here, we integrate polarization-resolved photoluminescence spectroscopy with a cryogenic strain-tuning technique to investigate this process in WSe₂ and MoSe₂. We record different dependence of trions and excitons on the biaxial strain: the decreases in helicities of excitons are attributed to the intervalley scattering, affected by e-h exchange interaction. The stability of MoSe₂

trions is related to band structure forbidden scattering. The WSe₂ trion scattering is described in a rate equation model, which agrees well with observations. Our results help to understand more about the manipulation of valley depolarization and facilitate the development of practical devices.

Parts of Chapter 3 are written in the manuscript *Strain control of exciton and trion valley depolarization in monolayer transition metal dichalcogenides*, Zhao An, Pedro Soubelet, Michael Zopf, Alex Delhomme, Chenjiang Qian, Yaroslav Zhumagulov, Paulo. E. Faria Junior, Jaroslav. Fabian, Frederik Benthin, Xin Cao, Andreas V. Stier, Fei Ding, and Jonathan J. Finley.

This work is synergetic: the project is supervised by Prof. Dr. Fei Ding and Prof. Dr. Jonathan J. Finley. The sample is exfoliated by Dr. Pedro Soubelet, and assembled by Zhao An. Data is collected by Zhao An and Dr. Pedro Soubelet. Dr. Pedro Soubelet and Zhao An did the data analysis. Dr. Andreas Stier, Dr. Michael Zopf, Prof. Dr. Fei Ding, and Prof. Dr. Jonathan J. Finley join the data analysis and discussion. The rate equations model is developed by Dr. Pedro Soubelet and supported by Dr. Yaroslav Zhumagulov, Dr. Paulo E. Faria Junior, and Prof. Dr. Jaroslav Fabian. *Ab initio* calculation and modeling are done by Dr. Yaroslav Zhumagulov, Dr. Paulo E. Faria Junior, and Prof. Dr. Jaroslav Fabian. Yvo Barnscheidt did a Raman measurement. Dr. Alex Delhomme, Dr. Chenjiang Qian, Dr. Xin Cao, and Fredrik Benthin offer necessary help in the measurement or data analysis. Dr. Pedro Soubelet contributes equally to Zhao An.

Chapter 4 presents an interaction of anisotropic strain with wavefunction of exciton in monolayer WSe₂. In this chapter, we integrate the dynamic strain-tuning technique with micro photoluminescence to investigate the fine structures of neutral exciton in monolayer WSe₂. We first identify the fine structures of exciton by the polarization-dependent spectrum and then record the nonlinear responses of exciton fine structure to anisotropic strain, which is interpreted by its interaction with exciton wavefunction. Our study draws a picture of the manipulation of wavefunctions, shedding light on a deeper understanding of WSe₂.

Parts of this chapter are prepared for the manuscript: *Manipulation of WSe₂ exciton fine structure by anisotropic strain*. Zhao An, Jonas Bauer, Mikhail Glazov, Alexey Chernikov, Pengji Li, Jingzhong Yang, Eddy P. Rugeramigabo, Michael Zopf, Kaiqiang Lin, and Fei Ding.

Prof. Dr. Fei Ding and Prof. Dr. Kaiqiang Lin coordinate the research. Jonas Bauer and Zhao An fabricate the sample and collect the data. Zhao An analyzes the collected data. Prof. Dr. Mikhail M. Glazov contributes the quantitative model to fit the results. Prof. Dr. Fei Ding, Prof. Dr. Kaiqiang Lin, Prof. Dr. Mikhail M. Glazov, Prof. Dr. Alexey Chernikov, and Dr. Michael Zopf join the discussion of results. Zhao An, Prof. Dr. Mikhail M. Glazov, Dr. Michael Zopf, and Pengji Li help in the fitting of the data. Dr. Jingzhong Yang joins the discussion on general scientific issues. The authors feel thankful for the discussion of results with Prof. Dr. Jonathan, J. Finely, Prof. Dr. Rolf J. Haug, Dr. Andreas Stier, Dr. Lina Bockhorn, Dr. Pedro Soubelet, and Bei Zheng.

Chapter 5 is to discuss a 2-leg MEMS platform and its effect on the quantum dot, whose emissions are around the zero phonon line of negatively charged silicon vacancy color centers in diamond. Here, we integrate a compact piezoelectric actuator with GaAs quantum dots embedded membrane, whose emission is around the zero phonon line of silicon vacancy. In the cryogenic photoluminescence spectrum, we observe two different trions from the same quantum dot and find their binding energies show opposite evolutions with a strain. Our work deepens the understanding of quantum dots at zero phonon line of silicon vacancy and facilitates the development of compact devices for the hybrid communication system. This system applies to the 2D TMDs emitter system.

The corresponding manuscript is in preparation, *Strain-induced modulation of quantum dot emissions at Si-Vacancy transitions*, Zhao An, Xin Cao, Jingzhong Yang, Maik Steinbach, Jürgen Koch, Peter Jäschke, Eddy P. Rugeramigabo, Fredrik Benthin, Rolf Haug, Michael Zopf, and Fei Ding.

Prof. Dr. Fei Ding and Zhao An designed the experiment. MEMS piezoelectric platform is designed by Zhao An, and fabricated by Maik Steinbach, Jürgen Koch, and Peter Jäschke. The quantum dots sample is grown by Dr. Xin Cao. Semiconductor membranes are fabricated by Zhao An, with great help from Prof. Dr. Rolf Haug. Optical measurements are conducted by Zhao An and Dr. Xin Cao, with the help of Jingzhong Yang and Fredrik Benthin. Zhao An analyzes the data, with instruction from Prof. Dr. Fei Ding, and Dr. Michael Zopf joining the result discussion. The formal manuscript for journal publication is written by Zhao An, and revised by Dr. Xin Cao, Dr. Jingzhong Yang, and Dr. Eddy P. Rugeramigabo.

In the rest of the dissertation, the **conclusion and outlook** are added. Throughout this work, the effects of strain on low-dimensional emitters are associated with the particles inside, such as excitons or trions, which show features related to their confinements, and band structures.

The shortcomings of this work are discussed: Compared to the interaction of strain with neutral exciton in WSe₂, the interaction of trions with strain is still not clear. We tried to give a description of the scattering process, the physical process needs to be unveiled. Technically, the piezoelectric platforms need to be optimized to an amplifier strain range and more versatile strain configurations.

2. Technology

In this chapter, the basic information of the setup and fabrication technique are discussed, so in the subsequent chapters, readers will not be distracted from the discussion of the results.

2.1 Light Path

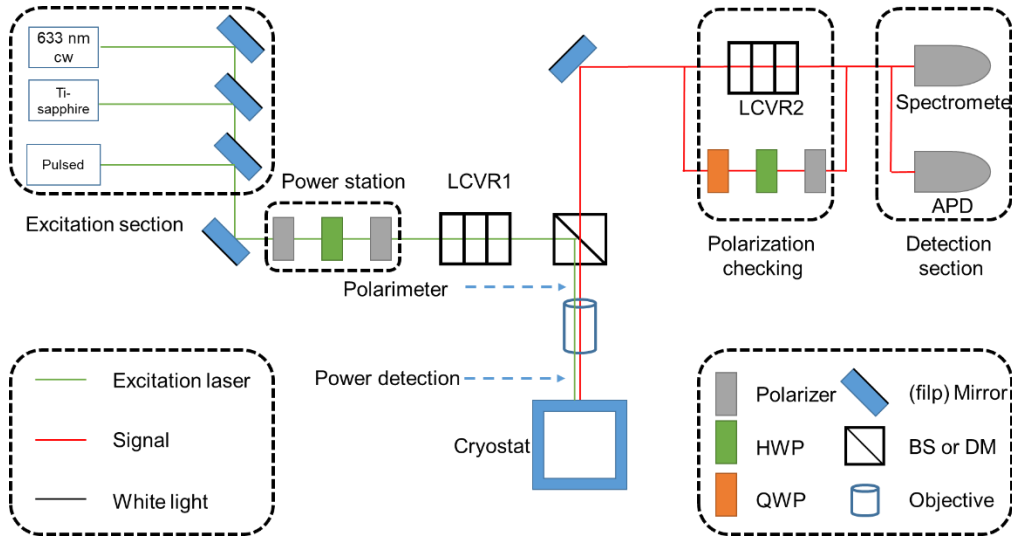


Figure 2. 1. Sketch of the PL measurement setup. HWP, QWP, BS, DM, and LCVR mean half-wave plate, quarter-wave plate beam splitter, dichroic mirror, and liquid crystal retarder, respectively.

Figure 2. 1 is the sketch of the main setup in Hannover. Some of the results in the subsequent chapters are measured in the partners' labs. Their setups are different to some extent, however, the most critical parts are similar.

2.1.1 Power Modulation

In the excitation section, different lasers can be used to excite the sample. Power can be modulated by the power station or the insertion of OD filters. In our experiments, the power is tuned at a proper level, although we can achieve saturation. To approach the real power on the sample, a detector is placed between the objective lens and cryostat, see Figure 2. 1. In most cases, wavelengths of signals for 2D TMDs locate at $720 \text{ nm} \pm 50 \text{ nm}$, on our spectrometer (Acton SpectraPro Sp-2750 with Pixis 400BR camera, Princeton instruments) the counting efficiency is quite high and stable. This spectrometer applies to the QDs in this thesis, around 737 nm .

2.1.2 Polarization and Etaloning Effect

Polarization is a critical parameter in this series of experiments. In this setup, the aberrations of polarization states derive from these aspects, the depolarization of mirrors, beam splitter, gratings of the spectrometer, and wavelength-dependent depolarization. To obtain accurate measurements, care was needed to ensure that the pump light arriving on the sample is circularly polarized and also that the measured components of the PL truly corresponded to the two circularly polarized components of the light emitted from the sample. In the excitation beam, we use silver mirrors instead of dielectric mirrors. At the same time, liquid crystal retarders to pre-compensate depolarization by the mirrors. For the wavelength-dependent depolarization, we use a polarimeter after all the mirrors to detect polarization states to guarantee precision. In the connection of the excitation and collection light path, we replace the beam splitter with a dichroic mirror. In the collection path, we put a polarizer to unify the depolarization effect of the mirrors before the spectrometer, so the effect of the grating will not make a big difference.

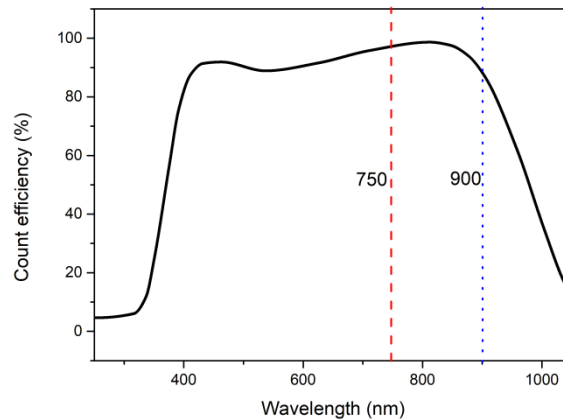


Figure 2. 2. Count efficiency of Pixis 400 BR CCD Camera. (Data from Principle instruments)

The last phase in the signal collection is the counting by CCD camera. Unfortunately, the emission wavelength of the heterobilayer $\text{WSe}_2/\text{MoSe}_2$ sample is just around 900 nm, which means our signals are bothered by the so-called ‘etaloning effect’. Compared to the front-illuminated CCDs, back-illuminated CCDs have much higher quantum efficiency, generally above 95%. This originates from the exposed active photon sensitive layer (Si, reflective index 4) and AR coatings, while this structure together with the insulation layer (SiO_2 , reflective index 1.4) to electric connections below the active layer assembles into a F-P cavity. This cavity is usually 10–15 μm in width, which constructs or destructs the photons

around NIR, finally, presenting a periodical fluctuation in the collected signals, i.e. fringe. In our experiment, a tungsten halogen lamp is used to calibrate the ‘etaloning effect’ as well as the wavelength dependence quantum efficiency.

2.2 Fabrication of Emitters

2.2.1 Fabrication of 2D TMD

In these works, all the 2D TMDs samples come from partners from Dr. Pedro Soubelet (TUM) or Jonas Bauer (University of Regensburg) and Prof. Dr. Kaiqiang Lin (University of Regensburg, now Xiamen University). Their contributions will be specified in corresponding chapters.

2.2.2 Fabrication of QDs Embedded Nanomembrane

For the QDs, the fabrication in this work starts from the as-grown QDs sample with a sacrificial layer, grown by Dr. Xin Cao.

The fabrication follows this chart:

Before the chemical etching, designed masks need to be deposited on the wafer. Notably, in this step, the mask is carefully aligned with the crystal orientation $\{110\}$ (cleavage plane) family.

First, we use the piranha solution to do a non-selective etching. With the protection of the mask layer, the sample will be etched vertically with some etching width, see phase 2.

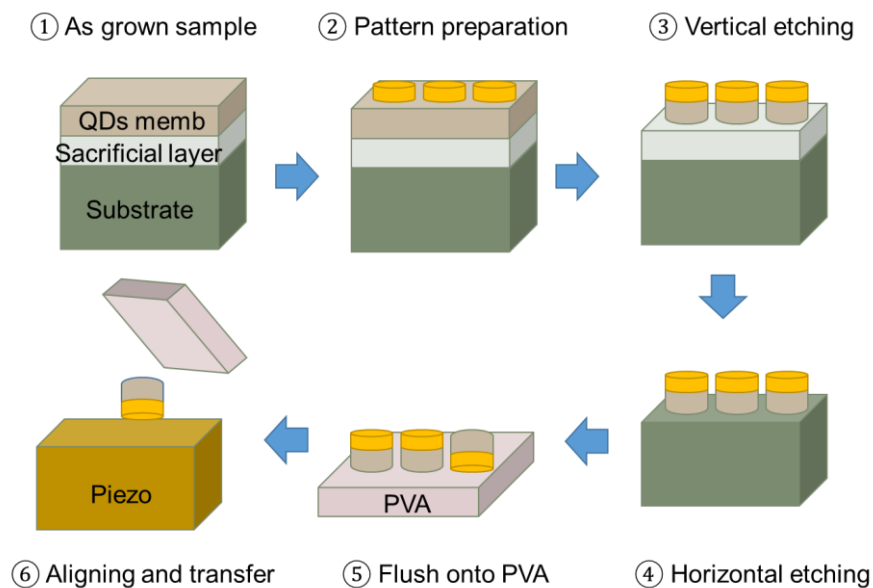


Figure 2. 3. Fabrication process chart of QD nanomembranes.

Second, the etched samples will be soaked into the HF solution to do a selective etching, because HF will attack the AIs sacrificial layer instead of the barrier layer.

Third, after dilution in water, the etching membranes are flushed onto a film made of PVA.

Then, the selected membranes are carefully aligned with the piezoelectric actuator.

At last, the aligned device is soaked into a water beaker, until PVA is dissolved. Then the membrane is transferred onto the piezoelectric actuator.

2.3 Fabrication of Piezoelectric Actuator

In this work, different types of piezoelectric actuators are used. All the functionalities of them are based on the inverse piezoelectric effect: piezoelectric materials transform electric power (electric voltage) into mechanical power (deformation or strain). Below, we discuss the types of actuators used in the subsequent chapters and their corresponding strain features.

2.3.1 Bulk Biaxial Piezoelectric Single Crystal

In this work, all the piezoelectric materials are PMN-PT (lead magnesium niobate-lead titanate), as a relaxor ferroelectrics, which shows the highest piezo-response.[116] Below Curie temperature, PMN-PT is a low-symmetry crystal structure and can be rhombohedral (R) or tetragonal (T) phases with different compositions of PMN and PT. The best piezoelectric response lies in the R zone close to the T zone, the boundary between them is called morphotropic phase boundary (MPB). Readers interested in this aspect are recommended to refer to the phase diagram of PMN-PT. Interestingly, the highest poling direction is **not** the spontaneous poling direction $\langle 111 \rangle$, but $\langle 100 \rangle$, because the electric field can induce engineered domains. Compared to the normal domains, the engineered domain has smaller hysteresis, and much higher piezoelectric constants[117]. This is why the R phase $\langle 100 \rangle$ cut PMN-PT is chosen and poled in the isotropic strain tuning research.

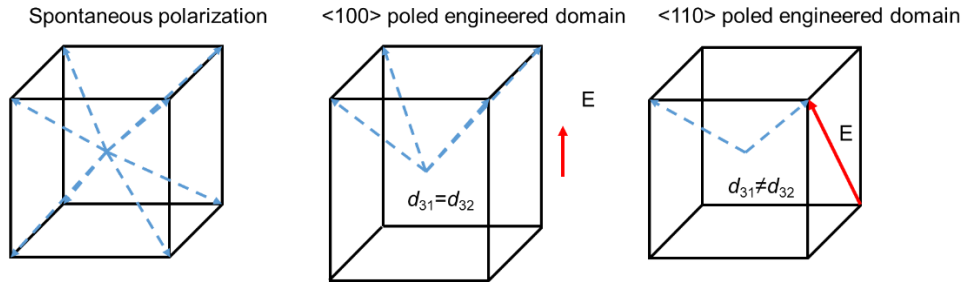


Figure 2. 4. Sketch of engineered domains on $\langle 100 \rangle$ and $\langle 110 \rangle$ orientations. The blue dashed line denotes $\langle 111 \rangle$ direction. Red arrows denote the direction of the electric field, the central one is along $\langle 100 \rangle$, and the last one is along $\langle 110 \rangle$.

These kinds of crystals can generate biaxial or isotropic in-plane strain. In our work, the bulk biaxial piezo is with 200 nm gold coated at both sides of the 300 μm thick PMN-PT.

2.3.2 Bulk Uniaxial Piezoelectric Single Crystal

Compared to the biaxial one, the uniaxial piezo owns a different crystal orientation, normal to the macro surface is $\langle 110 \rangle$ rather than $\langle 100 \rangle$. Recent research shows the poling along $\langle 110 \rangle$ of R phase and T phase PMN-PT can also induce nice piezoelectric responses. [118–120]

An interesting feature of this piezo is the anisotropic in-plane response, which can change the crystal symmetry and change the lattice constant.

2.3.3 Laser Cut Piezoelectric Single Crystal

Though the PMN-PT is the highest piezoelectric response material, the typical piezoelectric constant d_{33} is about 2700 pC/N.[121] 2D TMDs on the bulk material cannot generate a drastic shift, on the other hand, the strain configurations by the above two actuators are not versatile. Customized anisotropic strain is on demand. Here, the microelectromechanical systems (MEMS) of the piezoelectric platform are fabricated by laser cutting.

In my works, 2-leg, 4-leg, and 6-leg platforms are fabricated to apply uniaxial, biaxial, and triaxial in-plane strain onto QDs membranes or 2D materials. Till now, only the uniaxial laser cut film piezoelectric platform with QDs membranes gives some experimental findings, see chapter 5. Further discussion of the functionality of those platforms will be conducted there.

2.4 Electric Tuning Strategy

Whether in QDs systems or 2D TMDs emitter systems, electric fields are one of the most popular tuning strategies. Due to their reduced dimensions, the vertical electric field is easier to apply. However, we should not ignore the possibility of a lateral electric field.

For QDs, the electric dipole has a major component along the out-of-plane direction.[107] In our research, the effect of the lateral effect is limited. While for monolayer TMD, the case is contrasting: the intrinsic dipoles are in-plane. The lateral electric field will likely bring something new.

Here, we introduce how lateral electric electrodes are fabricated.

2.4.1 Lateral Electrodes for QDs Nanomembranes

Here, interdigital structures are patterned on the as-grown GaAs/AlGaAs wafer or selected substrates (Al_2O_3 , SiO_2 , high-resistance Si/SiO_2) by standard lithography, deposition, and liftoff operations.

2.4.2 Lateral Electrode for 2D TMDs

In the research of 2D TMDs, gate tuning is most investigated. In principle, it can apply an electric field or dope sample (negatively or positively) by controlling the power suppliers.

Here, we use the high dielectric strength HfO_2 as the insulation layer between metal electrodes and WSe_2 , to suppress the doping effect.

The fabrication flows this chart.

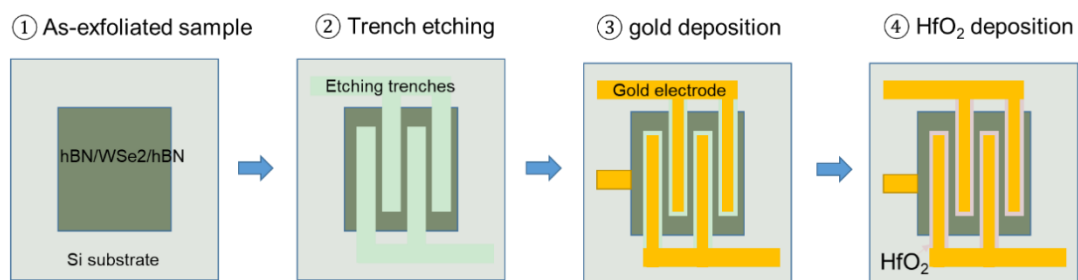


Figure 2. 5. Sketch of lateral electrode fabrication.

We start from a piece of as-exfoliated monolayer WSe_2 sample on a high-resistance Si substrate: WSe_2 is encapsulated by multiple layer hBN flake, and the Si substrate is patterned with marker array for position recognition. We determine the height or thickness of the deposition layer by AFM measuring the step on the edge of the hBN flake.

Then, we did the first EBL and RIE etching to define the trenches for gold and HfO_2 .

Subsequently, we check the etching results by EDX to guarantee the hBN and WSe₂ layer is completely removed.

After this, we did the second EBL as well as the gold deposition to define the gold fingers.

Next, we did the third EBL and HfO₂ deposition to define the HfO₂ insulation layer between the gold electrodes and WSe₂, in case of direction contact of them.

In this fabrication, position-recognition EBL technology is used to help us to deposit materials at the required place. The corresponding resolution is higher than the writing critical dimensions of the electron beam.

3. Strain control of exciton and trion valley depolarization in monolayer transition metal dichalcogenides

In this chapter, we start to discuss the effect of strain on 2D WSe₂ monolayer. As discussed before, strain can exert some influence on lattice constants and/or symmetries. Here, we start from the basic case, biaxial/isotropic strain integration with monolayer WSe₂.

Part of the results are prepared in the manuscript: Strain control of exciton and trion valley depolarization in monolayer transition metal dichalcogenides, Z. An, P. Soubelet, Y. Zhumagulov, M. Zopf, Delhomme, C. Qian, P. E. Faria Junior, J. Fabian, F. Benthin, X. Cao, A. V. Stier, F. Ding, and J. J. Finley.

Monolayer transition metal dichalcogenides gain much attention, as a platform for valleytronics and potential media for information storage. Behind them are the optical features of multiple complexes, determined by relaxation and dynamics. Here, we integrate polarization-resolved photoluminescence spectroscopy with a cryogenic strain-tuning technique to investigate this process in WSe₂ and MoSe₂. We record different dependence of trions and excitons on the biaxial strain: the decreases in helicities of excitons are attributed to the intervalley scattering, affected by e-h exchange interaction. The stability of MoSe₂ trions is related to band structure forbidden scattering. The WSe₂ trion scattering is described in a rate equation model, which agrees well with observations. Our results help to understand more about the manipulation of valley depolarization and facilitate the development of practical devices.

3.1 Introduction

Monolayer transition metal dichalcogenides (ML TMDs), provide a superb platform for the research of valleytronics and relevant potential applications for information storage.[112] Compared to their bulk counterparts, ML TMDs show contrasting differences in optical performances, such as strong light-matter interaction, circularly polarized excitation, and detection.[22] Due to the reduction of dielectric screening, trions have been reported.[122–124] Behind the optical performance are the optical selection rules and the locking of exciton spin polarization σ^+ (σ^-) with K (K') valley.[22] Experimentally, the observed degree of circular polarization (Dop) or helicity is from the ideal case, 100%.[125] An unavoidable

process is a relaxation, scattering of excitons, and their interactions with excess charges.[126,127] Our investigation of this process is of great significance for the demanding dynamic control of valley depolarization.[128]

WSe₂, together with MoSe₂ is among the most investigated TMDs. Interestingly, the band structure[5] of WSe₂ leads to the occupancy of the excited electrons in the upper branch of the conduction band. Besides, the neutral exciton in WSe₂ (X_W) can couple with an extra electron in the same or different valleys, comprising a singlet (triplet) negatively trion or trion, T_s (T_t). In cryogenic temperature photoluminescence (PL) spectrum, they are separated by the 6-7.5 meV.[112,129] In contrast, MoSe₂ presents only one high-intensity trion peak, which corresponds to the unique composition of trion: the exciton can only couple with an excess electron in the different valleys. This regime presents a Rashba-type mixing of the bright exciton (X_{Mo}) and dark exciton[130], giving rise to the high intensity of trion (T) peaks. The band structures of WSe₂ and MoSe₂ act as the foundation for exciton relaxation, scattering, and interactions with electrons. The corresponding optical features are the natural choice to investigate this process and its influence on valley depolarization.

In this letter, we integrate a cryogenic strain-tuning technique with polarization-resolved micro-PL spectroscopy to investigate the dynamics of ML WSe₂ and MoSe₂. We record different dependence of Dops on our biaxial strain. In MoSe₂, the Dop of X_{Mo} decreases with our biaxial strain, while that of T is almost intact. Concurrently, the X_W , T_s , and T_t all show monotonic decreases with strain, though their dynamics are of great difference. The scattering of X_W is similar to that of X_{Mo} , related to e-h exchange interaction. The behaviors of T_t and T_s are depicted in our rate equation model, which agrees well with the observations. Our results shed light on a deeper understanding of the dynamics and facilitate the manipulation of valley depolarization.

3.2 Sample fabrication

Figure 3. 1(a) presents the sketch of our samples. Monolayer TMDs (WSe₂ or MoSe₂) are exfoliated from the bulk crystals, before encapsulation by the top and bottom hBN flakes. The process is a standard dry-transfer technique,[131] similar to the reports on Si/SiO₂ substrate. Our monolithic piezoelectric actuator is made of a <100> cut PMN-PT (lead magnesium niobate–lead titanate) single crystal, with both sides coated with gold electrodes,

$R_a < 5\text{nm}$. In the cooling down process, the piezoelectric actuator is poled by high voltages, with the top electrode grounded to avoid the possible electric doping effect.

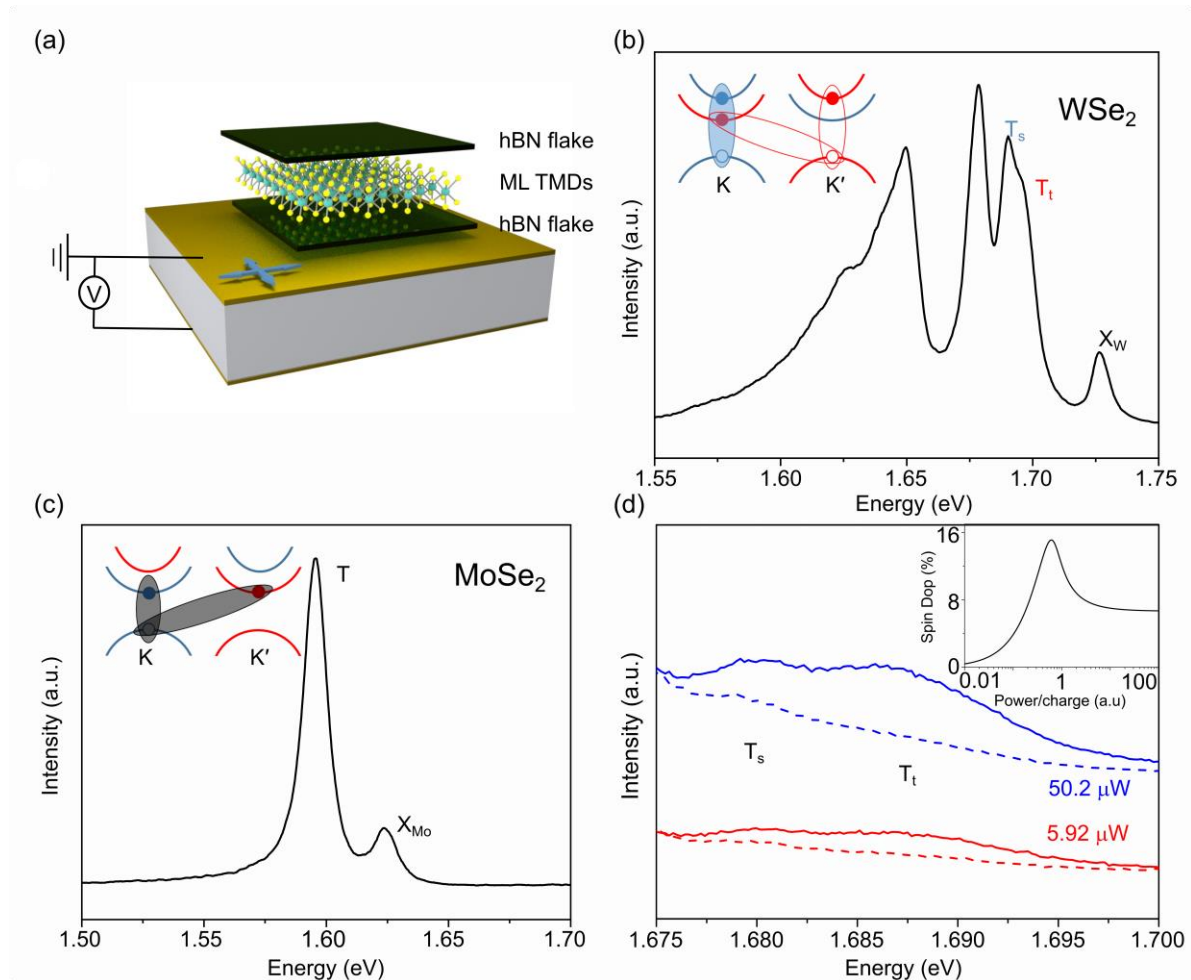


Figure 3. 1 a), Sketch of the sample, consisting of a multiple layer hBN flake encapsulated ML TMDs, which can be monolayer WSe₂ or MoSe₂. The arrows in the bottom left denote the biaxial strain configuration. Typical spectra of monolayer WSe₂ and MoSe₂ are listed in panels (b) and (c), respectively. Inset are the regimes of negative triions. Panel (d) presents the circular polarization spectra of WSe₂ triions at 5.92 and 50.2 μW, with a calculated dependence of spin-polarization on the density ratio of power/charge.

3.3 Results and discussion

In our characterization, the piezoelectric actuator will deform and transfer controlled strain into the TMDs flake, when an external electric voltage applies. Note that, the strain by the actuator is not the only resource of strain, which is also contributed by the residual strain in the sample fabrication, the contraction of the actuator in the cooling down, and even the local dielectric inhomogeneity.[132] These contributions are static when measurement

conditions are fixed, thus packed in the offset. In the following discussion, we focus on the biaxial strain by the actuator.

Figure 3. 1(b) and (c) demonstrate the typical spectra of ML WSe₂ and MoSe₂. Samples are pumped by a 532 nm cw laser, 1 μW, 10K, and optical signals are collected by an objective lens, NA=0.7. The rightmost peak in the WSe₂ spectrum at 1.7270 eV is neutral exciton (X_w). Compared to reports on Si/SiO₂ substrate[133,134], there is an ~15 meV redshift, which we attribute to the PMN-PT deformation in the cooling down and gold surface induced dielectric environment shift. On the left is the trion fine structure at 1.6968 eV (T_s) and 1.6902 eV (T_t), whose splitting agrees with previous reports.[56,129,135] Their regimes are inset in the top left corner: the particles enclosed by the filled blue (unfilled red) ellipse comprise T_s (T_t). Other peaks corresponding to negatively charged exciton and phonon replicas are named after similar reports.[136,137] The spectrum of MoSe₂ is more straightforward, with neutral exciton (X_{Mo}) at 1.6244 eV and trion at 1.5954 eV.

In Figure 3. 1(d), we show the circular polarization behavior of T_t and T_s by a 633 nm cw laser, 15 K. The circular Dop is calculated by $(I_{co} - I_{cr}) / (I_{co} + I_{cr})$, where I is the integrated intensity accessed by the Lorentzian function.[30] Subscripts co and cr denote co- and cross-polarized signals, respectively. We see the Dop of T_s and T_t are far from 100%, which manifests the scattering process. Note that the Dop of T_t is higher than T_s, which can be interpreted by the power-induced asymmetry distribution of electrons.[138] The Dops of T_t and T_s can be written as $P(T_t) = \frac{P(X)-P(e)}{1-P(X)P(e)}$ and $P(T_s) = \frac{P(X)+P(e)}{1+P(X)P(e)}$, respectively. Here, $P(X)$ is the polarization of exciton between K and K' valleys, which is positive, because of optical selection rules. $P(e)$ is the polarization of electrons, which is negative since the excess electron is easier to go to the other valley.[138] These numerical relationships mentioned justify $P(T_t) > P(T_s)$, see Appendix.1 for specified interpretation.

Considering the PL results presented in previous reports, we estimate a charge density $n_e(MoSe_2) = 2.5 \times 10^{10} \text{cm}^{-2}$, [139] and $n_e(WSe_2) = 3 \times 10^{11} \text{cm}^{-2}$, [138] respectively. With the increase of excitation power, either Dop of T_t or T_s shows a rise, which agrees with the previous reports.[138][140] Given the result we got here and the report in the literature, we speculate that the density ratio of power/charge determines the optical performance, which is supported by a first-principle calculation, inset in the top right corner of Figure 3. 1(d). The spin Dop different from the degree of polarization we detect from the optical signals by a scattering process. We need to make it clear that it is a possible solution from a set of

parameters. It helps readers to understand the dependence on the density ratio of power/charge, and more importantly, associate this effect to the interaction of electron and excitons. It does not interfere with the strain-dependence discussed below.

We can get a similar result from the Feynman scattering regime.[141] Readers interested in the interaction of exciton and excess electrons can refer to the discussion of the power dependence in Figure 4. 4.

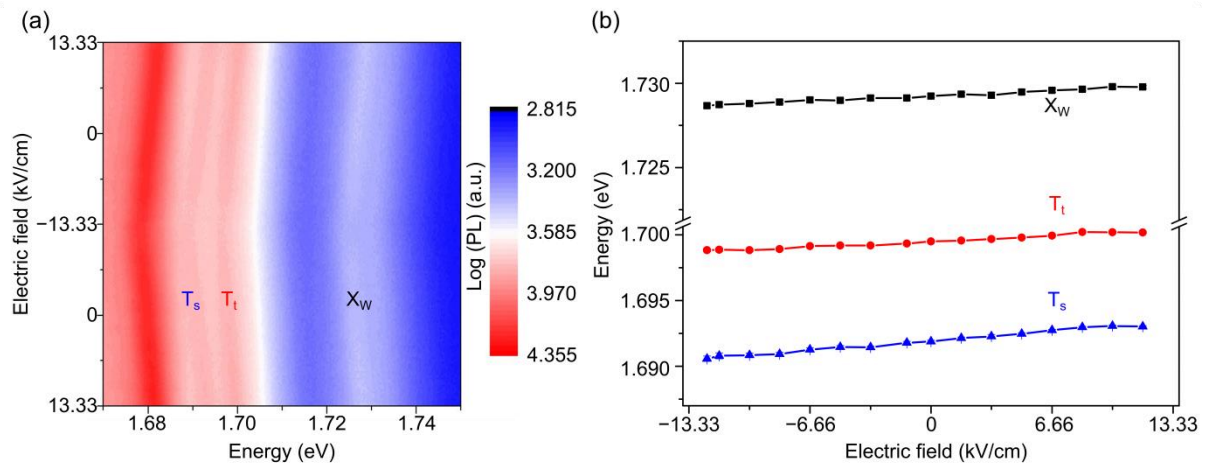


Figure 3. 2 a) Strain dependence of WSe₂ spectra. The vertical axis denotes the electric signal applied to the piezoelectric actuator, as shown in Fig 1(a). (b) extraction information of the neutral exciton (X_w), triplet negatively charged trion (T_t), and singlet charged trion (T_s). All the peak positions are accessed by the commonly used Lorentzian function, with tiny error bars.

We continue to discuss the influence of strain. Figure 3. 2(a) presents a color map of peak shift with active strain between 13.33 kV/cm and -13.33 kV/cm. The electric field in the vertical axis denotes the electric signal applied to the piezoelectric actuator, acting as the strain gauge. In Figure 3. 2(a), approximately reversible peak shifts of X_w, T_t, and T_s are traced: decreasing electric field induces a biaxial tensile strain, giving rise to the redshifts, which agrees with multiple strain-tuning research at room temperature and first-principle calculations.[57,142] To give the readers a clear view, all the peak positions in the upper half are extracted and plotted in Figure 3. 2(b). Meanwhile, we note the operation of the actuator is not ideally linear, which induces the non-linear responses around -13.33 kV/cm, the turning point is not very sharp, and at the end of the sweep, the peak positions do not go exactly to their initial positions. These unavoidable features are related to the hysteresis of piezoelectric materials. To get rid of this effect, we use the slope factors reported in the *ab initio* calculations[57] $a_{\text{MoSe}_2} = -98.2$ meV/% and $a_{\text{WSe}_2} = -133.5$ meV/% to transform the

strain gauge from the electric field into energies of neutral excitons. In Figure 3. 3, the strain state at 0 kV/cm is treated as the offset, which is comprised of the passive strain mentioned before and some active strain.

Readers might notice that the distance shift between T_s and T_t with the strain. In our experiment, we collect a series of data to investigate the strain's effect on the splitting. Till now, we do not find a convincing explanation. In the literature, the splitting between T_s and T_t is proportion to the e-h exchange interaction,[41,143,144] which is comprised of the interactions between excess electrons with bounded hole. Based on our current results, the previous reports[41] focusing on the short-range e-h exchange interaction is not perfectly strict.

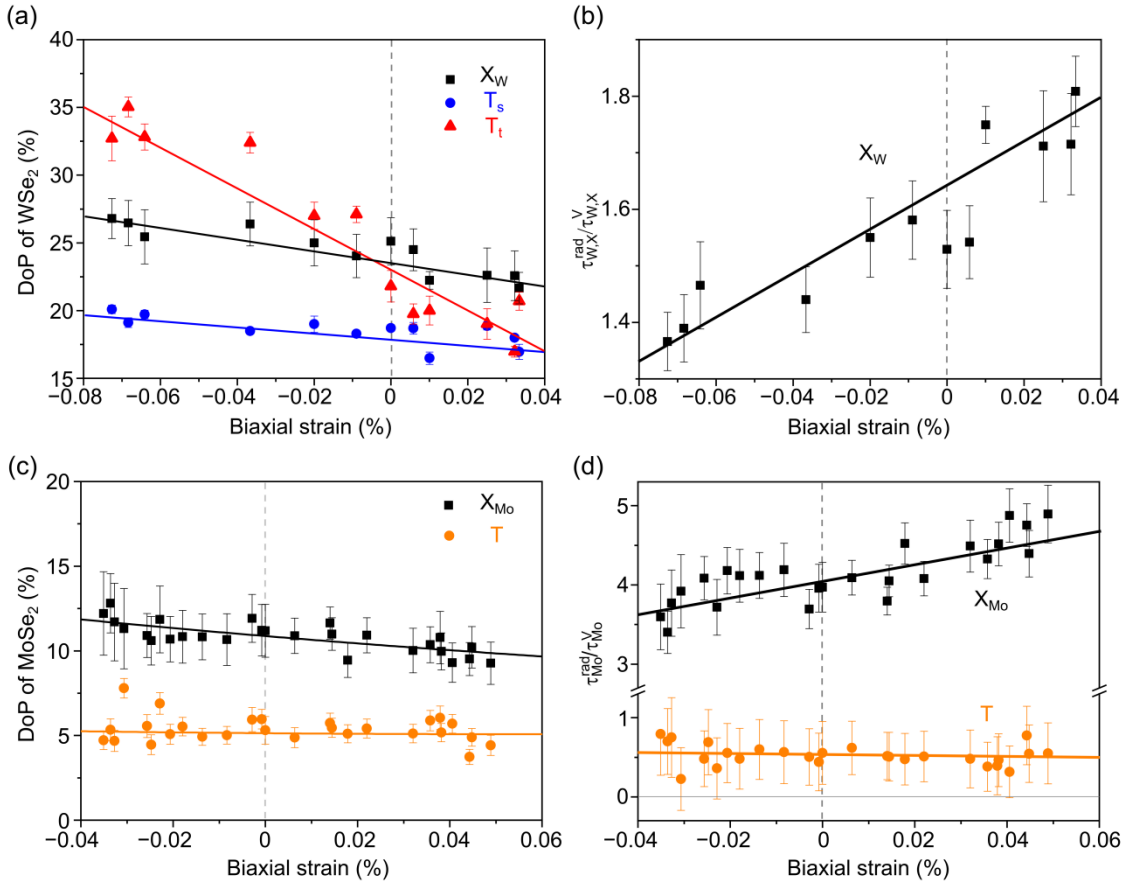


Figure 3. 3 (a) Strain dependence of X_w , T_t , and T_s . Based on the valley depolarization model in the main text, the ratio $\tau_{W,X}^{rad}/\tau_{W,X}^V$ are extracted in (b). Parallel results on MoSe₂ X_{Mo} and T are present in panels (c) and (d), respectively.

From the color map in Figure 3. 2(a), readers can see the shifts in intensities. The intensity of neutral exciton is associated with the evolution of conduction band edges.[47] The intensities of trions are more complicated, which act as a physical interface to detect the

trion scattering process. From now on, we start to discuss the Dop dependence on strain. From the previous reports, we know the excitation power,[138,140] temperature,[145] photon energy,[128] photon helicity,[128] traps from the substrate,[134,146] impurities[146] and external stimulus such as strain,[69,147,148] magnetic field[56] can affect the relaxation and dynamics after excitation. So here, the experimental condition is deliberately choosed. We employ a 1.96 eV left circular polarized photon to excite the sample ML WSe₂ and 1.68 eV photons for ML MoSe₂, respectively. And the excitation power is controlled at about 1 μ W to suppress the scattering between excited particles. The detection is on an impurities-free sample position, and the influence from the substrate is further ruled out. As such, the shift of observation can manifest the effect of the strain. In our optical setup, the accuracy of the circular polarization state is above 98%.

The scattering processes and related dynamics deterring the Dop of excitons and trions, vary with materials and radiations. We first discuss the excitons of MoSe₂ and WSe₂, as they share a similar behavior: Once pumped up in K valley, they can, during their lifetimes, transform into other radiations, by coupling with an extra electron, as well as scattering into the K' valley. In principle, the relaxation is determined by the radiations' lifetime (τ^{rad}) and angular momentum relaxation time.[149] Here, in our case, the latter corresponds to the hole spin lifetime or intervalley scattering time (τ^{V}). We adopt the valley depolarization model from Ref.[128] to describe the process:

$$\eta_{a,X} = \frac{\eta_{a,X,0}}{1 + 2 \tau_{a,X}^{\text{rad}} / \tau_{a,X}^{\text{V}}} \quad (3.1)$$

Here, the $\eta_{X,a,0}$ is the Dop of fresh exciton at the moment of generation, we assume it's 1. The subscript, a, denotes the excitons and materials system WSe₂ (W) or MoSe₂ (Mo). The superscript, V, denotes the intervalley scattering (V) and rad for radiative lifetime (rad).

Based on Eq.(3.1), we can further extract the $\tau_{Mo,X}^{\text{rad}} / \tau_{Mo,X}^{\text{V}}$ and $\tau_{W,X}^{\text{rad}} / \tau_{W,X}^{\text{V}}$, as shown in Figure 3. 3 (b) and (d). Both ratios of X_W and X_{Mo} present stable increases with our biaxial tensile strain. We note that the absolute values for X_{Mo} are larger than those of X_W, which is related to their short lifetime of X_{Mo}, associated with the Rashba mixing of bright and dark excitons.[130]

In principle, the lifetimes of excitons usually are determined by the materials system itself, generally scattering of the matrix, such as the scattering from the phonons.[126,143,150] In our case, the strain range is 0.1% at most, thus the corresponding influence on the phonon is

expected to be very weak. To quantify this effect, a first-principle calculation result is shown in Figure 3. 4(d): where, the lifetime of X_w shows a linear dependence: $\tau_{W,X}^{rad} = ks + b$. s is the strain, b is the intercept, 1.28 ps, and slope factor k is about 0.02 ps/%. So the $\tau_{W,X}^{rad}$ is stable to our strain. As a comparison, the dependence of scattering time is shown in Figure 4. 4(c), which presents a more prominent shift. Naturally, we attribute the variation of $\tau_{W,X}^{rad}/\tau_{W,X}^V$ to the shift of intervalley scattering process. For the neutral excitons, the intervalley scattering process is mainly driven by the e-h exchange interactions.[112] Here, we associate the effect of strain on this Coulomb interaction with the distance shifts between particles, which energetically corresponds to the peak shifts in Figure 3.2.

We proceed to discuss the Dop of trion (T) in MoSe₂. Compared with the trions in WSe₂, the composition of trions in MoSe₂ (Figure 3. 1(b) and (c)) is more straightforward. The solo peak of the trion and corresponding band structure rule out the effect of the intervalley scattering process, as shown in Figure 3. 4(b). A similar assumption and equation to Eq.(3.1) go as:

$$\eta_{Mo,T} = \frac{\eta_{Mo,X,0}}{1 + 2\tau_{Mo,T}^{rad}/\tau_{Mo,T}^V} \quad (3.2)$$

Here, the $\tau_{Mo,T}^{rad}$ and $\tau_{Mo,T}^V$ are the lifetime and intervalley scattering time of T. Note that in Eq. (3.2), we still use the initial Dop of the neutral exciton, because it's equal to that of the exciton, as the trion is comprised of the exciton and electron in the opposite valley.

The $\tau_{Mo,T}^{rad}/\tau_{Mo,T}^V$ are calculated and plotted in Figure 3. 3(d). We find the Dop of T in MoSe₂ is almost intact, which agrees with the forbidden radiation of intervalley scattering complexes (right side mechanism of Figure 3. 4(b)), in agreement with the spin protection.[151,152]

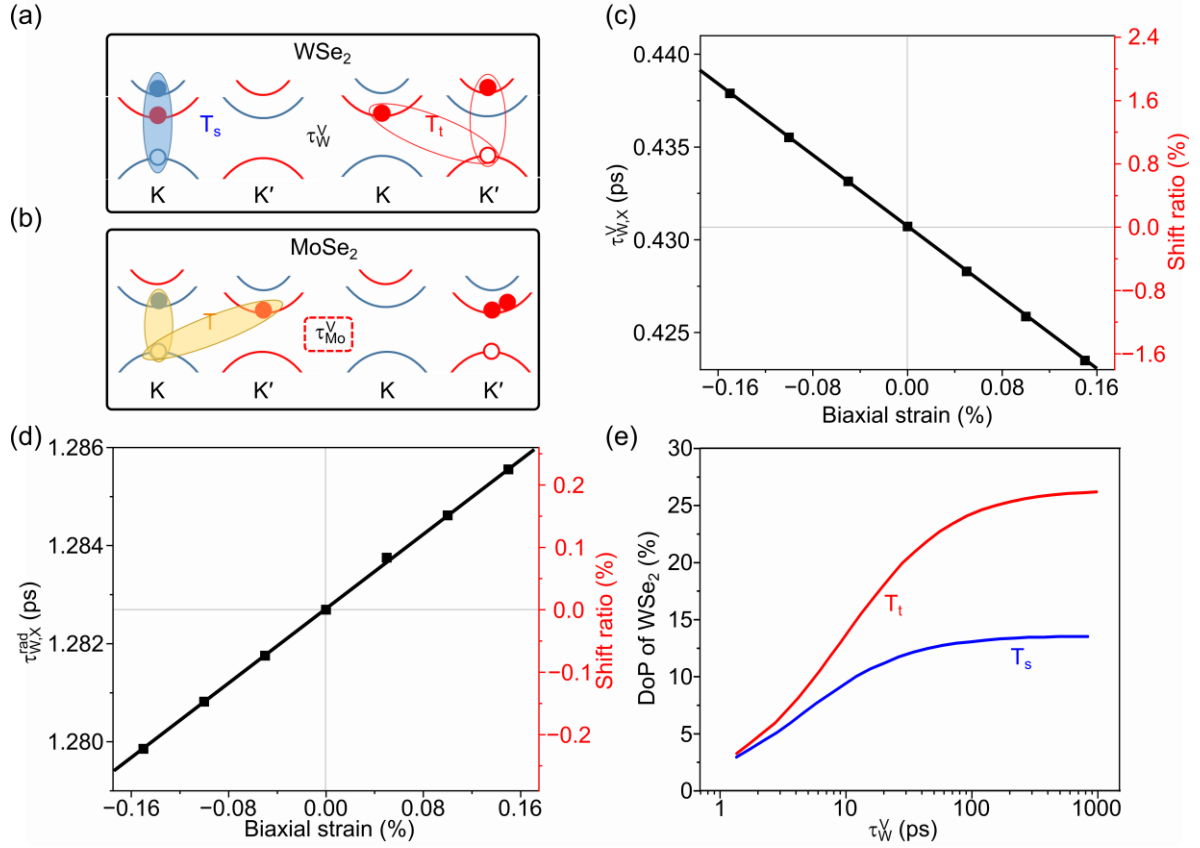


Figure 3. 4 (a, b) Regime of intervalley scattering in WSe₂ and MoSe₂, respectively. For MoSe₂, there are no corresponding peaks to the right side schematic. (c, d), A first-principle calculation results of the radiative intervalley scattering time constant and lifetime of X_W with strain. Details of the calculation are in Appendix.3.1 and 3.2. (e) A calculation of Dops of T_t and T_s with intervalley scattering rate. Readers interested in the details of panels (c) and (d) can refer to Appendix.3.1 and 3.3.

At last, we come to the description of trion in ML WSe₂ (T_t and T_s). From the process depicted in Figure 3. 4(a), T_s and T_t can convert into each other via the intervalley scattering, this is the reason why they are explained together. From the schematic, the scattering process consists of interactions between X_W, T_t, T_s, and excess electrons. The multiple scattering channels and sophisticated process render the solution of rate equation unsolved, so we turn to describe all relevant scatterings via this model:

$$\frac{dN_{W,X}^K}{dt} = \text{pump} - \frac{N_{W,X}^K}{\tau_{W,X}} - N_X^K \frac{N_{W,e}^K + N_{W,e}^{K'}}{\tau_W^b} - \frac{N_{W,X}^K - N_{W,X}^{K'}}{\tau_W^V} \quad (3.3)$$

$$\frac{dN_{W,Tt}^K}{dt} = -\frac{N_{W,Tt}^K}{\tau_{W,Tt}} + \frac{N_{W,X}^K N_{W,e}^K}{\tau_W^b} - \frac{N_{W,Tt}^K - N_{W,Ts}^{K'}}{\tau_W^V}$$

$$\frac{dN_{W,Ts}^K}{dt} = -\frac{N_{W,Ts}^K}{\tau_{W,Ts}} + \frac{N_{W,X}^K N_{W,e}^{K'}}{\tau_W^b} - \frac{N_{W,Ts}^K - N_{W,Tt}^{K'}}{\tau_W^v}$$

$$\frac{dN_{W,e}^K}{dt} = \frac{N_{W,Tt}^K}{\tau_{W,Tt}} + \frac{N_{W,Ts}^{K'}}{\tau_{W,Ts}} - N_e^K \frac{N_{W,X}^K + N_{W,X}^{K'}}{\tau_W^b}$$

Here, pump denotes the laser excitation process. The N denotes the density of particles, exciton, T_t , T_s , and electrons. The superscripts show the location of particles in K or K' valley. The parameter τ denotes the time constant for the particles. Especially, the τ_W^b denotes the formation time of trions, and τ_W^v is the intervalley scattering time. Readers should know this is the description of K valley, and the case for K' valley is the time-reversal.

In the first line of the model, an exciton is excited by the laser photons (first item), before the spontaneous recombination (second item), the exciton can couple with the electron and form T_s and T_t (third item), and can scatter into the K' valley (last item). Similarly, the density of T_t , T_s , and excess electron are listed in the second to the fourth line, respectively. We scrutinize the previous reports: The transformations of exciton are confirmed by the big dip of the absorption spectrum and weak intensity of the PL spectrum.[143] The intervalley scattering is momentum and spins conservative process, the annihilation-creation[127] and intervalley jumping regimes[126] have been suggested.

We integrate all related processes in the model and calculate the Dops of T_t and T_s as a function of trion intervalley scattering time τ_W^v . Figure 3. 4(e) shows a numerical solution for a set of fixed realistic parameters ($\tau_{W,X}=1$ ps, $\tau_{W,Tt}=2$ ps, $\tau_{W,Ts}=4$ ps, $\tau_W^v=0.5$ ps, and $\tau_W^b=0.1$ ps, which is the same set of parameters for the power dependence in Figure 3. 1(d)). We qualitatively associate the decrease of intervalley scattering time with the increase of strain, see Appendix.3.3. We note that if the intervalley scattering time, τ_W^v , decreases to 0, the Dops of singlet and triplet trions will go to zero, because here the intervalley scattering is free of energy consumption, which agrees with the basic assumption of optical selection rules. With the increase with τ_W^v , the Dops of T_t and T_s show an increase, which means the strain might affect the dynamics by extending the intervalley scattering time constant.

This model applies to the scattering process in ML MoSe₂, please refer to Appendix.2.

3.4 Conclusion and prospective

In this study, we record a strong impact of strain on the Dops of excitons and trions in ML WSe₂ and MoSe₂. The dependences of neutral excitons are similar, which are attributed to evolutions of e-h exchange interaction by strain. The evolutions and interpretations for trions are more complicated: trion from MoSe₂ is almost intact in the whole tuning range, which is related to the band structure suppressed intervalley scattering. The case for trion in WSe₂ is sophisticated and we describe this process by the rate equation model, which agrees with the previous reports and aforementioned assumptions well. In both material systems, biaxial strain can affect the Dop of radiations dynamically, which sheds light on the research of the scattering dynamics and can facilitate the development of devices.

4. Manipulation of WSe₂ exciton fine structure by anisotropic strain

The motivation of this chapter is to investigate the influence of anisotropic strain on the WSe₂ lattice. Similar to the biaxial or isotropic in-plane strain, the uniaxial or anisotropic strain can induce the peak shift of all radiative species. However, the influence of anisotropic strain on symmetry and the corresponding responses have not been reported at cryogenic temperatures. Some content of this chapter is prepared for the manuscript: Manipulation of WSe₂ exciton fine structure by anisotropic strain. Zhao An, Jonas Bauer, Mikhail Glazov, Alexey Chernikov, Pengji Li, Jingzhong Yang, Eddy P. Rugeramigabo, Michael Zopf, Kaiqiang Lin, and Fei Ding.

Semiconducting transition metal dichalcogenides, as a platform to investigate the valleytronics and corresponding applications, attract much attention. However, there is still more than one aspect requiring a deeper understanding, even on the most frequently reported monolayer WSe₂. Here, in cryogenic temperature, we integrate the dynamic strain-tuning technique with micro photoluminescence to investigate the fine structures of neutral exciton in monolayer WSe₂. We first identify the fine structures of exciton by the polarization-dependent spectrum and then record the nonlinear responses of exciton fine structure to anisotropic strain, which is interpreted by its interaction with exciton wavefunction. Our study draws a picture of the manipulation of wavefunctions, shedding light on a deeper understanding of WSe₂.

4.1 Introduction

Semiconducting transition metal dichalcogenides (TMDs) attract much attention these years.[22] Compared to their bulk counterparts, the monolayer TMDs flakes show contrasting properties, which triggers the expectation for the potential application in information storage.[112] Behind the optical performances, it's the optical selection rules, which are determined by the spin-orbit coupling and crystal symmetry[8]: in-plane C_3 symmetry, out-of-plane mirror symmetry, and the time-reversal symmetry between K and K' valley in reciprocal space.

The research on 2D TMDs are conducted by versatile methods[112]: magnetic field,[25,153] gate tuning,[17,30,129,139,154] and strain.[47,69,90] Strain tuning is a more powerful technique at the reduction dimensions, partially because of the enhanced mechanical properties.[155] The fundamental effect of strain is to affect the distances among particles and possibly the crystal symmetry, which can further induce numerous optical responses. In previous studies, it has been reported strain can tune exciton energy, linewidth,[44] scattering, and diffusions.[156] Local strain can collect the exciton nearby, which is called the funneling effect.[39,76,157] Compared to the in-plane isotropic strain, anisotropic strain can change the symmetry, possibly from C_3 to C_{2v} , even to C_1 .[91] Correspondingly, the optical performance, such as the helicity, will change. Yao Wang and coworkers[41] treat the effect of in-plane uniaxial strain (one representative type of anisotropic strain) as a horizontal magnetic field and predict the transformation of a unique Dirac point into the saddle shape. Mikhail Glazov and coworkers[109,158] reported the anisotropic strain can split the unique neutral exciton at a strain-free state into a closely split fine structure.

In this study, we report the fine structure of neutral exciton in WSe₂ and its strain dependence in cryogenic temperature. The fine structure is initially identified by the polarization-resolved PL. Interestingly, we find these split peaks can be controlled by our dynamical anisotropic strain: the splitting (phase) of them shows nonlinear evolutions, which is interpreted as the interaction of strain with the in-plane wavefunction. We conclude that anisotropic strain can tune the short-range e-h exchange interaction, which triggers evolutions of the exciton fine structure.

4.2 Sample and Experimental Setup

Figure 4. 1 (a) presents the sketch of our device. The monolayer WSe₂ layer is mechanically exfoliated from the bulk crystal before the encapsulation by hBN multiple-layer flakes. The whole process is conducted on the gold surface of the piezoelectric single crystal PMN-PT (<110> orientation, 300 μm thick, lead magnesium niobate-lead titanate). The top surface is polished, $R_a < 5$ nm. When voltage applies, the piezoelectric actuator will deform, and then transfer in-plane strain to WSe₂. To avoid possible doping effects, the top electrode is grounded. The optical image of the sample is shown in Figure 4. 1 (b), where the red dot denotes the laser spot, about 1.5 μm in diameter. In this research, we use a 633 nm linearly polarized continuous wave laser to excite the sample. A half-wave plate and a linear

polarizer are inserted in the signal collection arm to select the polarization-dependent signal. Additionally, a removable polarimeter is placed before the cryostat, to guarantee the precision of the polarization states.

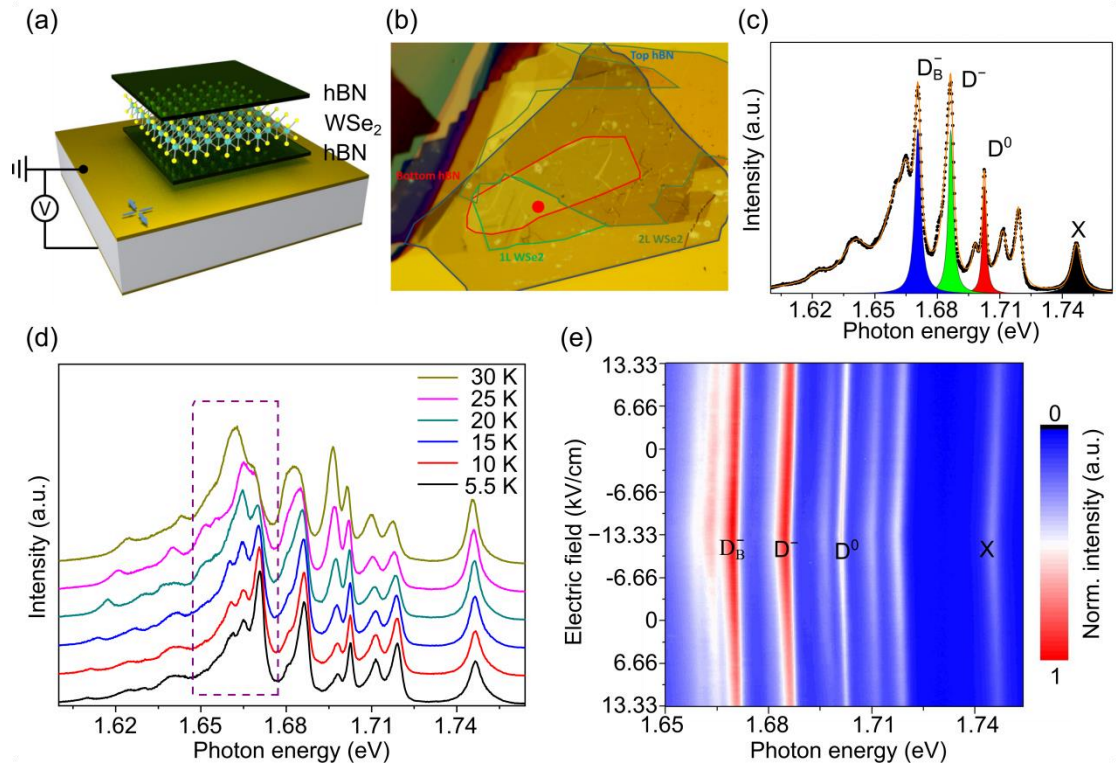


Figure 4. 1. Information of the sample. (a) Sketch of the sample. Monolayer WSe_2 encapsulated by multiple-layer hBN flakes is transferred on the bulk piezoelectric actuator, which acts as the source of strain at cryogenic temperatures. The blue arrows in the bottom left corner indicate the anisotropy of strain. (b) The optical image of the sample, where bottom hBN, top hBN, monolayer WSe_2 and bilayer WSe_2 zones are enclosed by curves with different colors. The red dot denotes the laser spot. (c) A typical spectrum at 5.5 K, excited by a 633 nm cw laser. For clarity, only concerned peaks are annotated. See the main text for all the peak information. (d) Temperature dependence of PL spectra. Peaks in the box begin to merge with the increased temperature. (e) Strain dependence of PL spectra. The electric field in the vertical axis is applied to the piezoelectric actuator, as shown in (a). Peak shifts are observable in the colormap. All intensities are normalized.

4.3 Results and discussion

A typical spectrum at 5.5 K is shown in Figure 4. 1(c), where the peak configuration agrees well with the previous reports[134,141]. The rightmost peak is the neutral exciton peak, X ($1.747 \text{ eV} \pm 5.37 \text{ meV}$). Other radiative species (binding energy to neutral exciton) are triplet negatively charged trion (T_t , 27.86 meV), singlet negatively charged trion (T_s , 35.43

meV), spin dark exciton (D^0 , 44.20 meV), negatively charged biexciton (XX^- , 48.7 meV), negatively charged dark exciton (D^- , 60.30eV), spin dark exciton coupled with Γ_5 phonon ($D_{\Gamma_5}^0$), negatively charged spin dark exciton brightened by the spin mixing (D_B^- , 76.13 meV), and some other phonon replica. To show a clear overview, only X, D^0 , D^- , and D_B^- are annotated in the panel. The physical relationships of D^0 , D^- and D_B^- , are further discussed in Figure 4. 2 with their strain dependence.

Temperature is a great influential factor in terms of the activity of the piezoelectric actuator, and optical features of WSe_2 . To determine suitable temperature parameters, a temperature dependence is conducted and shown in Figure 4. 1(d). Compared to the spectra at 5.5 K and 10 K, the peaks inside the box at 30 K are less characteristic. Therefore, the investigation on X and D^0 has the freedom to be conducted at 30 K, and the signal collection on D_B^- should be done at a lower temperature, actually 5.5 K. The performance of the piezoelectric actuator at 5.5 K is presented in Figure 4. 1(e), where all the radiative species show linear shifts with the electric field on the piezoelectric actuator. The activities of the actuator at different temperatures are compared in Figure 4. 2(a).

Figure 4. 2(a) presents the peak shift of X as a function of the electric field applied on the piezoelectric actuator. The major and minor panels demonstrate the responses at 5.5 K and 30 K, respectively. Here, X positions are accessed by Lorentzian fitting. We find that the tuning slope at 30 K ($201.33 \mu\text{eV}\cdot\text{cm}/\text{kV}$) is much larger than that at 5.5 K ($85.13 \mu\text{eV}\cdot\text{cm}/\text{kV}$). The activity of the piezoelectric actuator, together with the former discussion in the temperature-dependent optical features, supports our temperature selection: investigation on D_B^- is conducted at 5.5 K, and strain responses of X are conducted at 30 K.

Notably, the electric field in Figure 4. 2(a) cannot represent the real strain levels of the emitters. The reason lies in the presence of piezoelectric hysteresis, which is observed in the nonlinearity of the curls. Therefore, we use the exciton energy as the strain gauge in the following discussion.

Here, we need to make it clear that the strain in our research is not all able to be controlled. We divide the strain into arbitrary strain u_a , and strain manipulated by piezoelectric actuator u_{pa} . u_a derives from the fabrication process, contraction of the substrate during the cooling down, and inhomogeneity or local disorder of the sample. It differs from point to point, however, at one sample position and a stable temperature, u_a is a constant. We make a coarse estimation of arbitrary strain, by using a parallel sample on SiO_2/Si wafer. The strain

at 30 K is estimated from -0.17% to -0.20% , which means the sample is in a compressive state, in agreement with the previous report of the piezoelectric actuator.[103] On the other hand, the anisotropy of u_a cannot be accessed. u_{pa} is an anisotropic strain. Here, we stress that exciton energy represents the sum of u_a and u_{pa} , while the shift of it is only contributed by u_{pa} .

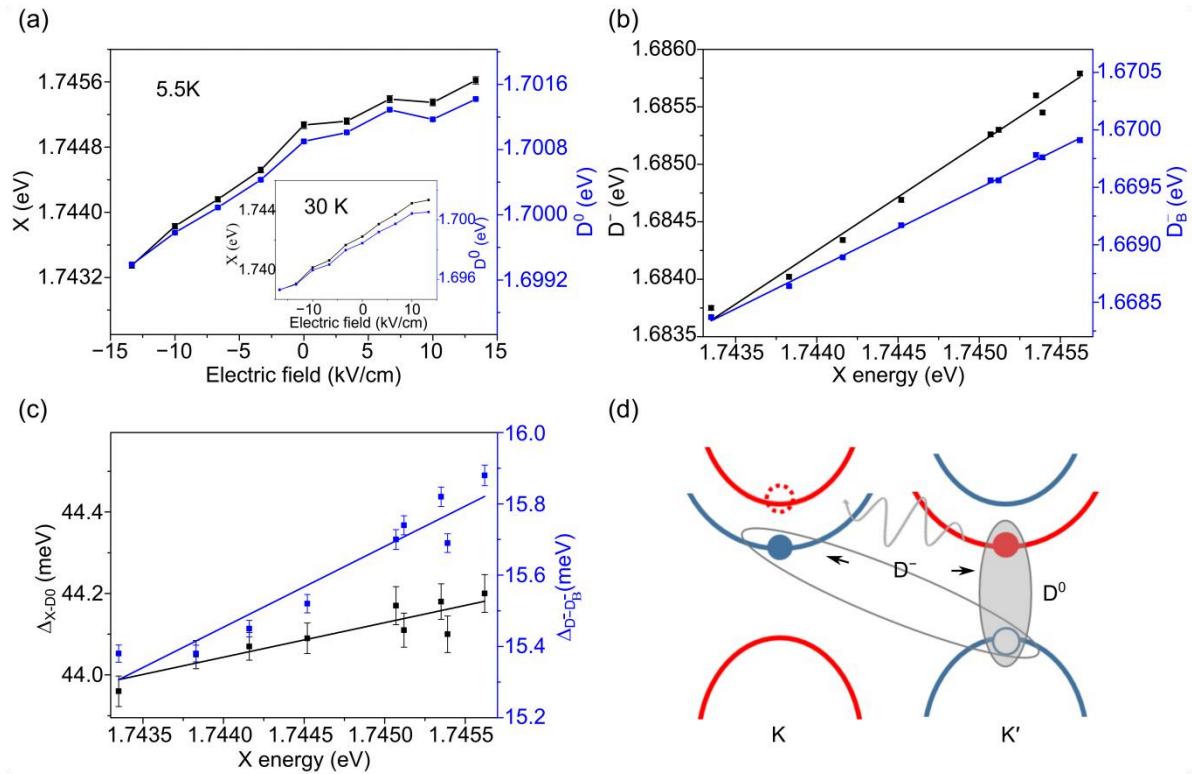


Figure 4. 2. Strain dependence of peaks. (a) and (b) demonstrate the peak shift of D , D^0 , D^- and D_B^- . The horizontal axis in (a) denotes the electric field applied to the piezoelectric actuator. (c) shows the shift of energy difference with strain. For a better comparison, all the ranges and steps in the same panel are unified, and starting points are aligned. (d) illustrates the radiative recombinations of D^0 , D^- , and D_B^- . In this schematic, the exciton is excited at K' valley, the case of K valley is the time reversal.

In Figure 4. 2(b), we extract the peak positions of D^- and D_B^- . Subsequently, we can get the energy difference between X and D^0 (Δ_{X-D^0}), as well as D^- and D_B^- ($\Delta_{D^- -D_B^-}$), as shown in Figure 4. 2(c). Here, we report the dynamic manipulation of Δ_{X-D^0} for the first time. By adopting a shifting slope of -6.4 meV per % uniaxial strain[156], the tuning range is about 0.14% uniaxial strain.

Meanwhile, we notice the energy difference Δ_{X-D^0} is above 44 meV, which disagrees with the previous *ab initio* calculation.[159] From the schematic of D^0 (bounded electron and

hole, enclosed by grey zone) in Figure 4. 2(d), Δ_{X-D0} is not only determined by the conduction band splitting (Δ_c), but also by the binding energies difference between X and $D^0(\Delta_{bd})$, that is,

$$\Delta_{X-D0} = \Delta_c + \Delta_{bd} \quad (4.1)$$

Interestingly, Δ_c can be accessed by the energy difference between D^- and D_B^- ($\Delta_{D^- - D_B^-}$): in the radiative process of D_B^- , the electron (solid blue sphere) and hole in different valleys combine and decay. To keep the momentum, the left-behind electron (solid red sphere) ends up in the opposite top valley via an intervalley scattering (grey curves, from the solid to dash open circle). This process counteracts the effect of the binding energy difference (Δ_{bd}) and finally presents the energy difference Δ_c . [141]

$$\Delta_c = \Delta_{D^- - D_B^-} \quad (4.2)$$

$$\Delta_{bd} = \Delta_{X-D0} - \Delta_{D^- - D_B^-} \quad (4.3)$$

In principle, Δ_{bd} is contributed by the effective mass and electron-hole exchange interaction. As the effective mass is not sensitive to the strain, [57] we can deduce the shift of the electron-hole exchange interaction with strain. This deduction is meaningful, as this short-range electron-hole exchange interaction contributes to the splitting of the neutral exciton, which we are discussing.

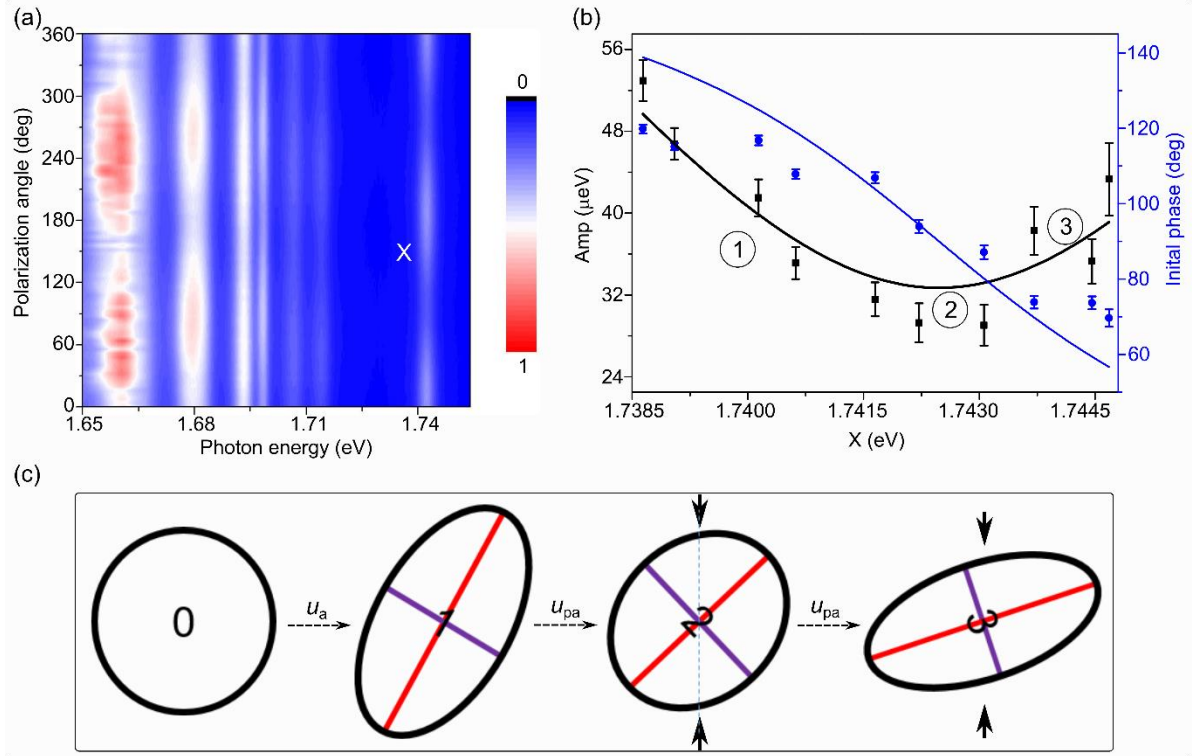


Figure 4. 3. (a) Polarization-dependent spectra at 30 K, where no electric field is applied to the actuator. The rightmost line in this panel denotes the variation of X. (b) Strain dependence of polarization behavior. The horizontal axis is the energy of neutral exciton, denoting the strain level. *Amp* denotes the splitting between two components of X. The initial phase indicates the phase relationship between the two components. See the main text for the extraction of them. (c) A schematic illustrating the interaction of anisotropic strain with the dipole of WSe₂. States 0, 1, 2, and 3 represent different fine structures, in terms of splittings and phases. Ellipse is analog to the dipole, shape, and orientation present the splitting and phase information. The red and purple lines inside are the major (a_i) and minor (b_j , $i, j=1, 2, \text{ and } 3$) of the ellipse, helping to show the shape deformation. The bisector of red and blue lines (blue dashed line) in state 2 is aligned with the direction of external strain. State 0 is the ideally strain-free state, and states 1, 2, and 3 correspond to the annotations in (b).

The splitting of the neutral exciton is identified in the polarization-dependent PL measurement. In Figure 4. 3(a), the intensity of neutral exciton (rightmost) at 30 K is not a constant, instead, it shows a periodical fluctuation. This observation indicates the presence of linear contributions in the signal. We interpret this observation as the effect of arbitrary strain(u_a), which drives the state from 0 to 1 in panel (c). State 0 denotes a strain-free state, where the C_3 symmetry is intact, and the corresponding wavefunction is drawn as a regular circle. By contrast, there is a symmetry reduction for state 1, which is associated with the presence of linear contributions. The major (red, a) and minor (purple, b) axes in state 1 are

not equal, $a_1 \neq b_1$. From states 0 and 1, readers can see the shifts in dipole shape and orientation, which is the demonstration of anisotropic strain's influence on symmetry. This ability is further verified by the interaction with active strain (u_{pa}).

The intensity shifts of the exciton are a straightforward display of polarization. Generally, the intensity is vulnerable, hence we focus on the **peak position** shift: at each strain level, the exciton energies show a sinusoidal variation in the polarization-dependent spectra:

$$X = Amp * \sin\left(\frac{x - \theta_p}{90}\right) + y_0 \quad (4.4)$$

Here, Amp is short for amplitude, which denotes variation of peak positions, corresponding to the splitting of two linear components. θ_p reads as the initial phase, illustrating the phase relationship between them. All the Amp and θ_p at different strain states are recorded and then plotted as a function of strain in Figure 4. 3(b). Interestingly, it shows a non-monotonic shift in Amp , we explain this observation by the interaction of the wavefunction of exciton with the anisotropic/pseudo-uniaxial strain.

When active anisotropic strain (u_{pa} , simplified as the black arrows in panel (c)) is applied to state 1, the ellipse shows a similar shift, in terms of orientation and shape: a clockwise rotation, together with shape deformation, $a_1/b_1 > a_2/b_2$. And the shift will be similar if the u_{pa} proceeds until it goes to state 2, where the angle bisector (the vertical dashed line) is along the strain. State 2 is the extreme state: a_2/b_2 is the minimum. After this, the strain will still rotate the wavefunction, whereas the shape of the ellipse will not go circularly, see state 3 ($a_3/b_3 > a_2/b_2$). The states 1, 2, and 3 are annotated in Figure 4. 3(b).

This process helps the reader to understand the evolution, quantitatively, it can be described by this model:

Generally, an in-plane strain can be written as

$$\begin{pmatrix} u_{xx} & u_{xy} \\ u_{xy} & u_{yy} \end{pmatrix} \quad (4.5)$$

when anisotropic strain applies, the exciton effective Hamiltonian, describing the radiative doublet of bright excitonic states on the basis of σ^+ and σ^- polarizations, can be expressed via the pseudospin Pauli matrices

$$H = \frac{\hbar B}{2} [\sigma_x(u_{xx} - u_{yy}) + 2\sigma_y u_{xy}] \quad (4.6)$$

Here, $u_{\alpha\beta}$ are the components of the strain tensor, and \mathcal{B} is a constant. An overall shift of the exciton doublet center is omitted. We introduce the parameters u_2 and θ , which describe the magnitude of anisotropic strain and its orientation in the (xoy) plane,

$$u_{xx} - u_{yy} = u_2 \cos 2\theta, 2u_{xy} = u_2 \sin 2\theta, u_2 = \sqrt{(u_{xx} - u_{yy})^2 + 4u_{xy}^2} \quad (4.7)$$

Diagnosing the Hamiltonian in Eq. (4.6) determines the splitting,

$$Amp = \mathcal{B} * u_2 \quad (4.8)$$

The angle θ describes the orientation of the polarization angle. Here, we get the splitting is proportional to the amplitude of anisotropic strain. The intercept, 0, in Eq.(4.8) denotes circular detection in absence of anisotropic strain, shown in state 0 Figure 4. 3 (c).

In our case, the strain is comprised of an arbitrary strain (u_a) and the strain by the piezoelectric actuator (u_{pa}). By coordinate system rotation,[38] u_{pa} can be written as:

$$u_{pa} = \begin{pmatrix} u_{xx}^p & 0 \\ 0 & u_{yy}^p \end{pmatrix} \quad (4.9)$$

and, we define anisotropy of strain by actuator u_p as:

$$u_p \equiv u_{xx}^p - u_{yy}^p \quad (4.10)$$

In this coordinate, the arbitrary strain (u_a) has a deflection angle ϕ , then

$$u_{xx}^a - u_{yy}^a = u_a \cos 2\phi, u_{xy}^a = u_{yx}^a = (u_a/2) \sin 2\phi \quad (4.11)$$

the corresponding *Amp* reads

$$Amp = \mathcal{B} \sqrt{u_p^2 + u_a^2 + 2u_p u_a \cos 2\phi} \quad (4.12)$$

polarization angle θ_p goes:

$$\theta_p = \theta_0 \pm \text{angle}[u_p + u_a \cos 2\phi, i(u_a \sin 2\phi)] \quad (4.13)$$

θ_0 is a constant, accounting for the setup-induced offset, and i is the imaginary sign. Eqs. (12, 13) present the *Amp* and initial phase in Figure 4. 3(b) are quantitatively related to the arbitrary strain u_a and strain by the actuator, in terms of magnitudes and orientations.

Additionally, in this research, the single crystal PMN-PT is $\langle 110 \rangle$ cut, which features:

$$u_{xx}^p - u_{yy}^p = k(u_{xx}^p + u_{yy}^p) \quad (4.14)$$

Generally, peak shift is proportional to the sum of them ($u_{xx}^p + u_{yy}^p$),[142] while the splitting of X is proportional to the difference between them ($u_{xx}^p - u_{yy}^p$).[109] Hence, Eqs. (4.12–4.14) establish the numerical relationship between the strain we apply and evolutions of *Amp* and phase we record. The lines in Figure 4. 3(b) represent the fitting results from this model. Around 1.743 eV, the strain state is along the angle bisector of the dipole, where the extrema (state 2) is achieved.

Notably, the model and observation will not guarantee that we can always get a process with the turning point in between. The observation is determined by the arbitrary strain-induced states. if the orientation of state 1 is not far from the uniaxial strain direction we can get an observation like panel (b). Otherwise, we cannot. In some scanning, we also get the monotonic shift, which corresponds to the processes of rotation before (downwards) or after (upwards) state 2.

In our case, the strain induced by the piezoelectric actuator is not large enough to counteract the arbitrary strain. At this emitter, we are not able to achieve the regular circle of the dipole, state 0. The strain magnitude is closely related to the possibility to see a turning point.

We also try to analyze the **peak intensity** of neutral exciton. Unfortunately, we did not find a reliable regular. In the colormap of Figure 4. 3 (a), the phase difference between X and D^0 always keeps a constant, about 90 deg. In the specified analysis, we find the variations of phases (I_X and I_{D^0}) are comparable to the phase difference of them, which dampens the credibility of this observation. Therefore, this section of results is not discussed here.

In the last section, a power dependence is added. The discussion is related to Figure 3. 1(d) in **Chapter 3**. In this sample here, the peaks are more characteristic, therefore we can verify our understanding of interactions between exciton and charges from another prospective, the competition between exciton (X) and dark exciton (D^0).

From a comparison of the PL spectrum here and the reflectance contrast spectrum[143], we can deduce the conversion of hot excitons into other radiative species. Those relaxation processes are discussed in Chapter 3, determining optical performances, such as valley coherence.

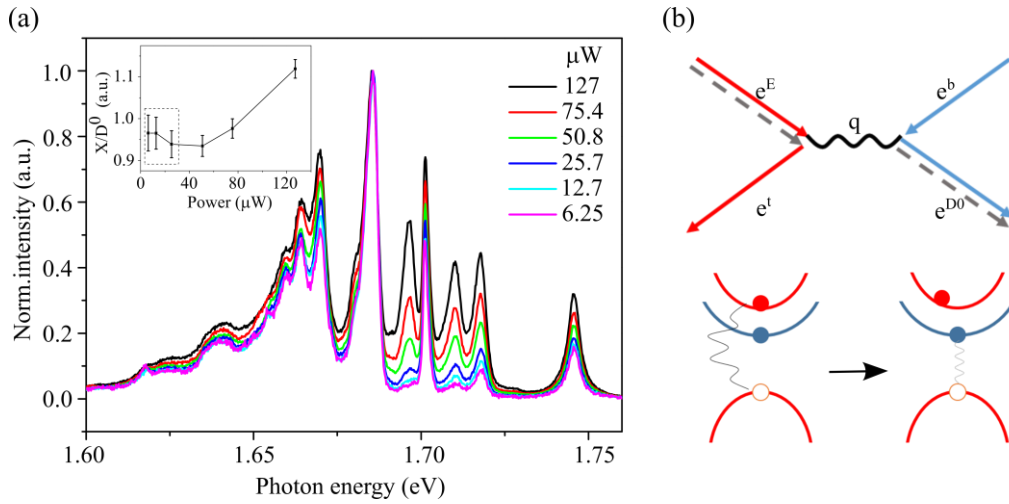


Figure 4. 4 (a) Power-dependent spectra. Inset is the intensity ratio of neutral exciton and spin dark exciton D^0 . (b) The upper panel is the Feynman diagram of the scattering process. Superscript denotes the state: E is bounded in exciton, D^0 is bounded in dark exciton, and b(t) is the bottom (top) bracket of the conduction band. The q means the momentum transfer. The bottom panel shows the corresponding initial (left) and final (right) states before/after the scattering.

In the low excitation phase, the many-body effect is less prominent. The single-particle picture can help to understand the process. As shown in Figure 4.4 (b), the hot exciton (top left, with E as the superscript, with solid line denoting electron dashed line hole) pumped up by the laser, can transform into a spin dark exciton (bottom right, with D^0 as the superscript). This process is very fast [160,161] in terms of thermodynamics, and energetically favorable. This process justifies the higher intensity of D^- and D^0 intensity at the lower power stage. We note some researchers [41,138] suggested other e-e scattering and e-exciton mechanisms for a transition from bright to dark excitons.

With the increase of power, other species show a relative increase in intensity than D^- , shown in panel (a), where all the intensities are normalized. This observation can be explained by the finite density of excess electrons. As illustrated in panel (b), the scattering process needs the assistance of the free electron (blue arrow, e^b). Due to the limitation of excess electrons, higher injection of hot excitons at increased power cannot sufficiently transform into D^0 . The suppressed scattering process contributes to the higher relative intensities of the neutral exciton, as shown in the inset panel of Figure 4.4 (a). In the extremely low power stage, the irregularities in the dashed box derive from the high signal-noise ratio.

4.4 Conclusion and prospective

To summarize, we apply dynamically controlled anisotropic strain to the monolayer WSe₂ at cryogenic temperature. We observe the fine structure of neutral exciton and record the evolution of their components with strain. The strain here is not high enough to completely remove the effect of arbitrary strain, which triggers to investigate higher-level strain tuning platforms as well as more versatile piezoelectric actuators.

5. Strain-induced modulation of quantum dot emissions at Si-vacancy transitions

The motivation of this chapter follows the former chapters, where monolithic anisotropic or isotropic single piezoelectric crystals are used. While the bulk devices show some limitations in terms of strain configuration and amplitude. Here, in this chapter, we discuss some micro-fabricated piezoelectric platforms and integrate a 2-leg MEMS strain tuning platform with QDs-embedded nanomembranes. The corresponding manuscript is in preparation, Strain-induced modulation of quantum dot emissions at Si-Vacancy transitions, Zhao An, Xin Cao, Jingzhong Yang, Maik Steinbach, Jürgen Koch, Peter Jäschke, Eddy P. Rugeramigabo, Fredrik Benthin, Rolf Haug, Michael Zopf, and Fei Ding.

A 6-leg platform with QDs is finished.

Qubit is the information unit in the envisioned quantum network. These years, multiple optical physical media have been developed, and photons from self-assembled quantum dots and negatively charged silicon-vacancy centers in diamonds are among the leading candidates. However, either of them is troubled by the incompatibility of the high brightness and long coherence time, which motivates us to investigate the hybridization of quantum dots and Silicon-vacancy. Here, we integrate a compact piezoelectric actuator with GaAs quantum dots embedded membrane, whose emission is around the zero phonon line of silicon-vacancy. In the cryogenic photoluminescence spectrum, we observe two different trions from the same quantum dot and find their binding energies show opposite evolutions with a strain. Our work deepens the understanding of quantum dots at zero phonon line of silicon-vacancy and facilitates the development of compact devices for the hybrid communication system.

5.1 Introduction

The pursuit of quantum communication networks spurs the development of quantum optics and related devices.[111] Quantum emitters, as one of the core devices inside, undergo great developments these years. On one hand, a series of solid-state emitters have emerged: self-assembled quantum dots[96] (QDs), negatively charged silicon-vacancy centers (SiV⁻)[162] and nitrogen-vacancy centers [163] in diamonds are among the most promising candidates. On the other hand, different optical structures[114,164] and post-growth tuning techniques

have been reported, such as strain[91,165], magnetic[166,167], and electric[168,169] field tuning. All of these make the emitter system more versatile and accelerate the realization of a practical system.[114,170,171]

While to date, no emitter is perfect for all the application scenarios. The emitters usually entail important compromises in their optical properties and quantum memory performances.[111] A prominent example is represented by GaAs QDs: they show an attractive combination of high brightness,[172–174] high indistinguishability,[175,176] high degree of entanglement,[174,177,178] and compatibility with optical structure and external fields.[91,165,168,169] However, QDs suffer from the phonon scattering from the host matrix, which reduces their coherence time greatly, usually on tens or hundreds of picoseconds for GaAs QDs polarization encoded qubits.[179] In contrast to QDs, SiV⁻ enjoys a much longer spin coherence time, up to 10 ms at 100 mK.[180] Recently, it has been reported that its coherence time can be further extended by strain.[181] While the modulation of their emission wavelength and the fabrication of optical structures are less flexible.[111] Considering the complementary features, the hybridization of QDs and SiV⁻ seems a more attractive option: the long coherence time of SiV⁻ photon manifests its potential in the quantum memory, and other components in the quantum communication system can rely on the QDs and related optical devices.

There are several stumbling blocks in this hybridization. The first refers to the optical performance of QDs, emitting around ZPL of SiV⁻ (QD@SiV⁻). Generally, the optical properties of GaAs QDs are influenced by their confinements[182]. QDs under different confinements are driven by different physics and exhibit different radiative species and wavelengths.[183] So far, there are not many reports on the optical performance of the QDs @ SiV⁻. A second aspect is pointed to the random growth nature of QDs, which makes it almost impossible to find different QDs with identical properties. This feature manifests the necessity of a deliberate post-growth tuning method. Fortunately, both issues can be tackled by the strain tuning technique.

These years, strain tuning technique for QDs has experienced considerable development.[91,106] Compared to the electric field,[184] strain can tune the wavelength without dampening the brightness. Interestingly, strain can eliminate the notorious fine structure splitting (FSS) by recovering the symmetry of QDs.[185,186]

Here, we integrate a QD-embedded membrane with a compact piezoelectric actuator. The structure of the piezoelectric actuator is deliberately defined so that it's able to apply position-resolved strain at cryogenic temperature. In the cryogenic PL spectrum, we observe two trions from a QD at SiV^- , their binding energies exhibit opposite responses to the same strain. In our device, photons from two QDs (A and B, Figure 1(a)) are tuned to resonance by the same electric field, which we attribute to the different configurations of the strain. The role of strain is further identified by evolutions of FSS and polarization phase, which agrees well with the model.

5.2 Sample fabrication

Figure 5. 1(a) shows the sketch of our device, consisting of a MEMS piezoelectric actuator and a piece of QDs-embedded membrane (gray plate). The optical structure (bottom left of Figure 5. 1(a)) is grown on a 50 nm AlAs sacrificial layer by molecular beam epitaxy.[96,183] Subsequently, a standard photolithography and a wet-chemical etching are successively applied, releasing the membranes with the size of $120 \times 160 \mu\text{m}^2$. After selection, a nano-membrane is transferred and held at the center of our piezoelectric actuator by a photoresist. The core part of actuator is an ‘H’ type structure PMN-PT ($[\text{Pb}(\text{Mg}_{1/3}\text{Nb}_{2/3})\text{O}_3]_{0.72}-[\text{PbTiO}_3]_{0.28}$), with two legs, each 1.5 mm long, 1.0 mm wide, separated by a 14.5 μm groove. The final state of the sample is inset in the bottom right of Figure 5. 1(a).

5.3 Results and discussion

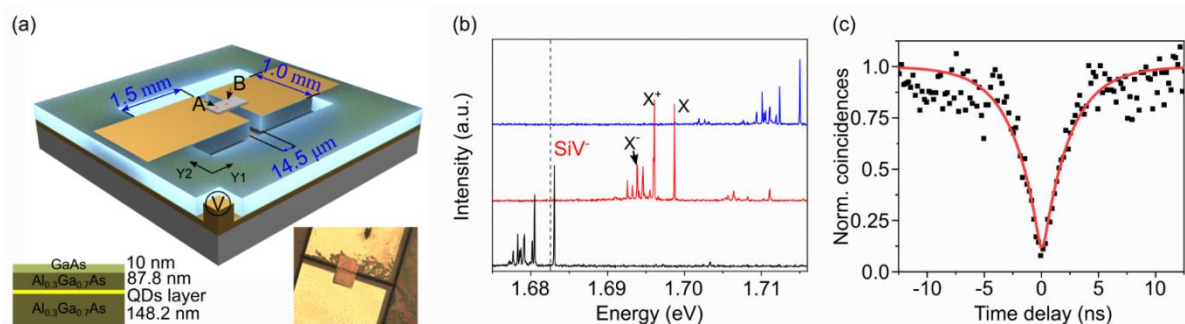


Figure 5. 1. (a) Schematic of position-resolved emitter system. Two exemplary QDs (A and B) are chosen from the membrane (light gray), either on top of or in the gap between the legs of the piezoelectric actuator. Y_1 and Y_2 denote the two directions along/orthogonal to the leg. The cross-section of the membrane is displayed (bottom left) together with an optical microscopy image of the top view (bottom right). (b) Exemplary photoluminescence spectra of different QDs at 6 K. The

transitions are around the ZPL of SiV^- (black, dashed line). (c) A second-order autocorrelation measurement for X photon. Red line are the fitting results, see main text for main information.

To characterize the emission properties, we collect the photoluminescence (PL) spectrum at 6 K, illuminated by a 532 nm cw laser. Figure 5. 1(b) presents a series of exemplary PL spectra, with peak clusters distributed in 723–727 nm, 730–734 nm, and 737–741 nm. Their primary peak configurations are similar, with a strong neutral exciton (X) peak on the rightmost and several derivative peaks on its left. The zero phonon line (ZPL) of SiV^- (dot line) is within the range of our emissions. We select one QD and identify three prominent transition peaks as X, positive trion X^+ and negative trion X^- (red spectrum in Figure. 5.1(b)). The verification of the transitions is detailed in the following section. To determine the single photon emission quality, second-order autocorrelation measurements are performed by sending the X photons to a Hanbury Brown and Twiss setup and the result is shown in Figure. 1(c). The anti-bunching coincidence histogram is modelled by the function

$$g^{(2)}(\tau) = \left[(g^{(2)}(0) - 1) e^{\frac{-|\tau|}{\tau_c}} + 1 \right] * N_{\text{det}}(\sigma), \quad (5.1)$$

where τ_c denotes the correlation time scale determined by the pumping and radiative decay process, $N_{\text{det}}(\sigma)$ is the instrument response function, mainly determined by the limited time resolution of the avalanche photodiode ($FWHM = 443.0$ ps). As shown in Figure 1(c), the sample exhibits a nice single photon emission feature, with $g_{\text{exp}}^{(2)}(0) = 0.07 \pm 0.3$ (black dot) and $g_{\text{fit}}^{(2)}(0) = 3.06 \times 10^{-9} \pm 0.03$ (red curve).

We continue to discuss the different trions in the spectrum. Temperature- and polarization-dependent measurements are successively implemented to determine the origin of the transitions. Temperature-dependent PL spectra of a randomly selected QD are stacked in Figure 5. 2(a), where all the emissions show redshifts with the increase of temperature. The integrated intensity reduction is further accessed by the Gaussian function and normalized in Figure 5. 2(b). The X^+ peak decreases faster than the others, which indicates a stronger scattering effect induced by temperature. Meanwhile, we collect the polarization dependence of PL spectra, by inserting a half wave-plate before a linear polarizer in the signal arm. We note that X shows a sinusoidal variation, which originates from the linear contribution of the signals in the presence of FSS. By contrast, the peak positions of X^+ and X^- keep constants, which agrees with a previous report of the trions, whose polarizations are influenced by the

extra charges.[187,188] Based on these observations and previous reports,[189] we argue X^+ is associated with a positive trions, and X^- comes from a negative trion, because the mobility of the hole is more sensitive to the temperature-induced scattering.

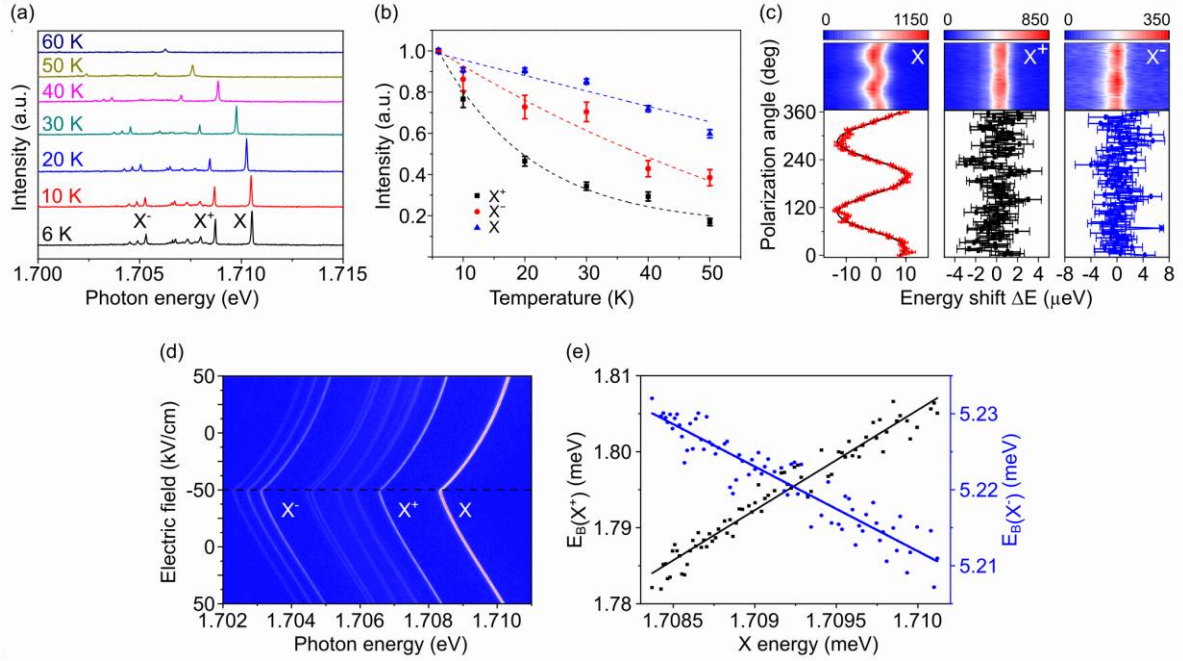


Figure 5. 2. (a) Temperature dependence of emissions from 6 K to 60 K. (b) Comparison of temperature-dependent integrated intensities of X^+ , X^- , and X , normalized by their intensities at 6 K. The dashed lines are exponential decays to guide the eyes. (c) Traces of all emissions energies as a function of polarization angle. The horizontal axis corresponds to the detuning of photons energies. (d) Strain dependence of emissions of QD, showing reversible tuning of spectral properties with the electric field. (e) Opposite binding energy evolutions of X^+ (black) and X^- (blue) to the same strain, black (blue) data points are linearly fitted as a function of the energy of neutral exciton.

We continue to discuss strain dependence of trions. Here, a source-meter (Keithley 2410 SMU) is used to drive the piezoelectric actuator. In this work, the top gates are grounded, in the case of electric doping to the nanomembrane. In Figure 5. 2(d), all the emissions show reversible shifts with the electric field applied to the actuator. We note there is a non-linear stage in the upper half, which is related to the hysteresis of the piezoelectric single crystal.[190] To get rid of this, we use the energy of X as the strain gauge in the following discussion.

In Figure 5. 2(e), we compare the strain dependence of X^- and X^+ to the same strain. We find their binding energies ($E_B(X^+)$ and $E_B(X^-)$) show linear but opposite shifts, which can be interpreted by the interaction of strain with their wave functions. According to empirical pseudo-potential calculation[191], the shift of binding energy can be written as:

$$\Delta E_B(X^+) \approx \Delta J_{eh} - \Delta J_{hh}, \quad (5.2)$$

$$\Delta E_B(X^-) \approx \Delta J_{eh} - \Delta J_{ee}, \quad (5.3)$$

where, J_{ee} , J_{hh} , and J_{eh} are Coulomb integrals between the lowest electron and highest hole states. The definition goes as[182]

$$J_{\mu\mu'} = \iint dRdR' \frac{[\Psi_\mu(R)]^* [\Psi_{\mu'}(R')]^* [\Psi_{\mu'}(R')] [\Psi_\mu(R)]}{\epsilon(R, R') |R - R'|} \quad (5.4)$$

R or R' is the Bohr radius of the electron or hole. μ and μ' are electrodes or holes, ϵ is the phenomenological microscopic dielectric functions.

From Eq. (5.4), Coulomb integrals are determined by the dispersion of the wave functions ($\Psi(R)$). In the presence of a compressive strain, the wave functions at the conduction (valence) band edge become more localized (delocalized, shift in R), resulting in $\Delta J_{hh} < 0 < \Delta J_{eh} < \Delta J_{ee}$. [191] Therefore, we can get $\Delta E_B(X^+) > 0$, and $\Delta E_B(X^-) < 0$ in Eqs. (5.2) and (5.3), which justifies the opposite slopes in Figure 5. 2(e).

In good consistency with this modeling, Gustavo A. N. and coworkers[182] report their calculations on the values of binding energies. In their configuration interaction model, they treat the strain as a perturbation, encoding its effect into the external potential in the Schrödinger equation. Their final results agree with our observations as well.

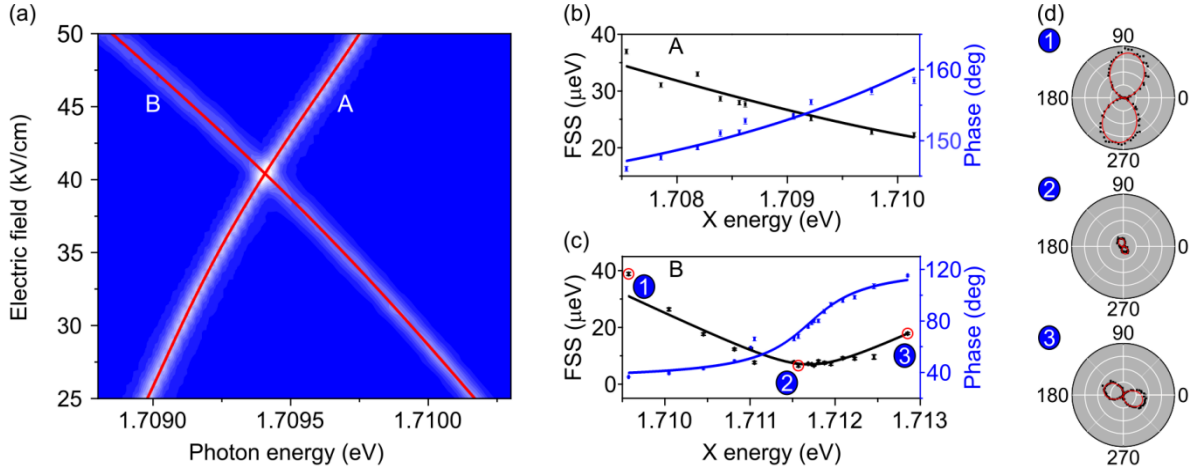


Figure 5. 3. Characterization of the optical response of QDs in the membrane to the different types of strain fields. (a) Comparison of the spectral feature of the neutral excitons at QDs A and B (see Figure 1(a)), as a function of the electric field applied to the piezoelectric actuator. (b) and (c) show the evolutions of FSS (black) and phase (blue) as a function of exciton energy. The distinction indicates the different strain configurations between the two QDs. (d) Polar plots of the polarization at the different strain conditions 1, 2, and 3 as denoted in (c). Orientation and amplitude represent phase and FSS, respectively. All plots have an axis scale of 45 μeV .

We continue to discuss the ability of this MEMS piezoelectric actuator by highlighting the resonance of the uncorrelated QDs in the same membrane. Figure 5.3(a) traces X emissions from QD A and B by applying a sequence of electric field values to the piezoelectric actuator. Two QDs A and B are selected: QD A is located in the nanomembrane glued to the leg of the piezoelectric actuator and QD B is in the portion of the nanomembrane on top of the gap between the legs, as shown in Figure 1(a). In contrast to QD A, the energy shift of QD B suggests that the dot experiences gradually either enhanced tension or released compression from 25 kV/cm to 50 kV/cm. With increasing electric field, the spectra of QD B exhibit a redshift with a magnitude that is almost twice the magnitude of the blueshift observed in QD A. The shift of QD A is similar to the observation in Figure 5.2(d), triggered by a compressive strain. On the contrary, the shift of QD B is apparently driven by a tensile strain, which originates from the contraction of the two legs. These performances can be understood in the following way: For QD A, the compressive strain along the orthogonal directions Y_1 and Y_2 can be expressed by

$$s_A^{Y1} = -k_1 \times E_p + f(s_B^{Y1}) \quad (5.5)$$

$$s_A^{Y2} = -k_1 \times E_p \quad (5.6)$$

where k_1 and E_p are the piezoelectric coefficient and electric field applied on the piezoelectric actuator, respectively. The negative signs denote compressive strains. Here, we use the same piezoelectric coefficient along two directions, because the PMN-PT single crystal is $\langle 100 \rangle$ cut. The last item denotes the difference in Y_1 and Y_2 direction, which is contributed by asymmetric boundary condition and influence of suspended section of membrane. The strain at QD B is quite different: under a positive electric field, it experiences the same tensile strain as QD A along the Y_2 direction with the same magnitude, but with a distinguished tensile strain along the Y_1 direction,

$$s_B^{Y1} = 2 \times \eta \times k_1 \times E_p, \quad (5.7)$$

$$s_B^{Y2} = -k_1 \times E_p \quad (5.8)$$

η is the strain transfer coefficient from the actuator to the membrane, approaching 1.

This configuration of strain field is further verified in terms of FSS and polarization angle of QDs A and B. In Figure 5.3(b), we observe that while FSS and polarization angle of QD A vary monotonically, there is a turning point in the FSS and a step-like evolution of the polarization angle for the QD B, in Figure 5.3(c). Generally, the isotropic strain cannot reshape or rotate the wave functions of QDs. The evolutions in Figures 3(b) and (c) argue the anisotropy of strain fields at QDs A and B, which agrees with the Eqs. (4) and (5). An anisotropic strain (uniaxial strain for example) applied to a QD can introduce a change in symmetry, affecting the FSS and the polarization angles of the X states. The corresponding Hamiltonian can be written as

$$H = H_{2v} + H_{c1} + sV_s(\mathbf{n}). \quad (5.9)$$

Here, H_{2v} and H_{c1} are the contributions from reduced C_{2v} and C_1 symmetries, respectively. s is the magnitude of strain, $sV_s(\mathbf{n})$ is the potential contributed by the external strain and \mathbf{n} denotes the direction dependence of strain.

$$H = \begin{pmatrix} \bar{E} + c + a_1 \times s & k + b \times s \\ k + b \times s & \bar{E} - c + a_2 \times s \end{pmatrix}, \quad (5.10)$$

where, $a_1 = \langle 1|V_s|1\rangle$, $a_2 = \langle 2|V_s|2\rangle$, $k = \langle 1|H_{c1}|2\rangle$, $b = \langle 1|V_s|2\rangle$, $\bar{E} + c = \langle 1|H_{2v} + V_{c1}|1\rangle$, $\bar{E} - c = \langle 2|H_{2v} + V_{c1}|2\rangle$, $|1\rangle$ $|2\rangle$ are wave functions of two bright excitons. To get the FSS, we determine the eigenvalues by diagnosing the Hamiltonian:

$$\text{FSS} = \sqrt{4(b \times s + k)^2 + (a \times s + 2c)^2}, \quad (5.11)$$

$a = a_1 - a_2$. The phase(θ_{\pm}) can be expressed as

$$\tan(\theta_{\pm} - \theta_0) = \frac{-2c - a \times s \mp \sqrt{4(b \times s + k)^2 + (a \times s + 2c)^2}}{2(b \times s + k)}. \quad (5.12)$$

Here, we introduce a constant θ_0 as the offset, to account for phase deviation.

Eqs (5.11, 5.12) associate strain s with the FSS and phase, quantitatively.

Because exciton energy is proportional to the strain

$$E_X = E_{X,0} + k_2 \times s, \quad (5.13)$$

$E_{X,0}$ is the X energy at a strain-free state and k_2 is the transforming matrix to associate a strain and its energy shift.

Interestingly, we find that FSS is always positive, with a minimum value. Experimentally, in Figure 5.3(c), the strain dependence of FSS at QD B presents a minimum value less than 10 μeV , at about 1.7118 eV. At the same strain level, a step-like evolution of polarization angle occurs. We note that such a turning point in the magnitude of FSS is not always present, depending on the strength and direction of strain, as suggested by the last item of Eq. (5.9). The strain dependence of QD A is an example, where the FSS and polarization angle both demonstrate monotonic shift with strain. Actually, readers can regard this process as a phase between state 1 and state 2 for QD B.

Below, we combine the results in Figure 5.3(c) and (d) to draw the whole picture of strain dependence. The three states in Figure 5.3(c) correspond to the three points in Figure 5.3(d). At state 1, the FSS is about 40 μeV , and polarization angle is 5 deg. While a compressive strain applies, the FSS decreases, which corresponds to the contraction of magnitude in panel (d). Meanwhile, polarization angle shows a gentle increase, see the anti-clockwise rotation in panel (d). The shifts magnitude of FSS and polarization angle agree with parabola and inverse tangent curves, suggested by the Eqs. (5.11) and (5.12). If the strain continues, the case is similar until it approaches state 2, where the shift of FSS is slow and FSS gets the minimum, while the polarization angle presents a rapid shift. The case at state 3 is similar to that at state 1, the same rotation direction but a higher magnitude of FSS. In this sample, the edges of nanomembranes are not perfectly aligned with the cleavage planes ($\{110\}$), so the minimum value of FSS does not go down to zero ($< 1\mu\text{eV}$).

5.4 Conclusion and prospective

To summarize, we performed cryogenic PL research on QDs at SiV^- , reporting that differently trions show opposite shifts in response to the same strain. Since the device can apply position-

dependent strain, in principle, we can always find two QDs and tune them into resonance, which is luring for a compact photonic circuit. Behind the optical performance is the interaction of strain with their wave functions.

In this study, we are not able to eliminate the FSS ($<1 \mu\text{eV}$), which results from the imperfect alignment of membrane edges with the cleavage planes ($\{110\}$). The strain performance should be increased if the photoresist holding the membrane is completely removed.

Besides the 2-leg device we discussed, a 6-leg strain tuning platform is integrated with the low-dimensional emitter system, as below.

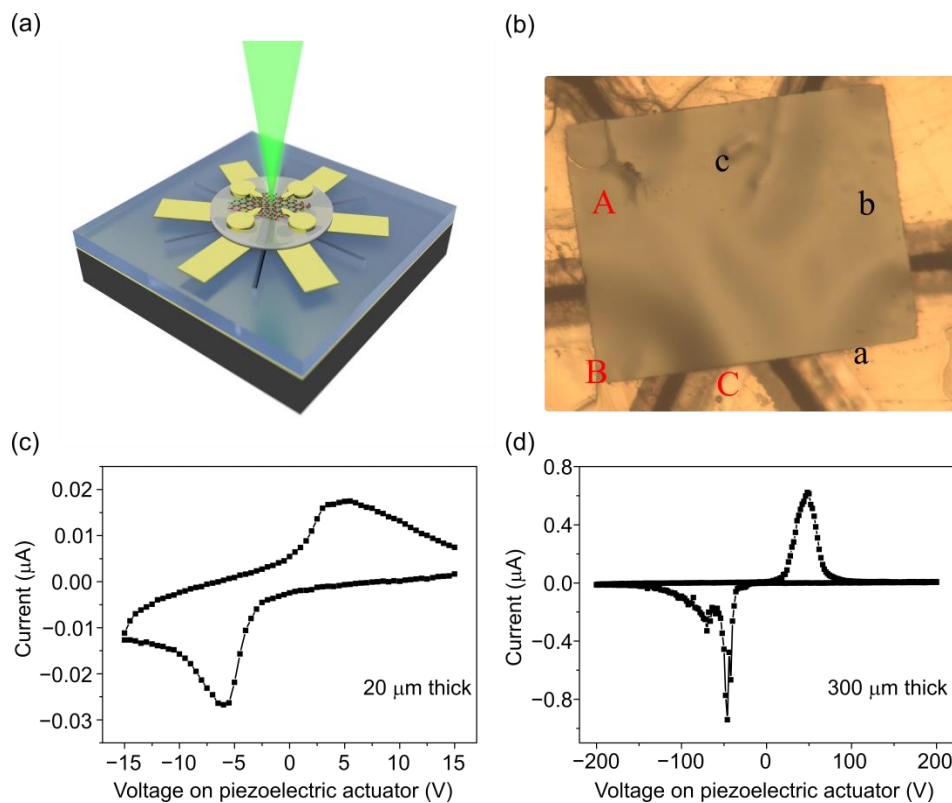


Figure 5. 4. (a) Schematic of six leg devices. (b) A prototype of the strain tuning platform. The Aa, Bb, and Cc are three pairs of legs. The membrane is $200 \times 250 \mu\text{m}^2$. (c) IV curves for the film ($20 \mu\text{m}$ thick) piezoelectric single crystal strain tuning device. (d) IV curves for bulk ($300 \mu\text{m}$ thick) piezoelectric single crystal strain tuning device. Panel (a) adapted from the SPP 2244 proposal. With permission from Fei Ding.

In Figure 5.4(a), the integrated 2D TMDs heterobilayer with a 6-leg platform is sketched. Compared to the 2-leg one, the 6-leg platform is more flexible: the 6-leg device can change the anisotropy of strain and orientation of strain. Ideally, we can put the membrane in between, without the concern about the alignment. The second aspect derives from the three

pairs of legs: two of them can be used to apply anisotropic strain, and the third pair can tune the wavelength. Considering the discussion in chapter 4, a 6-leg platform is envisioned to be able to achieve a regular circular of the wave function and meanwhile tune the photon energy around.

Even as the best piezoelectric material, PMN-PT still owns a quite limited d_{33} , on the order of magnitude of 2000 pC/N, which requires a very high voltage to induce observed shift. For bulk materials used the chapters 3 and 4, the coercive field is about 1.6 kV/cm or 48 V, Figure 5. 4(d). Here, a thin film piezoelectric is used, according to multiple IV curves measures, the voltage to achieve a coercive field is about 6 V, Figure 5. 4(c). which benefits the integrated devices for other measurements, such as ARPES and applications. Generally, the magnitude for signal modulation is not higher than 15V.

A comparable strain strategy is reported by Xiaodong Xu and coworkers[192,193]. Compared to their 2-leg device, our 2-leg platforms should be further developed for a higher strain magnitude. And the 6-leg one shows some advantages.

6. Appendix

1. Power dependence degree of Polarization T_t and T_s

We can now write the polarization of excitons (with N_X denoting the exciton density) as

$$0 < P(X) = \frac{N_X^K - N_X^{-K}}{N_X^K + N_X^{-K}} < 1 \quad (a.1)$$

According to the optical selection rules, $P(X)$ is positive.

Similarly, the $P(e)$ goes as

$$-1 < P(e) = \frac{N_e^K - N_e^{K'}}{N_e^K + N_e^{K'}} < 0 \quad (a.2)$$

Now we explain why $P(e)$ is negative. Some researchers[138] suggested the exciton polarization mechanism: when pumped up in K valley, hot excitons can affect the distribution of excess electrons, which results in the preference of excess electrons located in the K' valley. The reason behind this lies in the triplet trion is a phonon-aided process, while the singlet trion is a spin-flip process, which is less likely to happen than the phonon-aided process. In terms of lifetime, the triplet is shorter than the singlet,[194] which justifies this assumption.

According to the definition of Dop, the polarization of T_t writes as

$$P(T_t) = \frac{N_{co} - N_{cr}}{N_{co} + N_{cr}} \quad (a.3)$$

The composition of T_t in K valley, shown in Figure 3.1(b)

$$T_t^K \Leftrightarrow e^{K'} + X^K \quad (a.4)$$

$$P(T_t) = \frac{P(X) - P(e)}{1 - P(X)P(e)} \quad (a.5)$$

Similarly,

$$P(T_s) = \frac{P(X) + P(e)}{1 + P(X)P(e)} \quad (a.6)$$

From the equations, we can also deduce the dependence of Dop on the density of X and e.

$$P(T_t) - P(T_s) = \frac{2P(X)[1 - P(e)^2]}{[1 - P(X)P(e)][1 + P(X)P(e)]} \quad (a.7)$$

Eqs.(a.1, a.2, a.7) justify the $P(T_t) > P(T_s)$ in the Figure 3. 1(d).

2. Rate equation model for MoSe₂

Our rate equation model fits MoSe₂ as well. With similar notations and physical meanings, the model for MoSe₂ goes as

$$\begin{aligned} \frac{dN_{Mo,X}^K}{dt} &= pump - \frac{N_{Mo,X}^K}{\tau_{Mo,X}} - N_X^K \frac{N_{Mo,e}^{K'}}{\tau_{Mo}^b} - \frac{N_{Mo,X}^K - N_{Mo,X}^{K'}}{\tau_{Mo}^V} \\ \frac{dN_{Mo,T}^K}{dt} &= -\frac{N_{Mo,T}^K}{\tau_{Mo,T}} + \frac{N_{Mo,X}^K N_{Mo,e}^{K'}}{\tau_{Mo}^b} - \frac{N_{Mo,T}^K - N_{Mo,T}^{K'}}{\tau_{Mo}^V} \\ \frac{dN_{Mo,e}^K}{dt} &= \frac{N_{Mo,T}^{K'}}{\tau_{Mo,T}} - N_e^K \frac{N_{Mo,X}^{K'}}{\tau_{Mo}^b} \end{aligned} \quad (a.8)$$

Again, above is the case for K valley, the case for K' goes below

$$\begin{aligned} \frac{dN_{Mo,X}^{K'}}{dt} &= -\frac{N_{Mo,X}^{K'}}{\tau_{Mo,X}} - N_X^{K'} \frac{N_{Mo,e}^K}{\tau_{Mo}^b} - \frac{N_{Mo,X}^{K'} - N_{Mo,X}^K}{\tau_{Mo}^V} \\ \frac{dN_{Mo,T}^{K'}}{dt} &= -\frac{N_{Mo,T}^{K'}}{\tau_{Mo,T}} + \frac{N_{Mo,X}^{K'} N_{Mo,e}^K}{\tau_{Mo}^b} - \frac{N_{Mo,T}^{K'} - N_{Mo,T}^K}{\tau_{Mo}^V} \\ \frac{dN_{Mo,e}^{K'}}{dt} &= \frac{N_{Mo,T}^K}{\tau_{Mo,T}} - N_e^{K'} \frac{N_{Mo,X}^K}{\tau_{Mo}^b} \end{aligned} \quad (a.9)$$

3. Ab initio calculation and related time constant calculations

3.1 Basic information on density functional theory calculation

A density functional theory (DFT) calculation is performed to reveal the micro effect of strain on the low energy bands at K valley that constitute relevant excitons and trion observed experimentally.

The DFT calculations are performed using the WIEN2K code[195]. The crystal structure of the strained WSe₂ monolayer is generated using the Atomic simulation environment (ASE) python package.[196] We consider the PBEsol exchange-correlation function[197], a Monkhorst-pack k-grid of 15×15 and self-consistent convergence criteria of 10⁻² mRy/Bohr for the force, 10⁻⁶ e for the charge and 10⁻⁶ Ry for the energy.

For the heterostructures, the core-valence energy separation is chosen as -6 Ry, and the atomic radius is set to 9. For the inclusion of SOC, core electrons are considered fully relativistically whereas valence electrons are treated in a second variational step,[198] with the scalar-relativistic wave functions calculated in an energy window of -10 to 2 Ry. At zero strain, we found an equilibrium, in-plane lattice parameter of 3.2706 Å and a thickness of 3.3516 Å. We emphasize that for every strain value, the atomic structure is fully relaxed without SOC.[57]

3.2 Lifetime of the exciton

The calculated excitation lifetime uses the following formula: [199]

$$\tau_X^{rad} = \frac{\hbar \kappa_b \omega_{W,X}^2 m_0^2}{q e^2 |p_{cv}|^2 |\phi(0)|^2} \quad (a. 10)$$

where κ_b is the environmental high-frequency dielectric constant, here we use 5, corresponding to an hBN-encapsulated monolayer. $\omega_{W,X}$ is the exciton resonance frequency determined by the band gap and binding energy, p_{cv} is the interband momentum matrix element, $\phi(r)$ is the exciton wavefunction and $q = \sqrt{\kappa_b} \omega_0 / c$.

Using ab initio calculations of the band structure of monolayer with a strain and variable calculations[200] to strain. Our results are shown in Figure 3. 4(c).

3.3 Triplet-singlet valley scattering time

Triplet-singlet valley scattering time consists of a pair of electron-hole hopping from one valley to the other, conserving the total momentum and spin. As in the exciton case, several possible channels, such as trion-trion, trion electron-hole exchange, trion phonon, and trion-impurity interactions, can contribute to the intervalley triplet-singlet scattering of trions. The triplet to singlet scattering time can be estimated using the following formula:

$$\tau_T^{exc} = \frac{8\hbar(q\tau_T^{rad})^2}{M} \quad (a. 11)$$

where, $M = m_e + m_h$ is the effective mass of exciton. The quadratic dependence of the intervalley depolarization time on the radiative time indicates a significant sensitivity of the intervalley scattering of a trion singlet-triplet pair to external control.

7. Conclusion and outlook

Conclusion

Strain tuning applies to the low-dimensional emitter systems, however, it's much more challenging to apply strain at cryogenic temperatures. Compared to the multiple methods at room temperature, the strategy and tuning range at cryogenic temperature is limited.

In this thesis, we report several attempts to investigate responses of low dimensional emitter systems at cryogenic temperatures:

On the biaxial bulk piezoelectric actuator, hBN encapsulated monolayer WSe₂ is transferred. Once excited by the circularly polarized laser, the degree of circular polarizations of different radiations shows their corresponding strain dependences, which inspires the manipulation of valley depolarization/dephasing.

On the anisotropic bulk piezoelectric actuator, a similar sample is transferred. The narrow linewidth allows us a deep insight into the fine structures. The interaction between exciton wavefunction and anisotropic strain provides a new strategy to control the emitter system.

A drawback of cryogenic temperature strain tuning is its flexibility. Here, a designed MEMS platform is fabricated. From the results of a 2-leg strain tuning platform with QDs, the 2-leg device works well, it helps to unveil the opposite strain dependence of positive and negative trions. Importantly, this device applies to the integration with 2D TMDs flakes.

Outlook

The current work on the strain tuning platform is not satisfactory:

- 1, A higher-level strain tuning platform needs to be developed. With higher strain, the research will not be limited to qualitative investigations. In the meanwhile, another group achieve a higher level of strain via a commercial 2-leg device, which motivated the development of more mature devices.
- 2, A differentiated strain platform is required. These days, more and more interest is in the hetero-bilayer or homo-bilayer systems. Previous theoretical work describes a picture that the local atom landscape (twist angle and lattice constants) can be tuned by differentiated

strain. Some researchers envision the potential application of such a platform in signal processing and switching.

3, Strain tuning can be hybridized with some other optical technologies. In some roadmap for a lab-on-chip system, the integration with a gate tuning technology is envisioned. Due to the nice compatibility, multiple functional modules developed by the Si photonics technologies can migrate here, such as parametric nonlinear sources, electro-optic modulators, and cavities. All this progress helps the 2D TMDs or QDs emitters to walk a step further.

4, In Chapter 3, we explain the interaction of strain with neutral excitons in WSe₂, while the interaction of trion with strain is not fully understood.

Bibliography

1. Kumara, A., and Ahluwalia, P.K. (2012) Electronic structure of transition metal dichalcogenides monolayers 1H-MX₂ (M = Mo, W; X = S, Se, Te) from ab-initio theory: New direct band gap semiconductors. *Eur. Phys. J. B*, **85** (6), 18–22.
2. Voiry, D., Mohite, A., and Chhowalla, M. (2015) Phase engineering of transition metal dichalcogenides. *Chem. Soc. Rev.*, **44** (9), 2702–2712.
3. Duerloo, K.A.N., Li, Y., and Reed, E.J. (2014) Structural phase transitions in two-dimensional Mo-and W-dichalcogenide monolayers. *Nat. Commun.*, **5** (May), 1–9.
4. Durán Retamal, J.R., Periyangounder, D., Ke, J.J., Tsai, M.L., and He, J.H. (2018) Charge carrier injection and transport engineering in two-dimensional transition metal dichalcogenides. *Chem. Sci.*, **9** (40), 7727–7745.
5. Yu, H., and Yao, W. (2017) Valley-spin physics in 2D semiconducting transition metal dichalcogenides. *2D Mater. Prop. Devices*, 279–294.
6. Premasiri, K., and Gao, X.P.A. (2019) Tuning spin-orbit coupling in 2D materials for spintronics: A topical review. *J. Phys. Condens. Matter*, **31** (19).
7. Xie, S., Faeth, B.D., Tang, Y., Li, L., Parzyck, C.T., Chowdhury, D., Zhang, Y.H., Jozwiak, C., Bostwick, A., Rotenberg, E., Shan, J., Mak, K.F., and Shen, K.M. (2020) Direct observation of distinct minibands in moiré superlattices. *arXiv*, **2**, 1–18.
8. Yu, H., Liu, G. Bin, and Yao, W. (2018) Brightened spin-triplet interlayer excitons and optical selection rules in van der Waals heterobilayers. *2D Mater.*, **5** (3), 0–11.
9. Britnell, L., Ribeiro, R.M., Eckmann, A., Jalil, R., Belle, B.D., Mishchenko, A., Kim, Y.J., Gorbachev, R. V., Georgiou, T., Morozov, S. V., Grigorenko, A.N., Geim, A.K., Casiraghi, C., Neto, A.H.C., and Novoselov, K.S. (2013) Strong Light-Matter Interactions Thin Films. *Science (80-)*, **340** (June), 1311–1314.
10. Chiu, M.H., Zhang, C., Shiu, H.W., Chuu, C.P., Chen, C.H., Chang, C.Y.S., Chen, C.H., Chou, M.Y., Shih, C.K., and Li, L.J. (2015) Determination of band alignment in the single-layer MoS₂ WSe₂ heterojunction. *Nat. Commun.*, **6** (May), 1–6.
11. Seyler, K.L., Rivera, P., Yu, H., Wilson, N.P., Ray, E.L., Mandrus, D.G., Yan, J., Yao, W., and Xu, X. (2019) Signatures of moiré-trapped valley excitons in MoSe₂/WSe₂ heterobilayers. *Nature*, **567** (7746), 66–70.
12. Yu, J., Kuang, X., Zhong, J., Cao, L., Zeng, C., Ding, J., Cong, C., Wang, S., Dai, P., Yue, X., Liu, Z., and Liu, Y. (2020) Observation of double indirect interlayer exciton in WSe₂/WS₂ heterostructure. *Opt. Express*, **28** (9), 13260.
13. Mouri, S., Zhang, W., Kozawa, D., Miyauchi, Y., Eda, G., and Matsuda, K. (2017) Thermal dissociation of inter-layer excitons in MoS₂/MoSe₂ hetero-bilayers. *Nanoscale*, **9** (20), 6674–6679.

14. Unuchek, D., Ciarrocchi, A., Avsar, A., Watanabe, K., Taniguchi, T., and Kis, A. (2018) Room-temperature electrical control of exciton flux in a van der Waals heterostructure. *Nature*, **560** (7718), 340–344.
15. Hill, H.M., Rigosi, A.F., Rim, K.T., Flynn, G.W., and Heinz, T.F. (2016) Band Alignment in MoS₂/WS₂ Transition Metal Dichalcogenide Heterostructures Probed by Scanning Tunneling Microscopy and Spectroscopy. *Nano Lett.*, **16** (8), 4831–4837.
16. Ceballos, F., Bellus, M.Z., Chiu, H.Y., and Zhao, H. (2014) Ultrafast charge separation and indirect exciton formation in a MoS₂-MoSe₂ van der waals heterostructure. *ACS Nano*, **8** (12), 12717–12724.
17. Rivera, P., Seyler, K.L., Yu, H., Schaibley, J.R., Yan, J., Mandrus, D.G., Yao, W., and Xu, X. (2016) Supplementary Material for Valley-polarized exciton dynamics in a 2D semiconductor heterostructure. *Science* (80-.), **351** (688), 688.
18. Rivera, P., Yu, H., Seyler, K.L., Wilson, N.P., Yao, W., and Xu, X. (2018) Interlayer valley excitons in heterobilayers of transition metal dichalcogenides. *Nat. Nanotechnol.*, **13** (11), 1004–1015.
19. Chaves, A., Azadani, J.G., Alsalman, H., da Costa, D.R., Frisenda, R., Chaves, A.J., Song, S.H., Kim, Y.D., He, D., Zhou, J., Castellanos-Gomez, A., Peeters, F.M., Liu, Z., Hinkle, C.L., Oh, S.H., Ye, P.D., Koester, S.J., Lee, Y.H., Avouris, P., Wang, X., and Low, T. (2020) Bandgap engineering of two-dimensional semiconductor materials. *npj 2D Mater. Appl.*, **4** (1).
20. Yoshikawa, N., Nagai, K., Uchida, K., Takaguchi, Y., Sasaki, S., Miyata, Y., and Tanaka, K. (2019) Interband resonant high-harmonic generation by valley polarized electron–hole pairs. *Nat. Commun.*, **10** (1), 1–7.
21. Zhang, L., Zhang, Z., Wu, F., Wang, D., Gogna, R., Hou, S., Watanabe, K., Taniguchi, T., Kulkarni, K., Kuo, T., Forrest, S.R., and Deng, H. (2020) Twist-angle dependence of moiré excitons in WS₂/MoSe₂ heterobilayers. *Nat. Commun.*, **11** (1), 1–8.
22. Mak, K.F., and Shan, J. (2016) Photonics and optoelectronics of 2D semiconductor transition metal dichalcogenides. *Nat. Photonics*, **10** (4), 216–226.
23. Jones, A.M., Yu, H., Ghimire, N.J., Wu, S., Aivazian, G., Ross, J.S., Zhao, B., Yan, J., Mandrus, D.G., Xiao, D., Yao, W., and Xu, X. (2013) Optical generation of excitonic valley coherence in monolayer WSe₂. *Nat. Nanotechnol.*, **8** (9), 634–638.
24. Wang, G., Robert, C., Glazov, M.M., Cadiz, F., Courtade, E., Amand, T., Lagarde, D., Taniguchi, T., Watanabe, K., Urbaszek, B., and Marie, X. (2017) In-Plane Propagation of Light in Transition Metal Dichalcogenide Monolayers: Optical Selection Rules. *Phys. Rev. Lett.*, **119** (4), 1–7.

25. Stier, A. V., McCreary, K.M., Jonker, B.T., Kono, J., and Crooker, S.A. (2016) Exciton diamagnetic shifts and valley Zeeman effects in monolayer WS₂ and MoS₂ to 65 Tesla. *Nat. Commun.*, **7**, 1–8.
26. Mak, K.F., McGill, K.L., Park, J., and McEuen, P.L. (2014) Valleytronics. The valley Hall effect in MoS₂ transistors. *Sci. Suppl.*, **344** (6191), 1489–92.
27. Xu, X., Yao, W., Xiao, D., and Heinz, T.F. (2014) Spin and pseudospins in layered transition metal dichalcogenides. *Nat. Phys.*, **10** (5), 343–350.
28. Tran, K., Moody, G., Wu, F., Lu, X., Choi, J., Kim, K., Rai, A., Sanchez, D.A., Quan, J., Singh, A., Embley, J., Zepeda, A., Campbell, M., Autry, T., Taniguchi, T., Watanabe, K., Lu, N., Banerjee, S.K., Silverman, K.L., Kim, S., Tutuc, E., Yang, L., MacDonald, A.H., and Li, X. (2019) Evidence for moiré excitons in van der Waals heterostructures. *Nature*, **567** (7746), 71–75.
29. Yu, H., Liu, G. Bin, Tang, J., Xu, X., and Yao, W. (2017) Moiré excitons: From programmable quantum emitter arrays to spin-orbit coupled artificial lattices. *arXiv*, 1–8.
30. Rivera, P., Schaibley, J.R., Jones, A.M., Ross, J.S., Wu, S., Aivazian, G., Klement, P., Seyler, K., Clark, G., Ghimire, N.J., Yan, J., Mandrus, D.G., Yao, W., and Xu, X. (2015) Observation of long-lived interlayer excitons in monolayer MoSe₂-WSe₂ heterostructures. *Nat. Commun.*, **6**, 4–9.
31. Koperski, M., Nogajewski, K., Arora, A., Cherkez, V., Mallet, P., Veuillen, J.Y., Marcus, J., Kossacki, P., and Potemski, M. (2015) Single photon emitters in exfoliated WSe₂ structures. *Nat. Nanotechnol.*, **10** (6), 503–506.
32. Brotons-Gisbert, M., Baek, H., Campbell, A., Watanabe, K., Taniguchi, T., and Gerardot, B.D. (2021) Moiré-trapped interlayer trions in a charge-tunable WSe₂/MoSe₂ heterobilayer. 29–31.
33. Hong, J., Hu, Z., Probert, M., Li, K., Lv, D., Yang, X., Gu, L., Mao, N., Feng, Q., Xie, L., Zhang, J., Wu, D., Zhang, Z., Jin, C., Ji, W., Zhang, X., Yuan, J., and Zhang, Z. (2015) Exploring atomic defects in molybdenum disulphide monolayers. *Nat. Commun.*, **6**, 1–8.
34. Qiu, H., Xu, T., Wang, Z., Ren, W., Nan, H., Ni, Z., Chen, Q., Yuan, S., Miao, F., Song, F., Long, G., Shi, Y., Sun, L., Wang, J., and Wang, X. (2013) Hopping transport through defect-induced localized states in molybdenum disulphide. *Nat. Commun.*, **4**, 1–6.
35. Griffith, A.A. (1920) The phenomena of rapture and flow in solids. *Philos. Trans. R. Soc. London*, **221**.
36. Ding, F., Ji, H., Chen, Y., Herklotz, A., Dörr, K., Mei, Y., Rastelli, A., and Schmidt, O.G. (2010) Stretchable graphene: A close look at fundamental parameters through

- biaxial straining. *Nano Lett.*, **10** (9), 3453–3458.
37. Bi, Z., Yuan, N.F.Q., and Fu, L. (2019) Designing flat bands by strain. *Phys. Rev. B*, **100** (3), 1–9.
 38. Mennel, L., Furchi, M.M., Wachter, S., Paur, M., Polyushkin, D.K., and Mueller, T. (2018) Optical imaging of strain in two-dimensional crystals. *Nat. Commun.*, **9** (1).
 39. Branny, A., Kumar, S., Proux, R., and Gerardot, B.D. (2017) Deterministic strain-induced arrays of quantum emitters in a two-dimensional semiconductor. *Nat. Commun.*, **8** (May), 1–7.
 40. Zhai, D., and Yao, W. (2020) Layer Pseudospin Dynamics and Genuine Non-Abelian Berry Phase in Inhomogeneously Strained Moiré Pattern. *Phys. Rev. Lett.*, **125** (26), 266404.
 41. Yu, H., Liu, G. Bin, Gong, P., Xu, X., and Yao, W. (2014) Dirac cones and Dirac saddle points of bright excitons in monolayer transition metal dichalcogenides. *Nat. Commun.*, **5** (May), 1–7.
 42. Scalise, E., Houssa, M., Pourtois, G., Afanasev, V. V., and Stesmans, A. (2014) First-principles study of strained 2D MoS₂. *Phys. E Low-Dimensional Syst. Nanostructures*, **56** (1), 416–421.
 43. Johari, P., and Shenoy, V.B. (2012) Tuning the Electronic Properties of Semiconducting Transition Metal Dichalcogenides by Applying Mechanical Strains. (6), 5449–5456.
 44. Niehues, I., Schmidt, R., Drüppel, M., Marauhn, P., Christiansen, D., Selig, M., Berghäuser, G., Wigger, D., Schneider, R., Braasch, L., Koch, R., Castellanos-Gomez, A., Kuhn, T., Knorr, A., Malic, E., Rohlfing, M., Michaelis De Vasconcellos, S., and Bratschitsch, R. (2018) Strain Control of Exciton-Phonon Coupling in Atomically Thin Semiconductors. *Nano Lett.*, **18** (3), 1751–1757.
 45. Ghorbani-Asl, M., Borini, S., Kuc, A., and Heine, T. (2013) Strain-dependent modulation of conductivity in single-layer transition-metal dichalcogenides. *Phys. Rev. B - Condens. Matter Mater. Phys.*, **87** (23), 1–6.
 46. Yun, W.S., Han, S.W., Hong, S.C., Kim, I.G., and Lee, J.D. (2012) Thickness and strain effects on electronic structures of transition metal dichalcogenides: 2H-MX₂ semiconductors (M = Mo, W; X = S, Se, Te). *Phys. Rev. B - Condens. Matter Mater. Phys.*, **85** (3), 1–5.
 47. Desai, S.B., Seol, G., Kang, J.S., Fang, H., Battaglia, C., Kapadia, R., Ager, J.W., Guo, J., and Javey, A. (2014) Strain-induced indirect to direct bandgap transition in multilayer WSe₂. *Nano Lett.*, **14** (8), 4592–4597.
 48. Horzum, S., Sahin, H., Cahangirov, S., Cudazzo, P., Rubio, A., Serin, T., and Peeters, F.M. (2013) Phonon softening and direct to indirect band gap crossover in

- strained single-layer MoSe₂. *Phys. Rev. B - Condens. Matter Mater. Phys.*, **87** (12), 1–5.
49. Zhu, C.R., Wang, G., Liu, B.L., Marie, X., Qiao, X.F., Zhang, X., Wu, X.X., Fan, H., Tan, P.H., Amand, T., and Urbaszek, B. (2013) Strain tuning of optical emission energy and polarization in monolayer and bilayer MoS₂. *Phys. Rev. B - Condens. Matter Mater. Phys.*, **88** (12), 1–5.
 50. Yu, S., Xiong, H.D., Eshun, K., Yuan, H., and Li, Q. (2015) Phase transition, effective mass and carrier mobility of MoS₂ monolayer under tensile strain. *Appl. Surf. Sci.*, **325** (C), 27–32.
 51. Dong, L., Dongare, A.M., Namburu, R.R., O'Regan, T.P., and Dubey, M. (2014) Theoretical study on strain induced variations in electronic properties of 2 H -MoS₂ bilayer sheets. *Appl. Phys. Lett.*, **104** (5).
 52. Shi, H., Pan, H., Zhang, Y.W., and Yakobson, B.I. (2013) Quasiparticle band structures and optical properties of strained monolayer MoS₂ and WS₂. *Phys. Rev. B - Condens. Matter Mater. Phys.*, **87** (15), 1–8.
 53. Bhattacharyya, S., and Singh, A.K. (2012) Semiconductor-metal transition in semiconducting bilayer sheets of transition-metal dichalcogenides. *Phys. Rev. B - Condens. Matter Mater. Phys.*, **86** (7), 1–7.
 54. Pak, S., Lee, J., Lee, Y.W., Jang, A.R., Ahn, S., Ma, K.Y., Cho, Y., Hong, J., Lee, S., Jeong, H.Y., Im, H., Shin, H.S., Morris, S.M., Cha, S., Sohn, J.I., and Kim, J.M. (2017) Strain-Mediated Interlayer Coupling Effects on the Excitonic Behaviors in an Epitaxially Grown MoS₂/WS₂ van der Waals Heterobilayer. *Nano Lett.*, **17** (9), 5634–5640.
 55. Bai, Y., Zhou, L., Wang, J., Wu, W., McGilly, L.J., Halbertal, D., Fan, C., Lo, B., Liu, F., Ardelean, J., Rivera, P., Finney, N.R., Yang, X., Basov, D.N., Yao, W., Xu, X., Hone, J., Pasupathy, A.N., and Zhu, X. (2020) Excitons in strain-induced one-dimensional moiré potentials at transition metal dichalcogenide heterojunctions. *Nat. Mater.*, **19** (October).
 56. Aivazian, G., Gong, Z., Jones, A.M., Chu, R.L., Yan, J., Mandrus, D.G., Zhang, C., Cobden, D., Yao, W., and Xu, X. (2015) Magnetic control of valley pseudospin in monolayer WSe₂. *Nat. Phys.*, **11** (2), 148–152.
 57. Zollner, K., Junior, P.E.F., and Fabian, J. (2019) Strain-tunable orbital, spin-orbit, and optical properties of monolayer transition-metal dichalcogenides. *Phys. Rev. B*, **100** (19), 1–10.
 58. Liang, J., Zhang, J., Li, Z., Hong, H., Wang, J., Zhang, Z., Zhou, X., Qiao, R., Xu, J., Gao, P., Liu, Z., Liu, Z., Sun, Z., Meng, S., Liu, K., and Yu, D. (2017) Monitoring Local Strain Vector in Atomic-Layered MoSe₂ by Second-Harmonic Generation.

- Nano Lett.*, **17** (12), 7539–7543.
59. Mennel, L., Paur, M., and Mueller, T. (2019) Second harmonic generation in strained transition metal dichalcogenide monolayers: MoS₂, MoSe₂, WS₂, and WSe₂. *APL Photonics*, **4** (3).
 60. Conley, H.J., Wang, B., Ziegler, J.I., Haglund, R.F., Pantelides, S.T., and Bolotin, K.I. (2013) Bandgap engineering of strained monolayer and bilayer MoS₂. *Nano Lett.*, **13** (8), 3626–3630.
 61. Castellanos-Gomez, A., Poot, M., Steele, G.A., Van Der Zant, H.S.J., Agraït, N., and Rubio-Bollinger, G. (2012) Elastic properties of freely suspended MoS₂ nanosheets. *Adv. Mater.*, **24** (6), 772–775.
 62. Song, S., Keum, D.H., Cho, S., Perello, D., Kim, Y., and Lee, Y.H. (2016) Room Temperature Semiconductor-Metal Transition of MoTe₂ Thin Films Engineered by Strain. *Nano Lett.*, **16** (1), 188–193.
 63. Wang, R., Yu, Y., Zhou, S., Li, H., Wong, H., Luo, Z., Gan, L., and Zhai, T. (2018) Strategies on Phase Control in Transition Metal Dichalcogenides. *Adv. Funct. Mater.*, **28** (47), 1–17.
 64. Liu, K., Yan, Q., Chen, M., Fan, W., Sun, Y., Suh, J., Fu, D., Lee, S., Zhou, J., Tongay, S., Ji, J., Neaton, J.B., and Wu, J. (2014) Elastic properties of chemical-vapor-deposited monolayer MoS₂, WS₂, and their bilayer heterostructures. *Nano Lett.*, **14** (9), 5097–5103.
 65. Lee, J., Hu, X., Voevodin, A.A., Martini, A., and Berman, D. (2018) Effect of substrate support on dynamic graphene/metal electrical contacts. *Micromachines*, **9** (4), 1–9.
 66. Yang, R., Lee, J., Ghosh, S., Tang, H., Sankaran, R.M., Zorman, C.A., and Feng, P.X.L. (2017) Tuning Optical Signatures of Single- and Few-Layer MoS₂ by Blown-Bubble Bulge Straining up to Fracture. *Nano Lett.*, **17** (8), 4568–4575.
 67. Aslan, O.B., Datye, I.M., Mleczko, M.J., Sze Cheung, K., Krylyuk, S., Bruma, A., Kalish, I., Davydov, A. V., Pop, E., and Heinz, T.F. (2018) Probing the Optical Properties and Strain-Tuning of Ultrathin Mo_{1-x}W_xTe₂. *Nano Lett.*, **18** (4), 2485–2491.
 68. Shen, T., Penumatcha, A. V., and Appenzeller, J. (2016) Strain Engineering for Transition Metal Dichalcogenides Based Field Effect Transistors. *ACS Nano*, **10** (4), 4712–4718.
 69. He, K., Poole, C., Mak, K.F., and Shan, J. (2013) Experimental demonstration of continuous electronic structure tuning via strain in atomically thin MoS₂. *Nano Lett.*, **13** (6), 2931–2936.
 70. Pérez Garza, H.H., Kievit, E.W., Schneider, G.F., and Staufer, U. (2014) Controlled,

- reversible, and nondestructive generation of uniaxial extreme strains (>10%) in graphene. *Nano Lett.*, **14** (7), 4107–4113.
71. Li, Z., Lv, Y., Ren, L., Li, J., Kong, L., Zeng, Y., Tao, Q., Wu, R., Ma, H., Zhao, B., Wang, D., Dang, W., Chen, K., Liao, L., Duan, X., Duan, X., and Liu, Y. (2020) Efficient strain modulation of 2D materials via polymer encapsulation. *Nat. Commun.*, **11** (1), 1–8.
 72. Island, J.O., Kuc, A., Diependaal, E.H., Bratschitsch, R., Van Der Zant, H.S.J., Heine, T., and Castellanos-Gomez, A. (2016) Precise and reversible band gap tuning in single-layer MoSe₂ by uniaxial strain. *Nanoscale*, **8** (5), 2589–2593.
 73. Wang, Y., Cong, C., Yang, W., Shang, J., Peimyoo, N., Chen, Y., Kang, J., Wang, J., Huang, W., and Yu, T. (2015) Strain-induced direct–indirect bandgap transition and phonon modulation in monolayer WS₂. *Nano Res.*, **8** (8), 2562–2572.
 74. Sichert, J.A., Hemmerling, A., Cardenas-Daw, C., Urban, A.S., Feldmann, J., Yang, S., Wang, C., Sahin, H., Chen, H., Li, Y., Li, S.S., Suslu, A., Peeters, F.M., Liu, Q., Li, J., and Tongay, S. (2015) Tuning the optical, magnetic, and electrical properties of ReSe₂ by nanoscale strain engineering. *Nano Lett.*, **15** (3), 1660–1666.
 75. Lloyd, D., Liu, X., Christopher, J.W., Cantley, L., Wadehra, A., Kim, B.L., Goldberg, B.B., Swan, A.K., and Bunch, J.S. (2016) Band Gap Engineering with Ultralarge Biaxial Strains in Suspended Monolayer MoS₂. *Nano Lett.*, **16** (9), 5836–5841.
 76. Castellanos-Gomez, A., Roldán, R., Cappelluti, E., Buscema, M., Guinea, F., Van Der Zant, H.S.J., and Steele, G.A. (2013) Local strain engineering in atomically thin MoS₂. *Nano Lett.*, **13** (11), 5361–5366.
 77. Frisenda, R., Drüppel, M., Schmidt, R., Michaelis de Vasconcellos, S., Perez de Lara, D., Bratschitsch, R., Rohlfing, M., and Castellanos-Gomez, A. (2017) Biaxial strain tuning of the optical properties of single-layer transition metal dichalcogenides. *npj 2D Mater. Appl.*, **1** (1), 1–7.
 78. Plechinger, G., Castellanos-Gomez, A., Buscema, M., Van Der Zant, H.S.J., Steele, G.A., Kuc, A., Heine, T., Schüller, C., and Korn, T. (2015) Control of biaxial strain in single-layer molybdenite using local thermal expansion of the substrate. *2D Mater.*, **2** (1).
 79. Koenig, S.P., Boddeti, N.G., Dunn, M.L., and Bunch, J.S. (2011) Ultrastrong adhesion of graphene membranes. *Nat. Nanotechnol.*, **6** (9), 543–546.
 80. Tripathi, L.N., Iff, O., Betzold, S., Dusanowski, Ł., Emmerling, M., Moon, K., Lee, Y.J., Kwon, S.H., Höfling, S., and Schneider, C. (2018) Spontaneous Emission Enhancement in Strain-Induced WSe₂ Monolayer-Based Quantum Light Sources on Metallic Surfaces. *ACS Photonics*, **5** (5), 1919–1926.
 81. Palacios-Berraquero, C., Kara, D.M., Montblanch, A.R.P., Barbone, M., Latawiec, P.,

- Yoon, D., Ott, A.K., Loncar, M., Ferrari, A.C., and Atatüre, M. (2017) Large-scale quantum-emitter arrays in atomically thin semiconductors. *Nat. Commun.*, **8** (May), 1–6.
82. Miró, P., Ghorbani-Asl, M., and Heine, T. (2013) Spontaneous ripple formation in MoS₂ monolayers: Electronic structure and transport effects. *Adv. Mater.*, **25** (38), 5473–5475.
83. Castellanos-Gomez, A., Buscema, M., Molenaar, R., Singh, V., Janssen, L., Van Der Zant, H.S.J., and Steele, G.A. (2014) Deterministic transfer of two-dimensional materials by all-dry viscoelastic stamping. *2D Mater.*, **1** (1).
84. Nayak, A.P., Pandey, T., Voiry, D., Liu, J., Moran, S.T., Sharma, A., Tan, C., Chen, C.H., Li, L.J., Chhowalla, M., Lin, J.F., Singh, A.K., and Akinwande, D. (2015) Pressure-dependent optical and vibrational properties of monolayer molybdenum disulfide. *Nano Lett.*, **15** (1), 346–353.
85. Nayak, A.P., Yuan, Z., Cao, B., Liu, J., Wu, J., Moran, S.T., Li, T., Akinwande, D., Jin, C., and Lin, J.F. (2015) Pressure-Modulated Conductivity, Carrier Density, and Mobility of Multilayered Tungsten Disulfide. *ACS Nano*, **9** (9), 9117–9123.
86. Kim, J.-S., Moran, S.T., Nayak, A.P., Pedahzur, S., Ruiz, I., Ponce, G., Rodriguez, D., Henny, J., Liu, J., Lin, J.-F., and Akinwande, D. (2016) High pressure Raman study of layered Mo_{0.5}W_{0.5}S₂ ternary compound. *2D Mater.*, **3** (2), 025003.
87. Fu, X., Li, F., Lin, J.F., Gong, Y., Huang, X., Huang, Y., Han, B., Zhou, Q., and Cui, T. (2017) Pressure-Dependent Light Emission of Charged and Neutral Excitons in Monolayer MoSe₂. *J. Phys. Chem. Lett.*, **8** (15), 3556–3563.
88. Xia, J., Yan, J., Wang, Z., He, Y., Gong, Y., Chen, W., Sum, T.C., Liu, Z., Ajayan, P.M., and Shen, Z. (2021) Strong coupling and pressure engineering in WSe₂–MoSe₂ heterobilayers. *Nat. Phys.*, **17** (1), 92–98.
89. Li, F., Cabral, M.J., Xu, B., Cheng, Z., Dickey, E.C., Lebeau, J.M., Wang, J., Luo, J., Taylor, S., Hackenberger, W., Bellaiche, L., Xu, Z., Chen, L., ShROUT, T.R., and Zhang, S. (2019) No Title. **1** (April), 264–268.
90. Hui, Y.Y., Liu, X., Jie, W., Chan, N.Y., Hao, J., Hsu, Y.-T., Li, L.-J., Guo, W., and Lau, S.P. (2013) Exceptional tunability of band energy in a compressively strained trilayer MoS₂ sheet. *ACS Nano*, **7** (8), 7126–31.
91. Chen, Y., Zhang, J., Zopf, M., Jung, K., Zhang, Y., Keil, R., Ding, F., and Schmidt, O.G. (2016) Wavelength-tunable entangled photons from silicon-integrated III-V quantum dots. *Nat. Commun.*, **7**, 1–7.
92. Chakraborty, C., Mukherjee, A., Moon, H., Konthasinghe, K., Qiu, L., Hou, W., Peña, T., Watson, C., Wu, S.M., Englund, D., and Vamivakas, N. (2020) Strain tuning of the emission axis of quantum emitters in an atomically thin semiconductor. *Optica*, **7**

- (6), 580.
93. Hou, W., Azizimanesh, A., Sewaket, A., Peña, T., Watson, C., Liu, M., Askari, H., and Wu, S.M. (2019) Strain-based room-temperature non-volatile MoTe₂ ferroelectric phase change transistor. *Nat. Nanotechnol.*, **14** (July).
 94. Samanta, P.K. (2018) Strong and weak quantum confinement and size dependent optoelectronic properties of zinc oxide. *Ann. Univ. Craiova, Phys.*, **28**, 17–23.
 95. Gurioli, M., Wang, Z., Rastelli, A., Kuroda, T., and Sanguinetti, S. (2019) Droplet epitaxy of semiconductor nanostructures for quantum photonic devices. *Nat. Mater.*, **18** (8), 799–810.
 96. Keil, R., Zopf, M., Chen, Y., Höfer, B., Zhang, J., Ding, F., and Schmidt, O.G. (2017) Solid-state ensemble of highly entangled photon sources at rubidium atomic transitions. *Nat. Commun.*, **8** (May).
 97. Rastelli, A., Stufler, S., Schliwa, A., Songmuang, R., Manzano, C., Costantini, G., Kern, K., Zrenner, A., Bimberg, D., and Schmidt, O.G. (2004) Hierarchical self-assembly of GaAs/AlGaAs quantum dots. *Phys. Rev. Lett.*, **92** (16), 5–8.
 98. Plumhof, J.D., Trotta, R., Rastelli, A., and Schmidt, O.G. (2012) Experimental methods of post-growth tuning of the excitonic fine structure splitting in semiconductor quantum dots. *Nanoscale Res. Lett.*, **7**, 1–11.
 99. Lodahl, P., Mahmoodian, S., and Stobbe, S. (2015) Interfacing single photons and single quantum dots with photonic nanostructures. *Rev. Mod. Phys.*, **87** (2), 347–400.
 100. Winik, R., Cogan, D., Don, Y., Schwartz, I., Gantz, L., Schmidgall, E.R., Livneh, N., Rapaport, R., Buks, E., and Gershoni, D. (2017) On-demand source of maximally entangled photon pairs using the biexciton-exciton radiative cascade. *Phys. Rev. B*, **95** (23), 1–7.
 101. Boxberg, F., and Tulkki, J. (2007) Theory of the electronic structure and carrier dynamics of strain-induced (Ga, In)As quantum dots. *Reports Prog. Phys.*, **70** (8), 1425–1471.
 102. Huo, Y.H., Witek, B.J., Kumar, S., Cardenas, J.R., Zhang, J.X., Akopian, N., Singh, R., Zallo, E., Grifone, R., Kriegner, D., Trotta, R., Ding, F., Stangl, J., Zwiller, V., Bester, G., Rastelli, A., and Schmidt, O.G. (2013) A light-hole exciton in a quantum dot. *Nat. Phys.*, **10** (1), 46–51.
 103. Martín-Sánchez, J., Trotta, R., Piredda, G., Schimpf, C., Trevisi, G., Seravalli, L., Frigeri, P., Stroj, S., Lettner, T., Reindl, M., Wildmann, J.S., Edlinger, J., and Rastelli, A. (2016) Reversible Control of In-Plane Elastic Stress Tensor in Nanomembranes. *Adv. Opt. Mater.*, **4** (5), 682–687.
 104. Kumar, S., Trotta, R., Zallo, E., Plumhof, J.D., Atkinson, P., Rastelli, A., and Schmidt,

- O.G. (2011) Strain-induced tuning of the emission wavelength of high quality GaAs/AlGaAs quantum dots in the spectral range of the 87Rb D 2 lines. *Appl. Phys. Lett.*, **99** (16).
105. Huber, D., Reindl, M., Huo, Y., Huang, H., Wildmann, J.S., Schmidt, O.G., Rastelli, A., and Trotta, R. (2017) Highly indistinguishable and strongly entangled photons from symmetric GaAs quantum dots. *Nat. Commun.*, **8** (May), 1–7.
 106. Trotta, R., Martín-Sánchez, J., Wildmann, J.S., Piredda, G., Reindl, M., Schimpf, C., Zallo, E., Stroj, S., Edlinger, J., and Rastelli, A. (2016) Wavelength-tunable sources of entangled photons interfaced with atomic vapours. *Nat. Commun.*, **7**, 1–7.
 107. Vogel, M.M., Ulrich, S.M., Hafenbrak, R., Michler, P., Wang, L., Rastelli, A., and Schmidt, O.G. (2007) Influence of lateral electric fields on multiexcitonic transitions and fine structure of single quantum dots. *Appl. Phys. Lett.*, **91** (5), 2005–2008.
 108. Li, Z., Wang, T., Miao, S., Lian, Z., and Shi, S.F. (2020) Fine structures of valley-polarized excitonic states in monolayer transitional metal dichalcogenides. *Nanophotonics*, **9** (7), 1811–1829.
 109. Glazov, M.M., Dirnberger, F., Menon, V.M., Taniguchi, T., Watanabe, K., Bougeard, D., Ziegler, J.D., and Chernikov, A. (2022) Exciton fine structure splitting and linearly polarized emission in strained transition-metal dichalcogenide monolayers. *Phys. Rev. B*, **106** (12), 1–11.
 110. Yuan, X., Weyhausen-Brinkmann, F., Martín-Sánchez, J., Piredda, G., Křápek, V., Huo, Y., Huang, H., Schimpf, C., Schmidt, O.G., Edlinger, J., Bester, G., Trotta, R., and Rastelli, A. (2018) Uniaxial stress flips the natural quantization axis of a quantum dot for integrated quantum photonics. *Nat. Commun.*, **9** (1), 1–8.
 111. Atatüre, M., Englund, D., Vamivakas, N., Lee, S.Y., and Wrachtrup, J. (2018) Material platforms for spin-based photonic quantum technologies. *Nat. Rev. Mater.*, **3** (5), 38–51.
 112. Schaibley, J.R., Yu, H., Clark, G., Rivera, P., Ross, J.S., Seyler, K.L., Yao, W., and Xu, X. (2016) Valleytronics in 2D materials. *Nat. Rev. Mater.*, **1** (11).
 113. Koperski, M., Nogajewski, K., Arora, A., Cherkez, V., Mallet, P., Veuillen, J.Y., Marcus, J., Kossacki, P., and Potemski, M. (2015) Single photon emitters in exfoliated WSe₂ structures. *Nat. Nanotechnol.*, **10** (6), 503–506.
 114. Elshaari, A.W., Pernice, W., Srinivasan, K., Benson, O., and Zwiller, V. (2020) Hybrid integrated quantum photonic circuits. *Nat. Photonics*, **14** (5), 285–298.
 115. Chen, Y., Zhang, J., Zopf, M., Jung, K., Zhang, Y., Ding, F., and Schmidt, O.G. (2015) Energy-tunable entangled photon sources on a III-V/Silicon chip. 1–21.
 116. Li, F., Cabral, M.J., Xu, B., Cheng, Z., Dickey, E.C., LeBeau, J.M., Wang, J., Luo, J., Taylor, S., Hackenberger, W., Bellaiche, L., Xu, Z., Chen, L.-Q., Shroff, T.R., and

- Zhang, S. (2019) Giant piezoelectricity of Sm-doped $\text{Pb}(\text{Mg}_{1/3}\text{Nb}_{2/3})\text{O}_3\text{-PbTiO}_3$ single crystals. *Science* (80-.), **364** (6437), 264–268.
117. Sun, E., and Cao, W. (2014) Relaxor-based ferroelectric single crystals: Growth, domain engineering, characterization and applications. *Prog. Mater. Sci.*, **65**, 124–210.
 118. Peng, J., Luo, H., He, T., Xu, H., and Lin, D. (2005) Elastic, dielectric, and piezoelectric characterization of $0.70\text{Pb}(\text{Mg}_{1/3}\text{Nb}_{2/3})\text{O}_3\text{-}0.30\text{PbTiO}_3$ single crystals. *Mater. Lett.*, **59** (6), 640–643.
 119. Wang, F., Luo, L., Zhou, D., Zhao, X., and Luo, H. (2007) Complete set of elastic, dielectric, and piezoelectric constants of orthorhombic $0.71\text{Pb}(\text{Mg}_{1/3}\text{Nb}_{2/3})\text{O}_3\text{-}0.29\text{PbTiO}_3$ single crystal. *Appl. Phys. Lett.*, **90** (21).
 120. Liu, G., Jiang, W., Zhu, J., and Cao, W. (2011) Electromechanical properties and anisotropy of single- and multi-domain $0.72\text{Pb}(\text{Mg}_{1/3}\text{Nb}_{2/3})\text{O}_3\text{-}0.28\text{PbTiO}_3$ single crystals. *Appl. Phys. Lett.*, **99** (16), 1–4.
 121. Lv, P., and Lynch, C.S. (2017) Energetics of domain engineered rhombohedral ferroelectric single crystals. *Behav. Mech. Multifunct. Mater. Compos.* 2017, **10165** (April 2017), 101650B.
 122. Srivastava, A., Sidler, M., Allain, A. V., Lembke, D.S., Kis, A., and Imamoglu, A. (2015) Valley Zeeman effect in elementary optical excitations of monolayer WSe₂. *Nat. Phys.*, **11** (2), 141–147.
 123. Seyler, K.L., Schaibley, J.R., Gong, P., Rivera, P., Jones, A.M., Wu, S., Yan, J., Mandrus, D.G., Yao, W., and Xu, X. (2015) Electrical control of second-harmonic generation in a WSe₂ monolayer transistor. *Nat. Nanotechnol.*, **10** (5), 407–411.
 124. Wang, G., Bouet, L., Lagarde, D., Vidal, M., Balocchi, A., Amand, T., Marie, X., and Urbaszek, B. (2014) Valley dynamics probed through charged and neutral exciton emission in monolayer WSe₂. *Phys. Rev. B - Condens. Matter Mater. Phys.*, **90** (7), 1–6.
 125. You, Y., Zhang, X.X., Berkelbach, T.C., Hybertsen, M.S., Reichman, D.R., and Heinz, T.F. (2015) Observation of biexcitons in monolayer WSe₂. *Nat. Phys.*, **11** (6), 477–481.
 126. Lin, Z., Liu, Y., Wang, Z., Xu, S., Chen, S., Duan, W., and Monserrat, B. (2022) Phonon-Limited Valley Polarization in Transition-Metal Dichalcogenides. *Phys. Rev. Lett.*, **129** (2), 27401.
 127. Hao, K., Moody, G., Wu, F., Dass, C.K., Xu, L., Chen, C.H., Sun, L., Li, M.Y., Li, L.J., MacDonald, A.H., and Li, X. (2016) Direct measurement of exciton valley coherence in monolayer WSe₂. *Nat. Phys.*, **12** (7), 677–682.
 128. Mak, K.F., He, K., Shan, J., and Heinz, T.F. (2012) Control of valley polarization in

- monolayer MoS₂ by optical helicity. *Nat. Nanotechnol.*, **7** (8), 494–498.
129. Jones, A.M., Yu, H., Schaibley, J.R., Yan, J., Mandrus, D.G., Taniguchi, T., Watanabe, K., Dery, H., Yao, W., and Xu, X. (2016) Excitonic luminescence upconversion in a two-dimensional semiconductor. *Nat. Phys.*, **12** (4), 323–327.
 130. Yang, M., Robert, C., Lu, Z., Van Tuan, D., Smirnov, D., Marie, X., and Dery, H. (2020) Exciton valley depolarization in monolayer transition-metal dichalcogenides. *Phys. Rev. B*, **101** (11), 1–12.
 131. Soubelet, P., Klein, J., Wierzbowski, J., Silvioli, R., Sigger, F., Stier, A. V., Gallo, K., and Finley, J.J. (2021) Charged Exciton Kinetics in Monolayer MoSe₂ near Ferroelectric Domain Walls in Periodically Poled LiNbO₃. *Nano Lett.*, **21** (2), 959–966.
 132. Raja, A., Waldecker, L., Zipfel, J., Cho, Y., Brem, S., Ziegler, J.D., Kulig, M., Taniguchi, T., Watanabe, K., Malic, E., Heinz, T.F., Berkelbach, T.C., and Chernikov, A. (2019) Dielectric disorder in two-dimensional materials. *Nat. Nanotechnol.*, **14** (9), 832–837.
 133. Barbone, M., Montblanch, A.R.P., Kara, D.M., Palacios-Berraquero, C., Cadore, A.R., De Fazio, D., Pingault, B., Mostaani, E., Li, H., Chen, B., Watanabe, K., Taniguchi, T., Tongay, S., Wang, G., Ferrari, A.C., and Atatüre, M. (2018) Charge-tunable biexciton complexes in monolayer WSe₂. *Nat. Commun.*, **9** (1).
 134. He, M., Rivera, P., Van Tuan, D., Wilson, N.P., Yang, M., Taniguchi, T., Watanabe, K., Yan, J., Mandrus, D.G., Yu, H., Dery, H., Yao, W., and Xu, X. (2020) Valley phonons and exciton complexes in a monolayer semiconductor. *Nat. Commun.*, **11** (1), 1–7.
 135. Plechinger, G., Nagler, P., Arora, A., Schmidt, R., Chernikov, A., Del Águila, A.G., Christianen, P.C.M., Bratschitsch, R., Schüller, C., and Korn, T. (2016) Trion fine structure and coupled spin-valley dynamics in monolayer tungsten disulfide. *Nat. Commun.*, **7** (May), 1–9.
 136. Van Tuan, D., Scharf, B., Wang, Z., Shan, J., Mak, K.F., Žutić, I., and Dery, H. (2019) Probing many-body interactions in monolayer transition-metal dichalcogenides. *Phys. Rev. B*, **99** (8), 1–11.
 137. Paur, M., Molina-Mendoza, A.J., Bratschitsch, R., Watanabe, K., Taniguchi, T., and Mueller, T. (2019) Electroluminescence from multi-particle exciton complexes in transition metal dichalcogenide semiconductors. *Nat. Commun.*, **10** (1), 1–7.
 138. Robert, C., Park, S., Cadiz, F., Lombez, L., Ren, L., Tornatzky, H., Rowe, A., Paget, D., Sirotti, F., Yang, M., Van Tuan, D., Taniguchi, T., Urbaszek, B., Watanabe, K., Amand, T., Dery, H., and Marie, X. (2021) Spin/valley pumping of resident electrons in WSe₂ and WS₂ monolayers. *Nat. Commun.*, **12** (1), 1–7.

139. Ross, J.S., Wu, S., Yu, H., Ghimire, N.J., Jones, A.M., Aivazian, G., Yan, J., Mandrus, D.G., Xiao, D., Yao, W., and Xu, X. (2013) Electrical control of neutral and charged excitons in a monolayer semiconductor. *Nat. Commun.*, **4**, 1–6.
140. Vaclavkova, D., Wyzula, J., Nogajewski, K., Bartos, M., Slobodeniuk, A.O., Faugeras, C., Potemski, M., and Molas, M.R. (2018) Singlet and triplet trions in WS₂ monolayer encapsulated in hexagonal boron nitride. *Nanotechnology*, **29** (32).
141. Yang, M., Ren, L., Robert, C., Van Tuan, D., Lombez, L., Urbaszek, B., Marie, X., and Dery, H. (2022) Relaxation and darkening of excitonic complexes in electrostatically doped monolayer Formula Presented: Roles of exciton-electron and trion-electron interactions. *Phys. Rev. B*, **105** (8), 85302.
142. Johari, P., and Shenoy, V.B. (2012) Tuning the electronic properties of semiconducting transition metal dichalcogenides by applying mechanical strains. *ACS Nano*, **6** (6), 5449–5456.
143. Zipfel, J., Wagner, K., Ziegler, J.D., Taniguchi, T., Watanabe, K., Semina, M.A., and Chernikov, A. (2020) Light-matter coupling and non-equilibrium dynamics of exchange-split trions in monolayer WS₂. *J. Chem. Phys.*, **153** (3).
144. Courtade, E., Semina, M., Manca, M., Glazov, M.M., Robert, C., Cadiz, F., Wang, G., Taniguchi, T., Watanabe, K., Pierre, M., Escoffier, W., Ivchenko, E.L., Renucci, P., Marie, X., Amand, T., and Urbaszek, B. (2017) Charged excitons in monolayer WSe₂: Experiment and theory. *Phys. Rev. B*, **96** (8), 1–12.
145. Huang, J., Hoang, T.B., and Mikkelsen, M.H. (2016) Probing the origin of excitonic states in monolayer WSe₂. *Sci. Rep.*, **6** (March), 1–7.
146. Cao, T., Wang, G., Han, W., Ye, H., Zhu, C., Shi, J., Niu, Q., Tan, P., Wang, E., Liu, B., and Feng, J. (2012) Valley-selective circular dichroism of monolayer molybdenum disulphide. *Nat. Commun.*, **3** (May).
147. Carr, S., Fang, S., Jarillo-Herrero, P., and Kaxiras, E. (2018) Pressure dependence of the magic twist angle in graphene superlattices. *Phys. Rev. B*, **98** (8).
148. Pimenta Martins, L.G., Carvalho, B.R., Occhialini, C.A., Neme, N.P., Park, J.H., Song, Q., Venezuela, P., Mazzoni, M.S.C., Matos, M.J.S., Kong, J., and Comin, R. (2022) Electronic Band Tuning and Multivalley Raman Scattering in Monolayer Transition Metal Dichalcogenides at High Pressures. *ACS Nano*.
149. Freyland, W. (2011) *Spin Physics in Semiconductors*.
150. Paradisanos, I., Wang, G., Alexeev, E.M., Cadore, A.R., Marie, X., Ferrari, A.C., Glazov, M.M., and Urbaszek, B. (2021) Efficient phonon cascades in WSe₂ monolayers. *Nat. Commun.*, **12** (1), 1–7.
151. Shepard, G.D., Ardelean, J. V., Ajayi, O.A., Rhodes, D., Zhu, X., Hone, J.C., and Strauf, S. (2017) Trion-Species-Resolved Quantum Beats in MoSe₂. *ACS Nano*, **11**

- (11), 11550–11558.
152. Hao, K., Xu, L., Wu, F., Nagler, P., Tran, K., Ma, X., Schüller, C., Korn, T., MacDonald, A.H., Moody, G., and Li, X. (2017) Trion valley coherence in monolayer semiconductors. *2D Mater.*, **4** (2).
 153. He, Y.M., Clark, G., Schaibley, J.R., He, Y., Chen, M.C., Wei, Y.J., Ding, X., Zhang, Q., Yao, W., Xu, X., Lu, C.Y., and Pan, J.W. (2015) Single quantum emitters in monolayer semiconductors. *Nat. Nanotechnol.*, **10** (6), 497–502.
 154. Ross, J.S., Klement, P., Jones, A.M., Ghimire, N.J., Yan, J., Mandrus, D.G., Taniguchi, T., Watanabe, K., Kitamura, K., Yao, W., Cobden, D.H., and Xu, X. (2014) Electrically tunable excitonic light-emitting diodes based on monolayer WSe₂ p-n junctions. *Nat. Nanotechnol.*, **9** (4), 268–272.
 155. Devi, A., Kumar, N., Thakur, A., Kumar, A., Singh, A., and Ahluwalia, P.K. (2022) Electronic Band Gap Tuning and Calculations of Mechanical Strength and Deformation Potential by Applying Uniaxial Strain on MX₂(M = Cr, Mo, W and X = S, Se) Monolayers and Nanoribbons. *ACS Omega*, **2**.
 156. Dirnberger, F., Ziegler, J.D., Faria Junior, P.E., Bushati, R., Taniguchi, T., Watanabe, K., Fabian, J., Bougeard, D., Chernikov, A., and Menon, V.M. (2021) Quasi-1D exciton channels in strain-engineered 2D materials. *Sci. Adv.*, **7** (44).
 157. Feng, J., Qian, X., Huang, C.W., and Li, J. (2012) Strain-engineered artificial atom as a broad-spectrum solar energy funnel. *Nat. Photonics*, **6** (12), 866–872.
 158. Glazov, M.M., Ivchenko, E.L., Wang, G., Amand, T., Marie, X., Urbaszek, B., and Liu, B.L. (2015) Spin and valley dynamics of excitons in transition metal dichalcogenide monolayers. *Phys. Status Solidi Basic Res.*, **252** (11), 2349–2362.
 159. Kapuściński, P., Delhomme, A., Vaclavkova, D., Slobodeniuk, A.O., Grzeszczyk, M., Bartos, M., Watanabe, K., Taniguchi, T., Faugeras, C., and Potemski, M. (2021) Rydberg series of dark excitons and the conduction band spin-orbit splitting in monolayer WSe₂. *Commun. Phys.*, **4** (1).
 160. Honold, A., Schultheis, L., Kuhl, J., and Tu, C.W. (1989) Collision broadening of two-dimensional excitons in a GaAs single quantum well. *Phys. Rev. B*, **40** (9), 6442–6445.
 161. Damen, T.C., Shah, J., Oberli, D.Y., Chemla, D.S., Cunningham, J.E., and Kuo, J.M. (1990) Exciton dynamics in GaAs quantum wells. *J. Lumin.*, **45** (1–6), 181–185.
 162. Gruber, A., Dräbenstedt, A., Tietz, C., Fleury, L., Wrachtrup, J., and Von Borczyskowski, C. (1997) Scanning confocal optical microscopy and magnetic resonance on single defect centers. *Science (80-.)*, **276** (5321), 2012–2014.
 163. Acosta, V., and Hemmer, P. (2013) Nitrogen-vacancy centers: Physics and applications. *MRS Bull.*, **38** (2), 127–130.

164. Bradac, C., Gao, W., Forneris, J., Trusheim, M.E., and Aharonovich, I. (2019) Quantum nanophotonics with group IV defects in diamond. *Nat. Commun.*, **10** (1), 1–13.
165. Zhang, J., Huo, Y., Rastelli, A., Zopf, M., Höfer, B., Chen, Y., Ding, F., and Schmidt, O.G. (2015) Single photons on-demand from light-hole excitons in strain-engineered quantum dots. *Nano Lett.*, **15** (1), 422–427.
166. Pooley, M.A., Bennett, A.J., Shields, A.J., Farrer, I., and Ritchie, D.A. (2014) Energy-tunable quantum dot with minimal fine structure created by using simultaneous electric and magnetic fields. *Phys. Rev. Appl.*, **1** (2), 1–5.
167. Stevenson, R.M., Young, R.J., Atkinson, P., Cooper, K., Ritchie, D.A., and Shields, A.J. (2006) A semiconductor source of triggered entangled photon pairs. *Nature*, **439** (7073), 178–182.
168. Ghali, M., Ohtani, K., Ohno, Y., and Ohno, H. (2012) Generation and control of polarization-entangled photons from GaAs island quantum dots by an electric field. *Nat. Commun.*, **3**.
169. Bennett, A.J., Pooley, M.A., Stevenson, R.M., Ward, M.B., Patel, R.B., De La Giroday, A.B., Sköd, N., Farrer, I., Nicoll, C.A., Ritchie, D.A., and Shields, A.J. (2010) Electric-field-induced coherent coupling of the exciton states in a single quantum dot. *Nat. Phys.*, **6** (12), 947–950.
170. Pelucchi, E., Fagas, G., Aharonovich, I., Englund, D., Figueroa, E., Gong, Q., Hannes, H., Liu, J., Lu, C.Y., Matsuda, N., Pan, J.W., Schreck, F., Sciarrino, F., Silberhorn, C., Wang, J., and Jöns, K.D. (2022) The potential and global outlook of integrated photonics for quantum technologies. *Nat. Rev. Phys.*, **4** (3), 194–208.
171. Awschalom, D.D., Hanson, R., Wrachtrup, J., and Zhou, B.B. (2018) Quantum technologies with optically interfaced solid-state spins. *Nat. Photonics*, **12** (9), 516–527.
172. Dousse, A., Suffczyński, J., Beveratos, A., Krebs, O., Lemaître, A., Sagnes, I., Bloch, J., Voisin, P., and Senellart, P. (2010) Ultrabright source of entangled photon pairs. *Nature*, **466** (7303), 217–220.
173. Predojevic, A., Huber, T., Khoshnevar, M., Dalacu, D., Poole, P.J., Majedi, H., and Weihs, G. (2014) Polarization entangled photons from quantum dots embedded in nanowires. *Opt. InfoBase Conf. Pap.*
174. Versteegh, M.A.M., Reimer, M.E., Jöns, K.D., Dalacu, D., Poole, P.J., Gulinatti, A., Giudice, A., and Zwiller, V. (2014) Observation of strongly entangled photon pairs from a nanowire quantum dot. *Nat. Commun.*, **5**.
175. Müller, M., Bounouar, S., Jöns, K.D., Glässl, M., and Michler, P. (2014) On-demand generation of indistinguishable polarization-entangled photon pairs. *Nat. Photonics*,

- 8** (3), 224–228.
176. Stevenson, R.M., Salter, C.L., Nilsson, J., Bennett, A.J., Ward, M.B., Farrer, I., Ritchie, D.A., and Shields, A.J. (2012) Indistinguishable entangled photons generated by a light-emitting diode. *Phys. Rev. Lett.*, **108** (4), 1–5.
 177. Trotta, R., Wildmann, J.S., Zallo, E., Schmidt, O.G., and Rastelli, A. (2014) Highly entangled photons from hybrid piezoelectric-semiconductor quantum dot devices. *Nano Lett.*, **14** (6), 3439–3444.
 178. Kuroda, T., Mano, T., Ha, N., Nakajima, H., Kumano, H., Urbaszek, B., Jo, M., Abbarchi, M., Sakuma, Y., Sakoda, K., Suemune, I., Marie, X., and Amand, T. (2013) Symmetric quantum dots as efficient sources of highly entangled photons: Violation of Bell’s inequality without spectral and temporal filtering. *Phys. Rev. B - Condens. Matter Mater. Phys.*, **88** (4), 3–7.
 179. Zhai, L., Löbl, M.C., Nguyen, G.N., Ritzmann, J., Javadi, A., Spinnler, C., Wieck, A.D., Ludwig, A., and Warburton, R.J. (2020) Low-noise GaAs quantum dots for quantum photonics. *Nat. Commun.*, **11** (1), 1–8.
 180. Sukachev, D.D., Sipahigil, A., Nguyen, C.T., Bhaskar, M.K., Evans, R.E., Jelezko, F., and Lukin, M.D. (2017) Silicon-Vacancy Spin Qubit in Diamond: A Quantum Memory Exceeding 10 ms with Single-Shot State Readout. *Phys. Rev. Lett.*, **119** (22), 1–6.
 181. Sohn, Y.I., Meesala, S., Pingault, B., Atikian, H.A., Holzgrafe, J., Gündoğan, M., Stavrakas, C., Stanley, M.J., Sipahigil, A., Choi, J., Zhang, M., Pacheco, J.L., Abraham, J., Bielejec, E., Lukin, M.D., Atatüre, M., and Lončar, M. (2018) Controlling the coherence of a diamond spin qubit through its strain environment. *Nat. Commun.*, **9** (1), 17–22.
 182. Narvaez, G.A., Bester, G., and Zunger, A. (2005) Pressure effects on neutral and charged excitons in self-assembled (In,Ga)As GaAs quantum dots. *Phys. Rev. B - Condens. Matter Mater. Phys.*, **72** (4), 1–4.
 183. Cao, X., Yang, J., Li, P., Zhang, Y., Rugeramigabo, E.P., Brechtken, B., Haug, R.J., Zopf, M., and Ding, F. (2021) Single photon emission from ODT passivated near-surface GaAs quantum dots. *Appl. Phys. Lett.*, **118** (22).
 184. Fehler, K.G., Ovryan, A.P., Antoniuk, L., Lettner, N., Gruhler, N., Davydov, V.A., Agafonov, V.N., Pernice, W.H.P., and Kubanek, A. (2020) Purcell-enhanced emission from individual SiV-center in nanodiamonds coupled to a Si₃N₄-based, photonic crystal cavity. *Nanophotonics*, **9** (11), 3655–3662.
 185. Plumhof, J.D., Trotta, R., Křápek, V., Zallo, E., Atkinson, P., Kumar, S., Rastelli, A., and Schmidt, O.G. (2013) Tuning of the valence band mixing of excitons confined in GaAs/AlGaAs quantum dots via piezoelectric-induced anisotropic strain. *Phys. Rev. B - Condens. Matter Mater. Phys.*, **87** (7), 33–35.

186. Singh, R., and Bester, G. (2009) Nanowire quantum dots as an ideal source of entangled photon pairs. *Phys. Rev. Lett.*, **103** (6), 1–4.
187. Bracker, A.S., Stinaff, E.A., Gammon, D., Ware, M.E., Tischler, J.G., Shabaev, A., Efros, A.L., Park, D., Gershoni, D., Korenev, V.L., and Merkulov, I.A. (2005) Optical Pumping of the Electronic and Nuclear Spin of Single Charge-Tunable Quantum Dots. *Phys. Rev. Lett.*, **94** (4), 47402.
188. Bracker, A.S., Stinaff, E.A., Gammon, D., Ware, M.E., Tischler, J.G., Park, D., Gershoni, D., Filinov, A. V, Bonitz, M., Peeters, F., and Riva, C. (2005) Binding energies of positive and negative trions: From quantum wells to quantum dots. *Phys. Rev. B*, **72** (3), 35332.
189. Huber, D., Lehner, B.U., Csontosová, D., Reindl, M., Schuler, S., Covre Da Silva, S.F., Klenovský, P., and Rastelli, A. (2019) Single-particle-picture breakdown in laterally weakly confining GaAs quantum dots. *Phys. Rev. B*, **100** (23), 1–9.
190. Benjeddou, A. (2018) Field-dependent nonlinear piezoelectricity: a focused review. *Int. J. Smart Nano Mater.*, **9** (1), 98–114.
191. Ding, F., Singh, R., Plumhof, J.D., Zander, T., Křápek, V., Chen, Y.H., Benyoucef, M., Zwiller, V., Dörr, K., Bester, G., Rastelli, A., and Schmidt, O.G. (2010) Tuning the exciton binding energies in single self-assembled InGaAs/GaAs quantum dots by piezoelectric-induced biaxial stress. *Phys. Rev. Lett.*, **104** (6), 2–5.
192. Wilson, N.P., Yao, W., Shan, J., and Xu, X. (2021) Excitons and emergent quantum phenomena in stacked 2D semiconductors. *Nature*, **599** (7885), 383–392.
193. Cenker, J., Sivakumar, S., Xie, K., Miller, A., Thijssen, P., Liu, Z., Dismukes, A., Fonseca, J., Anderson, E., Zhu, X., Roy, X., Xiao, D., Chu, J.H., Cao, T., and Xu, X. (2022) Reversible strain-induced magnetic phase transition in a van der Waals magnet. *Nat. Nanotechnol.*, **17** (3), 256–261.
194. Singh, A., Tran, K., Kolarczik, M., Seifert, J., Wang, Y., Hao, K., Pleskot, D., Gabor, N.M., Helmrich, S., Owschimikow, N., Woggon, U., and Li, X. (2016) Long-Lived Valley Polarization of Intravalley Trions in Monolayer WSe₂. *Phys. Rev. Lett.*, **117** (25), 1–6.
195. Blaha, P., Schwarz, K., Tran, F., Laskowski, R., Madsen, G.K.H., and Marks, L.D. (2020) WIEN2k: An APW+lo program for calculating the properties of solids. *J. Chem. Phys.*, **152** (7).
196. Bahn, S.R., and Jacobsen, K.W. (2002) L Anguages. *Comput. Sci. Eng.*, **4** (3), 56–66.
197. Perdew, J.P., Ruzsinszky, A., Csonka, G.I., Vydrov, O.A., Scuseria, G.E., Constantin, L.A., Zhou, X., and Burke, K. (2008) Restoring the density-gradient expansion for exchange in solids and surfaces. *Phys. Rev. Lett.*, **100** (13), 1–4.

198. Berkelbach, T.C., Hybertsen, M.S., and Reichman, D.R. (2013) Theory of neutral and charged excitons in monolayer transition metal dichalcogenides. *Phys. Rev. B*, **88** (4), 45318.
199. Glazov, M.M., Amand, T., Marie, X., Lagarde, D., Bouet, L., and Urbaszek, B. (2014) Exciton fine structure and spin decoherence in monolayers of transition metal dichalcogenides. *Phys. Rev. B*, **89** (20), 201302.
200. Berkelbach, T.C., Hybertsen, M.S., and Reichman, D.R. (2013) Theory of neutral and charged excitons in monolayer transition metal dichalcogenides. *Phys. Rev. B - Condens. Matter Mater. Phys.*, **88** (4), 1–6.

Acknowledgements

I still remember it was on October, 10th 2018 when I came to Hannover. Time flies before I know it. I step into the final stage of the Ph.D.

Initially, there is not much stuff in our lab, and our group is not well-organized. I still remember the spin coater in LNQE is broken. For a long time, it was not repaired. The optical lab is empty, but 'clean'. Time witnesses the efforts of our group members. Now, we establish well-built fabrication and measurement apparatuses, which act as the most important support for scientific research.

First, I need to express my gratitude to Prof. Dr. Fei Ding, who is such a kind supervisor. When I was frustrated, he will be the one who raises me up. His overview and guidance is the lamp tower in my long-term Ph.D. He is very powerful when I need help. Another important aspect, the mini-jobs, and extension of the contract save me from bankruptcy.

I would like to say thanks to Prof. Dr. Jonathan J. Finley and Dr. Andreas V. Stier from technical university Munich. Thanks for the synergy in our mutual project SPP 2244. As a green hand of 2D TMDs, I did not know how to analyze the data and how to tell the story. They steer the wheel of our project, a very critical role. Also thanks to them for the nice reception on my trip to Munich.

I would like to thank Prof. Dr. Rolf Haug, who is a very kind and nice researcher. I got multiple permissions from him for wire bonding, gold deposition, and AFM measurement. In the experimental design of electric tuning 2D materials, he gave me significant suggestions.

I need to say a big thanks to Prof. Dr. Mikhail M. Glazov from Ioffe Physical-Technical Institute, Russian Academy of Sciences, who is a very efficient researcher. He owns a shining record in the theoretical works of strain-tuning 2D materials. He gave me the critical guidance in the anisotropic strain tuning WSe₂.

I would like to give my hot thanks to Prof. Dr. Alexey Chernikov from technical university Dresden, who is so experienced in the research of 2D materials and is able to judge the experiments from the tiny aspect.

A special thanks to Prof. Dr. Kaiqiang Lin from the University of Regensburg, now in University of Xiamen. He did a nice job and achieved shining publications. He is a nice expert in the high-lying exciton in TMDs and got a nice overview of the TMDs research. He

helps me with the SHG and Raman setup. The collaborations with him in the electric-tuning of 2D materials, and uniaxial strain-tuning monolayer is very meaningful to me.

An indispensable thanks to Dr. Michael Zopf, who joined all the discussions of the experimental outputs and offers me helpful suggestions to optimize them. His help in data organization and coding impressed me. His involvement in the book chapter is fundamentally important. His innovation in data fitting inspires me a lot.

Another thanks belong to Dr. Eddy P. Rugeramigabo. For me, it's true that whenever I have trouble, go to Eddy. Eddy knows how to find the proper devices, where to deposit metal/dielectric materials, how to do the instrument maintenance, how to do the electric connection, where to cut wafers, and how to buy stuff from overseas. Eddy always provides the most straightforward help to take me out of the dilemma. Thanks to Eddy for the 2 leg manuscript revision.

I need to say thanks to my most intimate partner Dr. Pedro Soubelet and Dr. Alex Delhomme from technical university Munich. Pedro supports me with a lot of nice ML and heterobilayer TMDs samples on piezoelectric actuators. What impresses me most is his ability in data analysis and modeling. His involvement is definitely a must for the job in ML and heterobilayer work. Together with Pedro and Alex, we did a nice measurement in the heterobilayer sample.

A big thank goes to Jonas M. Bauer. His sample fabrication is quite nice, which is the foundation of the uniaxial strain tuning and electric tuning of WSe₂.

A big thank goes to Dr. Jingzhong Yang, who is the main builder of the optical setups. His understanding of the science and operation of the device is always inspiring. The discussions with him on optical stuff are reliable. Jingzhong transferred the operation technique associated with the GaAs membrane and revised the 2-leg manuscript.

Also, I need to thank Dr. Xin Cao, my nice friend, who takes me biking and playing badminton and uno. In the experiments, Xin leads me through the initial phase of optical measurement, and he always gives me some useful help. Xin revised the 2-leg manuscript.

I thank Dr. Paulo E. Faria Junior, Dr. Yaroslav Zhumagulov, and Prof. Dr. Jaroslav Fabian from the University of Regensburg, for the help in theoretical help in ML WSe₂.

I thank our collaborators from laser center Hannover, Maik Steinbach, Jürgen Koch, and Peter Jäschke, who help us to cut the MEMS structure of bulk and film piezoelectric strain-tuning platforms.

Thank you to all my colleagues in Hannover, Pengji Li (always inspiring ideas in research and the help in everyday life), Chenxi Ma (the patient instruction in the EBL-RIE operation), Yiteng Zhang (the bonding by Indium particles, AFM measurement of hBN thickness), Frederik Benthin (coding, the data splitting, LCVR controlling, and Teqo Configurations), Dr. Christian Laurio, Taoran Li, Zhihua Lin, Constantin Schmidt, Tom Fandrich, Zenghui Jiang, Frederik Bettle, Yinan Wang, Xian Zheng, Ruolin Guan, Muti Liu, Tingting Liang for the help.

Thank Dr. Lina Bockhorn, Mr. Ronny Huether, Dr. Benedikt Brechtken, and Bei Zheng from Prof. Dr. Haug's group for the help in deposition, wire bonding, step-profile measurement, instruction of EBL technique and scientific & technological discussions.

I thank Ms. Heike Kars, for her patience and instruction in the numerous form filling and reimbursement.

Many thanks belong to the working staff in LNQE, Dr. Fritz Schulze Wischeler, Oliver Kerker, Raymond Zieseniß, Andrea Lissel, working staff in the mechanical workshop, Jens Wegmann, and Matthias Rabe.

I thank all my friends in Germany. It's nice to meet you.

Thanks to my main sponsor China scholarship committee for the scholarship from Oct. 2018 to Oct. 2022.

Last but not least, I have to thank my family for the support of the Ph.D., my dear mum, dear dad, dear sister, nephew, and niece. I love you more than I can say.

Publications and Presentations

Publications and manuscripts:

Zhao An, Michael Zopf, and Fei Ding. (2022) Strain-Tuning of 2D Transition Metal Dichalcogenides, in *Nanomembranes*, John Wiley & Sons, Ltd, pp. 413–448. Chapter 1.

Strain control of exciton and trion valley depolarization in monolayer transition metal dichalcogenides, Zhao An, Pedro Soubelet (co-first), Yaroslav Zhumagulov, Michael Zopf, Alex Delhomme, Chenjiang Qian, Paulo E. Faria Junior, Jaroslav Fabian, Fredrik Benthin, Xin Cao, Andreas V. Stier, Fei Ding, and Jonathan J. Finley. Chapter 3.

Manipulation of WSe₂ exciton fine structure by anisotropic strain. Zhao An, Jonas Bauer, Mikhail Glazov, Alexey Chernikov, Pengji Li, Jingzhong Yang, Eddy P. Rugeramigabo, Michael Zopf, Kaiqiang Lin, and Fei Ding. Chapter 4.

Strain-induced modulation of quantum dot emissions at Si-Vacancy transitions. Zhao An, Xin Cao, Jingzhong Yang, Maik Steinbach, Jürgen Koch, Peter Jäschke, Eddy P. Rugeramigabo, Fredrik Benthin, Rolf Haug, Michael Zopf, and Fei Ding. Chapter 5.

Scientific Talks and Posters

Talk: Winter School of the institute for Solid State Physics. ‘Strain tuning low-dimensional materials’. Springer, Germany. November 26th, 2021.

Talk: DPG Conference: ‘Control of valley polarization in WSe₂ by strain’. University Regensburg, Germany, September 5th, 2022.

Poster: Nano day: ‘Piezo-based MEMS for tuning the properties of low-dimensional materials’. LU Hannover, Germany. October 10th, 2019.

Poster: Summer day: ‘Strain tuning of 2D semiconductors’. LU Hannover July 21st, 2022.

Selbständigkeitserklärung

Hiermit erkläre ich an Eides statt, dass ich die am heutigen Tag eingereichte Dissertation zum Thema “ Investigations of low-dimensional emitter system by dynamic strain platform” unter der Betreuung von Herrn Prof. Dr. Fei Ding selbständig erarbeitet, verfasst und Zitate kenntlich gemacht habe. Andere als die angegebenen Hilfsmittel wurden von mir nicht benutzt.

Die Dissertation wurde in dieser oder ähnlicher Form an keiner anderen Stelle zum Zwecke eines Promotionsverfahrens eingereicht. Es wurde von mir bisher kein Promotionsverfahren an anderer Stelle beantragt.

Curriculum Vitae

Personal information:

Name: Zhao An (安钊)

Date of birth: 06.11.1989

Place of birth: Shijiazhuang, China

Nationality: Chinese

Education and working experience:

Sept.2009 – July 2013: Northern University, China

Bachelor of Materials Science and Engineering

Sept.2013 – July 2016: Institute of Acoustics, Chinese Academy of Sciences, China

Master of Acoustics, specializing in piezoelectric materials

July 2016 – July 2018: Key lab, 13th institute, China Electronic Technology Group Corporation (CETC-13), China

MBE engineer, specializing in MBE epitaxy of structure

Oct. 2018 – present: Leibniz University Hannover, Germany

Ph.D. Candidate

Previous Publications:

Liao, Q., Zheng, L., **An, Z.**, Huang, H., Yan, C., Qin, L., Wang, L., and Peng, S. (2017) Crystal structure and thermal characteristics of Mn modified ultra-high curie temperature (>800 °C) Bi₂WO₆ piezoelectric ceramics. *J. Alloys Compd.*, **692** (C), 454–459.

Huang, H., **An, Z.**, Huang, P., Li, D., and Liao, Q. (2016) Phase transition and thermal depolarization of double perovskite modified low sintering temperature PbTiO₃ piezoelectric ceramics. *J. Eur. Ceram. Soc.*, **36** (3), 925–929.

Liao, Q., Huang, P., **An, Z.**, Li, D., Huang, H., and Zhang, C. (2016) Origin of thermal depolarization in piezoelectric ceramics. *Scr. Mater.*, **115**, 14–18.

Liao, Q. and Huang, H. were my mentor and supervisor, respectively.